University of Alberta

Dose Verification in Image Guided Adaptive Radiotherapy

By

Steven David Thomas 

A thesis submitted to the faculty of Graduate Studies and Research in partial fulfillment of the requirements for the degree of Doctor of Philosophy

in

Medical Physics

Department of Physics

Edmonton, Alberta
Fall 2007

Your file Votre référence
ISBN: 978-0-494-33078-4
Our file Notre référence
ISBN: 978-0-494-33078-4

I felt a clearing in my mind
As if my brain had split;
I tried to match it, seam by seam,
But could not make them fit.

The thought behind I strove to join
Unto the thought before,
But sequence raveled out of reach
Like balls upon the floor.

Emily Dickinson

I like it.
I don't know what it all means,
but it makes me crazy.

Doug Sandilands

To my family and friends
for making it worth it.

Abstract

Image guided radiation therapy (IGRT) has evolved naturally from the increased use of imaging modalities in radiation therapy. Along with IGRT has come an increase in the ability to geometrically conform dose distributions to pathology. This conformity comes at the cost of greater complexity for both the radiation therapy planning and delivery modalities. Increased complexity in turn requires heightened vigilance to ensure that radiation delivery is planned and executed in an accurate manner. This thesis involves aspects of dose verification for two current IGRT delivery techniques. In part 1 of this thesis, dose verification for the Helical TomoTherapy^{TM} (HT) treatment modality is investigated and benchmarked. First, a Monte Carlo determined AAPM TG-51 calibration for HT is created. This allows for accurate dose determination of the HT treatment modality. Using this increase in measured dose accuracy two dimensional treatment verifications for 10 patients planned and treated with HT are determined and tabulated. From the tabulated data three criteria for satisfactory treatment verifications of a plan are established. In part 2 of this thesis the use of magnetic resonance imaging (MRI) for post implant seed identification (an important part of dose verification) of prostate brachytherapy treatments is investigated. Magnetic distortions surrounding a typical brachytherapy seed within a clinical MRI are modeled for 3 different seed orientations with respect to the main magnetic field. From the distortion maps, simulated images are produced. These simulated images are then compared to images of brachytherapy seeds suspended in a porcine gel acquired on a Philips 1.5T MRI scanner using the same parameters used to simulate the images. A normalized cross correlation between the

simulated and experimentally acquired images is used to demonstrate the possible feasibility of such a simulation being used to determine seed positions in-vivo. Finally, the potential advantages of using a high field 3.0T MRI system for post implant seed dosimetry are investigated. This is done by acquiring and comparing images of a typical brachytherapy seed suspended in a porcine gel phantom acquired using clinical MR imagers at both 1.5T and 3.0T field strengths.

Acknowledgements

I would like to thank a great number of people. These people have kept me going in one way or another for what now seems along time. To give them full credit would require such pages as to dwarf the academic text of the thesis. Instead I shall just list them and a little about them and hope they understand my paper constraints.
Thank you:
Gino Fallone who knows how to make big ideas into realities. **Marc MacKenzie** who is the modern Renaissance man and thus great at dinner parties. **Tara Bug** who says the most wonderful things, grew with me and beat me to the end. **Keith W** who is great at Matlab and humors me in my choice of bad movies. **Hammer** who knows how to laugh, make me laugh and expanded my view of the world. **LBJ** my dinner partner who likes poetry and paintings, and who says yes to adventure. **Erin** who is much smarter than I, is down to earth and makes any place she is at better. **Big Al** who is the most fun to get in trouble with and who throws fun parties. **Alana H** who is not scared of distance. **Anna** who makes a party a party. **Keith N** who is a bona fide rock star, likes a good joke and night skies. **Atiyah** who often knows what is important. **The Brad** who is really just the nicest guy you could ever meet and a composer of songs to dogs. **Heather** who knows (to the nearest integer) the number of weeks in a year. **Dug** who is broke but enlightened (I'm not sure if that is the cost of enlightenment). **Merc** who is into epic adventure and sometimes brings me along. **Orr** who is not afraid to go past my comfort level. **Denny** who shows you he loves you by being difficult. **Mark** who can get into something like you've never seen before. **Stacie** who likes canoes more than rings which says a lot. **Meg** who knows most of the things that make cities great. **Shane** who just knows a lot of stuff. **Gom** who can do everything. **Afra** who likes to watch the way people move. **Hyo** who never liked Taco Bell. **Sandra** who loves to laugh and dance. **Dave** who can get up to speed very quickly. **Matt** who is not intimidated by size (though maybe he should be). **Rivest** who really likes to give'r. **Len** who can fix anything. **Amy** who is Amy. **Beau, Trav (el presidente), Suz, Chris, Ryan and Alan** who are the best ever (now clapping). **Colin** who knows what we should be doing. **Satyapal** who believes in putting ones very best foot forward. **Dave Rogers** who knows a lot about what those photons and electrons are actually doing. **Alan Wilman** who will tell you, when it's just up to you to make it work. **Teo** who knows the value of courses and climbs. **Isabelle** who has been in it with me for the long haul. **Sarah** who taught me the benefits of having a great sibling and who is like me (crazy). **Dad** who taught me to think for myself. **Mom** who taught me to worry about the people I love and who makes Lethbridge home.

I would also like to thank the following people for their guidance and help at various points along the way.
Don, Rick, Ron, Yusuf, Maureen, Debbi, Jocelyn, Ken, Gary, Brad M., Christian, Dan, Brad, Karl, Charlie, Geetha, Emily, KJ, Moira (BFF), Conrad, Suzie, Stephen, Sherri, Terry, Brent, , Alana, Marco, Hans, Ernie, Ying Li, Nora and Paul, Dalia and Mary,.

I know I have inevitably forgotten important people but you know who you are and I hope you know how important you are to me. Thanks again everybody.

Table of Contents

Chapter 4: Patient specific delivery verification for 10 HT Treatment Plans

Part 2: Seed Identifcation Required for Delivery Varification in Brachytherapy

Chapters 5 -6

Chapter 5: Characterization of the susceptibility artifact around a prostate brachytherapy seed in MRI

Chapter 6: Imaging a Prostate Brachytherapy Seed at 1.5 and 3.0 Tesla: an In Vitro Study

Chapter 7: Conclusions

Appendix A: AAPM Task-Group - 51 (TG-51)

Appendix B Monte Carlo and the EGSnrc user code

Appendix C: Introduction to MRI

List of Tables

List of Figures

List of Symbols

B	Magnetic Field
B_O	Main Magnetic Field
B_{eff}	Effective Magnetic Field
BW_{rf}	Band Width of the RF pulse
BW_{read}	Band Width of the Read Gradient
B_1	Circularly Polarized Magnetic Field
d	Displacement in the Direction of the Gradient
D_w^Q	Dose to Water from a Beam of Quality Q
D_m	Measured point dose
D_c	Calculated point dose
$D(r_c)$	Calculated Dose at Position r_c
$D(r_m)$	Measured Dose at Position r_m
DS#1	Data Set Number 1
DS#2	Data Set Number 2
E	Interaction Energy
F_Z	Magnetic Distortion Map
FOV_{phase}	Field of View in the Phase Direction
FOV_{read}	Field of View in the Read Direction
G_{read}	Read Gradient
G_{phase}	Phase Gradient
G_{SS}	Slice Select Gradient
g_{SS}	Nominal Slice-Selective Gradient Strength

g_{xR}	Nominal Read Gradient Strength in the X direction
g_{yR}	Nominal Read Gradient Strength in the Y direction
g_{xR}	Nominal Read Gradient Strength in the Z direction
H	H field
I	Spin angular momentum operator
I_0	Light Traveling into Material
I_t	Light Transmitted through Material
K	Boltzman's constant
K_h	Humidity Correction Factor
k_Q	Photon Beam Quality Conversion Factor
k_{phase}	Position in K-Space Phase Direction
k_{read}	Position in K-Space Phase Direction
$\left(\bar{L}/\rho\right)_{air}^{water}$	Water-to-Air Mean Restricted Mass Collision Stopping Power Ratio
M	Fully Corrected Electrometer Reading
m_{air}	Mass of Air in the Ion Chamber
M_{raw}	Raw Electrometer Reading
M_{raw}^{H}	Electrometer Reading taken at High Voltage Setting
M_{raw}^{L}	Electrometer Reading taken at Low Voltage Setting
M_{raw}^{+}	Positive Voltage Electrometer Reading
M_{raw}^{-}	Negative Voltage Electrometer Reading
M_{SIG}	Binary Signal Mask
M_{SS}	Binary Slice Selective Mask

M_{xy}	Transverse Magnetization
M_x	Magnetization in the X direction
M_y	Magnetization in the Y direction
M_z	Longitudinal Magnetization
M_O	Total Magnetization
N_{pe}	Number of Phase Encodes
$N_{\|\alpha\rangle}$	Number of Spins in the $\|\alpha\rangle$ Eigenstate
$N_{\|\beta\rangle}$	Number of Spins in the $\|\beta\rangle$ Eigenstate
$N_{D,w}^{^{60}Co}$	Absorbed Dose to Water Calibration Coefficient for a ^{60}Co Beam
NSA	Number of Signal Averages
OD	Optical Density
P	Pressure
P_{cel}	Central Electrode Correction Factor
P_{elec}	Electrometer Correction Factor
P_{fl}	Fluence Correction Factor
P^{gr}	Gradient Correction Factor
P_{ion}	Ionization Correction
P_{pol}	Polarity Correction Factor
P_{repl}	Cavity Replacement Correction Factor
$P_{T,P}$	Temperature and Pressure Correction Factor
P_{wall}	Cavity Wall Correction Factor
r	Random Number

r_c	Position of the Calculated Dose Pixel
r_m	Position of the Measured Dose Pixel
sl	Slice Thickness
T	Temperature
t_{phase}	Phase Encode Time
T_{trans}	Transmittance
TE	Echo Time
TR	Repetition Time
T1	Longitudinal Relaxation Time
T2*	Tranverse Relaxation Time (reversible and non reversible)
T2'	Tranverse Relaxation Time (reversible)
T2	Tranverse Relaxation Time (non reversible)
V_H	Electrometer Voltage for M_{raw}^H Reading
V_L	Electrometer Voltage for M_{raw}^L Reading
x_{SIG}	Correct M_{xy} Magnetization X Location
x_{SIG}^*	Apparent X Position of the M_{xy} Magnetization
y_{SIG}	Correct M_{xy} Magnetization Y Location
y_{SIG}^*	Apparent Y Position of the M_{xy} Magnetization
z_{SIG}	Correct M_{xy} Magnetization Z Location
z_{SIG}^*	Apparent Z Position of the M_{xy} Magnetization
$\left(\overline{W}/e\right)$	Mean Excitation Energy per Ion Pair Formed
α_{TIP}	Tip Angle

α	Contribution of Dose from the Medium Electrons
β	Contribution of Dose from the Wall Electrons
Δd_M	Distance to Agreement Criteria
ΔD_M	Dose Difference Criteria
$\gamma(r_c)$	DQA Gamma Value at Position r_c
γ	Proton Gyromagnetic Ratio
$\hbar$	Planks Constant divided by 2π
τ	Iteration Parameter
μ_p	Photon Interaction Coefficient
$\boldsymbol{\mu}$	Magnetic Dipole Moment
μ_M	Magnetic Permeability
μ_0	Permeability of Free Space
μ_x	Magnetic Moment X Component
$\mu_{x\rho}$	Magnetic Moment X Component in the Rotating Reference Frame
μ_y	Magnetic Moment Y Component
$\mu_{y\rho}$	Magnetic Moment Y Component in the Rotating Reference Frame
$\mu_{z\rho}$	Magnetic Moment Z Component
$\mu_{z\rho}$	Magnetic Moment Z Component in the Rotating Reference Frame
$\left(\overline{\mu_{en}/\rho}\right)_{water}^{wall}$	Wall-to-Water Ratio of Mean Mass Energy Absorption Coefficients
$\left(\overline{\mu_{en}/\rho}\right)_{water}^{C552}$	C552-to-Water Ratio of Mean Mass Energy Absorption Coefficients
$\varphi(E)$	Energy Fluence Spectrum

Φ_M	Magnetic Scalar Potential
ω_ρ	Rotation Frequency in the Rotating Reference Frame
ω_O	Larmor Frequency
χ_M	Magnetic Susceptibility Constant
$\|\alpha\rangle$	Spins Parallel to B_O
$\|\beta\rangle$	Spins Anti Parallel to B_O

List of Abbreviations

A1SL	Exradin A1SL ion Chamber
BFFE	Balanced Fast Field Echo
BTV	Biological Target Volume
CT	Computed Tomography
CTV	Clinical Target Volume
d_{max}	Depth of Maximum Dose
DTA	Distance to Agreement
DQA	Delivery Quality Assurance
EBRT	External Beam Radiation Therapy
FOV	Field Of View
FS	Field Size
FSE	Fast Spin Echo
FWHM	Full Width at Half the Maximum amplitude
GBM	Glioblastoma Multiforme
GE	Gradient Echo
GTV	Gross Tumor Volume
H&D	Hurter and Driffield
H&N	Head and Neck
HDR	High Dose Rate
HT	Helical TomoTherapy
ICRU	International Commission on Radiation Units and Measurement
IGRT	Image Guided Radiation Therapy

IMRT	Intensity Modulated Radiation Therapy
LDR	Low Dose Rate
MDR	Medium Dose Rate
MGR	Merry Go Round reference frame
MLC	Multi Leaf Collimator
MPR	Multi Planar Reconstruction
MRI	Magnetic Resonance Imaging
MRSI	Magnetic Resonance Spectroscopic Imaging
MVCT	Mega Voltage Computed Tomography
NMR	Nuclear Magnetic Resonance
NSA	Number of Signal Averages
OD	Optical Density
P	Prostate
PBM	Palliative Bone Metastasis
PDR	Pulsed Dose Rate
PET	Positron Emission Tomography
PTV	Planning Target Volume
RF	Radio Frequency
SAR	Specific Absorption Rate
SIB	Simultaneous Integrated Boost
SNR	Signal to Noise Ratio
spr	Ratio of mean restricted mass collision Stopping Power
SSD	Source Surface Distance

TE	Echo Time
TR	Repetition Time
%dd	Percent Depth Dose
$\%dd(10)_x$	Percent Depth Dose at 10 cm depth
2D	Two Dimensional
3D	Three Dimensional

Chapter 1 Introduction to the Thesis

The sub-field of image guided radiation therapy (IGRT) has evolved naturally from the increased use of imaging modalities in radiation therapy. Along with IGRT has come an increase in the ability to geometrically conform dose distributions to pathology. This conformity comes at the cost of complexity for both the planning and delivery modalities used in modern radiation therapy. Increased complexity in turn requires heightened vigilance to ensure that radiation delivery is planned and executed in an accurate manner. This thesis involves aspects of dose verification for two current IGRT radiation delivery techniques. In part 1 of this thesis, dose verification for the Helical TomoTherapy™ (HT) treatment modality is investigated and benchmarked. In part 2 of this thesis the use of magnetic resonance imaging (MRI) for post implant dose verification and evaluation of prostate brachytherapy treatments is investigated. Chapter 1 of this thesis provides an overview of the topics discussed in each of the following chapters.

Chapter 1: Introduction to the Thesis

Chapter 1 introduces the topics discussed in the rest of the thesis.

Chapter 2: Cancer and Radiation Therapy

Chapter 2 introduces the reader to common concepts associated with cancer and radiation therapy. The reader is first introduced to the pathology of cancer and its resultant impact on public health. Common cancer treatments such as surgery,

chemotherapy and radiation therapy are discussed. Next, the clinically important tumor definitions of gross tumor volume, clinical tumor volume and planning target volume are given, and the concept of the biological tumor volume is introduced.

The next section of chapter 2 gives an overview to some common imaging and delivery modalities currently used in radiation therapy. Thus the imaging modalities of computed tomography and magnetic resonance imaging are briefly discussed and the radiation delivery modalities of teletherapy and brachytherapy are introduced. Because of its importance to the first half of the thesis, the history of the development of teletherapy including more recent advances of intensity modulation radiation therapy and Helical HT are described. The method of HT radiation delivery is described as well as the mechanical set up of the Hi-Art 2 HT system.

In the final section, various types of brachytherapy are discussed and further classifications of low dose rate, medium dose rate, high dose rate, permanent implant and temporary implant are also defined.

Chapter 3: A TG-51 Calibration for Helical TomoTherapy ™

Helical TomoTherapy™ is a recent modality for delivering IMRT. As such HT requires a method of accurately determining the absorbed dose under reference conditions. In the American Association of Physicists in Medicine (AAPM) TG-51 external beam dosimetry protocol, k_Q, is presented as a function of the photon component of the percentage depth-dose at 10 cm depth, $\%dd(10)_x$, measured under

the reference conditions of a 10x10 cm^2 field size and a source-to-surface distance (SSD) of 100 cm. The value of $\%dd(10)_x$ from HT cannot be used for the determination of k_Q because the design of the HT does not meet the following TG-51 reference conditions:

i) the field size and the practical SSD required by TG-51 are not obtainable

ii) the absence of the flattening filter changes the beam quality thus affecting some components of k_Q. The stopping power ratio is not affected because of its direct relationship to $\%dd(10)_x$.

In chapter 3, we derive a relationship for the Exradin A1SL ion chamber converting the $\%dd(10)_x$ measured under HT "reference conditions" of SSD=85 cm and a 5x10 cm^2 field-size ($\%dd(10)_{x\,[HT\ Ref]}$), to the dosimetric equivalent value under for TG-51 reference conditions ($\%dd(10)_{x\,[HT\ TG\text{-}51]}$) for HT. This allows the determination of k_Q under the HT reference conditions. This conversion relationship should also apply to other ion chambers with possible errors on the order of 0.1%.

Chapter 4: Patient Specific Delivery Verification for 10 HT Treatment Plans

In chapter 4, two dimensional treatment verifications for 10 patients planned and treated with HT are determined and tabulated. The treatment verification consists of a film measurement as well as point dose measurements made with an ion chamber.

Possible dosimetric errors which may occur from using film are discussed. The agreement between the calculated and the measured film dose distributions are evaluated with the gamma index calculated for 3 sets of criteria (2 mm & 2%, 4 mm & 3% and 3mm & 5%) as recommended in the literature. Agreements are determined for both un-normalized dose data and dose map registration using reference marks as well as dose data in which normalization and manual registration of the dose maps are employed. Three criteria for satisfactory treatment verifications in the high dose regions of a plan are established.

Chapter 5: Characterization of the Susceptibility Artifact Around a Prostate Brachytherapy Seed in MRI

In chapter 5, magnetic distortions surrounding a typical brachytherapy seed (IMC6711, OncoSeed^{TM}) within a clinical magnetic resonance (MR) imager are modeled for 3 different seed orientations with respect to the main magnetic field. From the distortion maps, simulated images are produced. Magnetic resonance images of the brachytherapy seed suspended in a 3% by weight porcine gel using a fast spin echo technique were acquired on a Philips 1.5 T MRI scanner using the same parameters as are used to simulate the images. The image artifacts are shown to be dependent on both the orientation of the seed with the main magnetic field, and the direction of read encode gradient. The simulated images allow for determination of seed position with respect to the complex image distortion patterns. Discrepancies between the center of mass from the seed and the center of mass of the image are determined and compared to the literature. Finally a normalized cross correlation

between the simulated images and experimentally acquired images are used to demonstrate the possible feasibility of such a simulation being used to determine seed positions in-vivo.

Chapter 6: Imaging a Prostate Brachytherapy Seed at 1.5 and 3.0 Tesla: an In Vitro Study.

In chapter 6, a typical brachytherapy seed (IMC6711, OncoSeed^{TM}) suspended in a 3% by weight porcine gel phantom is imaged using clinical MR imagers at both 1.5 T and 3.0 T field strengths. Transverse images are acquired on Philips 1.5 T and 3.0 T Intera scanners with both spin echo and gradient echo pulse sequence. Images were acquired with the long axis of the seed oriented both parallel to the main magnetic field and at 45° offset to the main magnetic field in the coronal plane. The images were acquired using 1, 3, and 5 mm slice thicknesses. Images were then reconstructed in the coronal plane using multi-planar reconstruction and the volume of the artifact as well as the maximum length and width of the image artifact were determined. In all cases the size of the artifact was found to increase when performed at the 3.0 T field strength. When using the fast spin echo technique to image non-parallel seed orientations, the increased artifact size was found to offset slice averaging problems when the 3 and 5 mm slice thicknesses were used.

Chapter 7: Conclusion

Chapter 7 summarizes the results of our work and provides some areas of future work.

Appendix A: The TG-51 Protocol

Appendix A introduces some of the basic ideas regarding the photon component of the TG-51 protocol for dose calibration. Discussed are some of the improvements made on the more recent TG-51 protocol with respect to the earlier TG-21 protocol. The formalism for the photon component of TG-51 is outlined including the fully corrected electrometer reading, the absorbed dose to water calibration coefficient for a ^{60}Co beam and the beam quality conversion factor (k_Q). The correction factors for polarity, recombination, temperature and pressure required for the fully corrected electrometer reading are defined. Also discussed, are the cavity replacement, central electrode and the ion chamber wall correction factor P_{wall} inherent in k_Q. Derivations are given for both k_Q an P_{wall}.

Appendix B:

Appendix B gives a description of the Monte Carlo method and the EGSnrc user codes used in the thesis. The Monte Carlo method is described using the distance to interaction for a photon in a medium. The uses of random number generators in Monte Carlo calculations as well as desirable qualities of pseudo random number are discussed. A brief history of the EGSnrc user code is given as well as the general method it employs for handling both photon and charged particle transport. Finally descriptions of the BEAMnrc, DOSXYZnrc, SPRRZnrc, FLURZnrc user codes are provided.

Appendix C:

In appendix C, some of the basic fundamentals of magnetic resonance imaging are discussed. Both the quantum mechanical and classical descriptions for a magnetic dipole moment (corresponding to a hydrogen proton) in a static magnetic field are given. The classical description of excitation is also given for a magnetic moment in a static and circularly polarized magnetic field. To make this description more intuitive the reader is introduced to the rotating frame of reference. Longitudinal and transverse relaxation mechanisms which give rise to image contrast are also discussed. The spatial encoding processes of slice selection, phase encoding and frequency encoding are explained. Finally the reader is introduced to the signal equation and k-space. An example of how a magnetic resonance pulse sequence employing unidirectional frequency encoding traverses k-space is also given.

Chapter 2: Cancer and Radiation Therapy

2.1 Cancer

The Canadian Cancer Society has defined cancer as "the uncontrolled, abnormal growth that can invade and destroy healthy tissues."[1] As cancer cells replicate they form a detectable mass which is referred to as a tumor. Tumors may further spread to other areas within the body, which is referred to as a metastasis.[2] The cancer destroys healthy tissue by competition for resources, resulting in undesirable symptoms and may result in death if left untreated. Although a single name, cancer is actually a general term "for more than 200 diseases."[1]

Cancer is responsible for 27.2% of all mortalities within Canada, which is second only to the 34.0 % of deaths attributable to cardiovascular disease.[3] In addition, cancer is the leading cause of person-years of life lost in Canada, where person-years lost is defined as "the sum of the difference between the actual age of death and the expected remaining lifetime for each person who died of cancer."[4] The number of Canadians who are estimated to have developed cancer in 2004 is approximately 145,500 with an estimated 68,300 expected to die in the same year. Based on current incidence rates it is further expected that about 40% of Canadian citizens will develop cancer during the course of their lives.[5]

The most commonly diagnosed cancers in Canada for men and women are prostate and breast cancer, respectively. Although not the most commonly diagnosed, lung cancer is the leading cause of cancer deaths within Canada. In terms of cancer

prevention, the single most important action is to avoid smoking, which is responsible for about a third of the potential years of life lost.[1] Other preventative measures include, healthy living in conjunction with an active lifestyle as well as limiting sun exposure and alcohol consumption.[1]

2.2 Treatments for Cancer

There are three primary treatments for cancer which are often performed in combination in order to obtain the best result. These treatments are surgery, chemotherapy, and radiation therapy. In surgery the tumor mass is physically removed along with a surrounding margin intended to include any microscopic disease. Surgery, like radiation therapy, is primarily used to treat well localized cancers. Chemotherapy involves the use of a cytotoxic drug with the intention of disrupting the cell cycle of the cancer cells. Chemotherapy is the prime modality for non-localized cancers such as leukemia. Chemotherapy is also employed to shrink a tumor prior to surgery, or to kill residual cancer cells. It is employed after or concurrent to surgery or radiation therapy.[6] Radiation therapy involves the use of radiation to kill tumor cells. It is employed in over half of treatments. Due to its relevance to the work done in this thesis it is described in detail in the following section.

2.3 Radiation Therapy

When ionizing radiation is incident upon a material, energy is imparted to that material. This energy is measured in terms of radiation dose, where dose is defined as the energy imparted per unit mass where 1J/kg=1 Gray (Gy). Although the overall

energy imparted is relatively small, it is released over very small volumes making it sufficient to break molecular bonds.

In the case of living cells several outcomes may result from this energy deposition including: cell death, mutation and carcinogenesis.[7,8] These outcomes are possible for both diseased and healthy tissues, which makes radiation a "double-edged sword" in terms of its use as a therapeutic agent. The first therapeutic radiation treatment dates back to 1896 when E.H. Grubbe used an x-ray tube to irradiate diseased breast tissue.[9] Understanding the effect of radiation upon healthy tissue as a result of his prior experience testing x-ray tubes with his hand, E.H Grubbe shielded the healthy tissue surrounding the tumor using lead sheets. This first treatment highlights the goals of radiation therapy, which have been the focus of improvements ever since 1896, and are as follows:

1) To deliver radiation to cancerous tissue in sufficient dose to kill all clonogenic cells within the tumor
2) To deliver as little dose as possible to all healthy tissue to minimize the probability of complications from damage to normal tissues.

In turn, achieving these goals critically requires the following two capabilities: the ability to accurately and precisely determine the location of the diseased cells and differentiate them from healthy cells (i.e. have accurate tumor definition); and the ability to precisely deliver high levels of radiation dose to the diseased cells while minimizing the dose given to any other location within the patient.

Striving to simultaneously fulfill these requirements (precise localization, precise delivery) has made modern radiation therapy a highly integrated discipline consisting of both medical imaging sciences and radiation delivery sciences. In essence, radiation therapy involves the accurate solution to a five dimensional problem. These 5 dimensions include the three Cartesian spatial dimensions (X, Y and Z), time and dose or preferably biological effect. The work in this thesis involves current issues with respect to the accurate measurements of the three spatial dimensions as well as the dose dimension.

2.4 Tumor Definitions for Radiation Therapy

Tumor definition is the process by which the tumor is localized and differentiated from healthy tissue. As the process of tumor definition is limited by our ability to see very small amounts of pathological tissue, several definitions have become important with respect to radiation therapy.[10,11] The gross tumor volume (GTV) is defined as "gross palpable or visible/demonstrable extent and location of malignant growth". (figure. 2-1) The clinical target volume (CTV) is defined as "tissue volume that contains a demonstrable GTV and/or subclinical microscopic malignant disease, which has to be eliminated" (figure. 2-1) The planning target volume is further defined in order "to select appropriate beam sizes and beam arrangements, taking into consideration the net effect of all the possible geometrical variations, in order to ensure that the prescribed dose is actually absorbed in the CTV" (figure. 2-1)

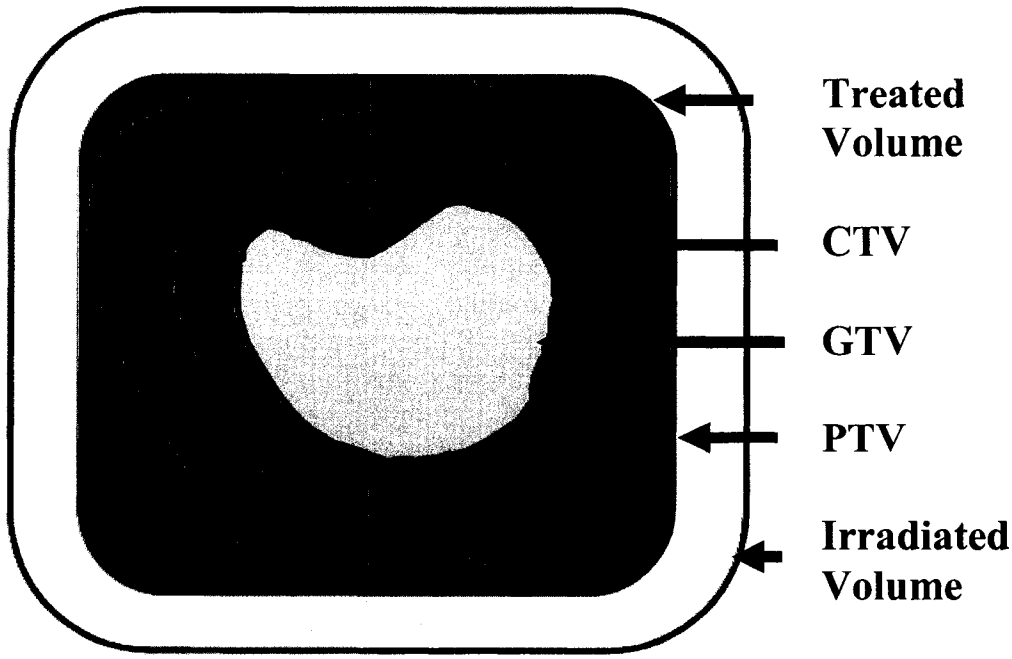

Figure. 2-1 a pictorial representation of GTV, CTV, PTV, treated volume and irradiate volume. The grey area represents the tumor as visible in the image obtained from a particular imaging modality.

Two other volumes of interest are termed the treated volume which is the volume that receives a relatively high dose and the irradiated volume which defines the volume that (in terms of tissue tolerances) receives a significant dose. More recently there has been the addition of the biological tumor volume (BTV) which defines volumes as determined by functional imaging modalities such as positron emission tomography (PET) or magnetic resonance spectroscopic imaging (MRSI).[12,13] The BTV is intended to describe the functional volume of the tumour.

Tumor definition involves two primary imaging modalities computed tomography (CT) and magnetic resonance imaging (MRI). The CT imaging modality primarily uses material density differences as a source of contrast. The primary advantage of CT is its ability to view both bone and lung, which is difficult using MRI. MRI has a number of contrast mechanisms ranging from magnetic properties of tissues to molecular motion. These numerous contrast mechanisms make MRI an extremely useful modality for tumor localization within soft tissue. The MRI imaging modality is discussed in greater detail in appendix C.

2.5 Radiation Delivery Techniques

Radiation delivery consists of two major subcategories, which are teletherapy and brachytherapy ("close therapy").[14]

2.5.1 Teletherapy

Teletherapy or external beam radiation therapy (EBRT) is a primary modality for treating localized cancers. As stated before, EBRT simultaneously delivers radiation to both tumor and healthy surrounding tissues. The delivery of radiation to healthy tissues may lead to treatment side effects. It is these normal tissue complications that generally limit the dose that can be delivered to the tumor, limiting the probability of achieving local tumor control. It is for this reason that a substantial amount of work has been directed at developing techniques to reduce or redistribute healthy tissue dose. The first major advance in EBRT was the use of megavoltage sources. Up to the late 1940s, EBRT treatments involved orthovoltage x-ray sources

with energies in the 200 to 400 kVp range (i.e. filtered x-ray spectra with energies up to a maximum of 200 to 400 keV). Treatments at these energies often resulted in late normal tissue complications primarily occurring in bone.[15] It was at that time hoped that the improved depth dose aspects of megavoltage sources would lead to improved healthy tissue sparing. Two radiation sources which were employed and are still used today are the ^{60}Co source (1.25 MeV), and the linear accelerator with energies of 2 MV and greater. The results showed significant improvements for various cancer sites. All stages of carcinoma of the cervix showed more than a two-fold increase in survival at 14 yrs when treated with MV modalities.[16] The 10 year survival for all stages of Hodgkin's disease increased from 23% to 62% when treated with MV energies, which was attributed to increases in prescribed doses, which were previously limited by skin dose.[17]

More recent advancements in EBRT have been in the stricter conformation and geometric accuracy of the 3D dose distribution to the shape of the tumor.[18] The latest iteration of this advancement is intensity-modulated radiation therapy (IMRT). The term 'intensity' here refers to the relative energy fluence profile across the plane of the radiation beam. For conventional EBRT machines, this relative energy fluence is made roughly uniform by filtering the bremsstrahlung distribution through a high Z conical filter. The HT modality is a sub-category of IMRT.[19-21]

2.5.2 IMRT

In both dose delivery and dose planning, IMRT is conceptually very different from conventional EBRT. In conventional EBRT, the shape and size of the (generally intensity flattened) beam is determined by pairs of opposed collimator jaws. Resultant radiation fields are thus generally shaped to the PTV with nearly uniform intensity across the field. In some cases the uniform intensity distributions are modified by devices such as wedges to improve the dose distribution within the patient. To obtain an optimized dose distribution satisfying the two goals listed in section 2.3, various parameters such as beam number, beam angle, beam size and the relative beam weights are manually iterated towards values that produce an acceptable plan by a treatment planner. This process of manual optimization of beam parameters is known as forward treatment planning.

IMRT, as the name implies, involves beams with non-uniform 2D intensity profiles.[22] Such beams are produced by subdividing each radiation field (usually 7-15 per treatment) into a large number (e.g. 100's or 1000's) of small "beamlets". The weight of each beamlet can be adjusted so as to create intensity modulated fields which, when appropriately combined, allow for highly conformal three dimensional dose distributions. These highly intensity modulated fields are generally realized using a multi leaf collimator (MLC) in which a number of sub-fields are added together (either statically in step and shoot IMRT or dynamically) to create one intensity modulated field.[20] (See figure. 2-2) An MLC consists of an array of narrow collimating leaves which move across the radiation field. The geometric resolution of

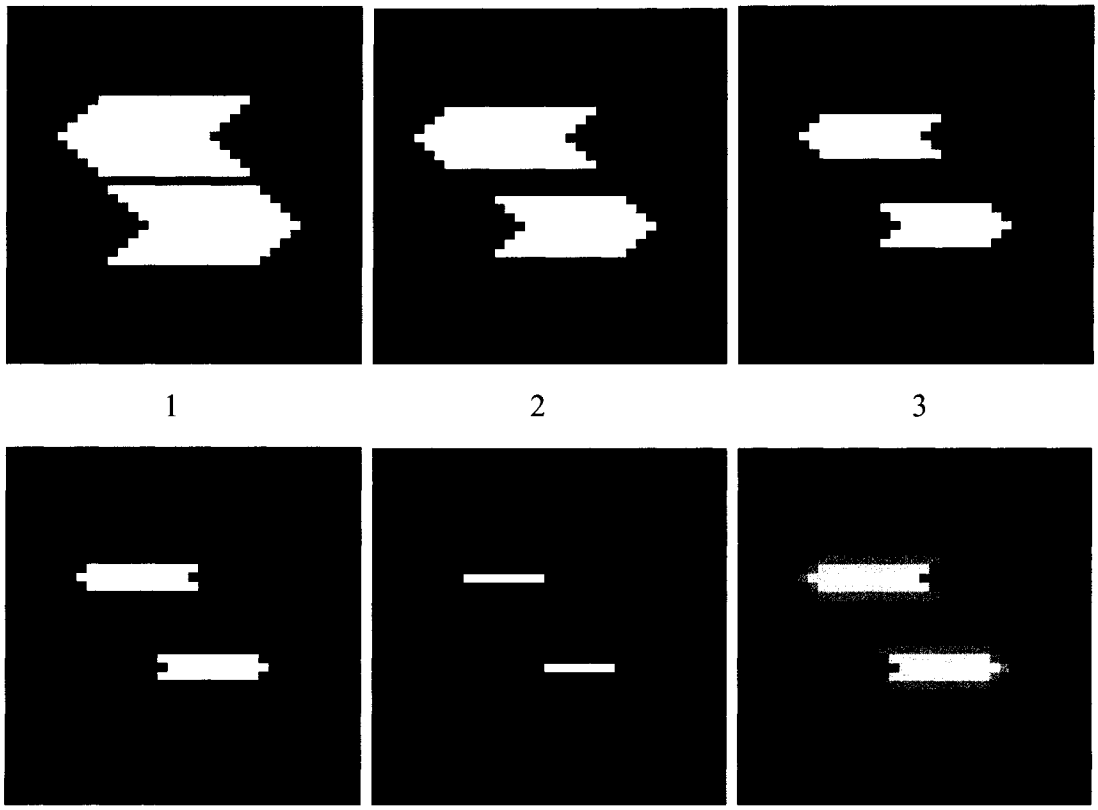

Figure. 2-2 A pictorial demonstration of how five static subfields (images 1-5) are summed together to create one shaped and intensity modulated field (image 6). In this demonstration all subfields are given equal weight.

the dose delivery is defined by the minimum distance of leaf travel and the physical width of each leaf. The use of sub-fields to create intensity modulated fields' results in a very large number of parameters which must be optimized to create an IMRT treatment plan. The large number of parameters requiring optimization makes forward treatment planning impractical for general IMRT. Consequently IMRT is generally associated with inverse treatment planning. The first step of the inverse treatment planning process involves using three dimensional image data of the patient to delineate the GTV, CTV, and PTV along with other points or volumes of interest such

as critical structures. In the next step the treatment planner specifies desired dose-volume constraints for the tumor and critical structure volumes that reflect the clinical objectives for the dose plan. Based on these specified dose-volume criteria, the treatment planning computer generates appropriate weights for its objective function, which it uses to evaluate how closely a given dose plan meets the specified clinical objectives. The planning computer then iteratively adjusts the intensity of each of beamlet with respect to the objective function until an acceptable treatment plan has been reached. In cases where an acceptable plan is not reached, dose-volume criteria are adjusted by the planner in an attempt to steer the computer's optimization algorithm towards a solution that meets the requirements of the radiation oncologist.

2.5.3 Helical TomoTherapy™

The mechanics of the HT delivery differ significantly from conventional step-and-shoot IMRT.[19] In HT the radiation field is an intensity-modulated slit beam. The slit beam is then rotated around the patient in a helical manner (i.e. the couch moves continuously while the radiation source rotates about the patient). The work in this thesis is focused on an HT unit called the Hi-Art 2 system [Tomotherapy Inc, Madison, WI]. It should be noted that although the term HT unit used in this thesis refers to the Hi Art 2 system, other helical type delivery systems are also under investigation.[20,21] The Hi Art 2 system is composed of a 5.7 MV linear accelerator which is mounted on a CT type gantry. A schematic of the HT unit is shown in figure. 2-3. Both the source to axis of rotation and the bore diameter on the Hi Art2 system are 85 cm (figure. 2-3).

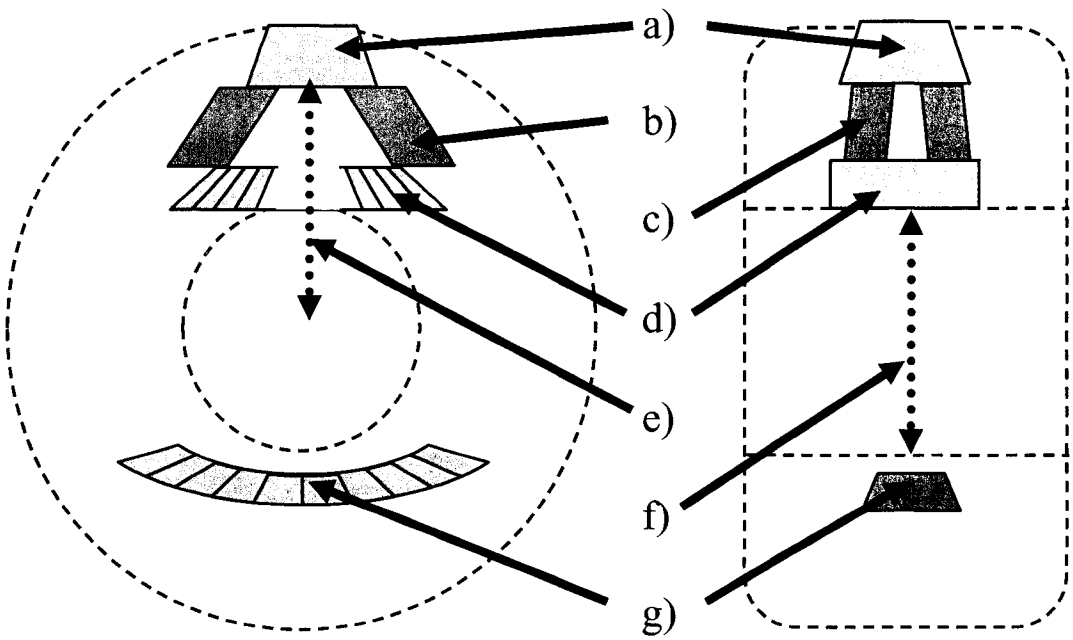

Figure. 2-3 A schematic diagram showing some of the major components of HT Hi Art 2 system. a) wave guide and target, b) x collimator, c) y jaws, d) binary MLC, e) 85 cm source axis distance, f) 85 cm bore diameter, g) MVCT detectors

The HT system is capable of producing a maximum field size of 5 X 40 cm^2 defined at the axis of rotation. For planning purposes, each 360 degree rotation is divided into 51 discrete angles which allows for a greater number of beam angles than are typically employed in linac based IMRT. At each beam angle the intensity is modulated using a pneumatically driven MLC with 64 leaves, each with a nominal width of 6.25 mm at the axis of rotation. The MLC employed in the HT unit is binary in the sense that the leaves are either completely open or closed. Any leaf may be opened for only a portion of each projection with a minimum leaf open time of 18 msec. A leafogram gives the relative duration of each leaf opening for every MLC leaf and every beam angle of a treatment plan.(figure. 2-4) The Hi Art 2 system also employs a megavoltage computed tomography (MVCT) system which allows for the

determination and correction of patient position with respect to the planning position. Other aspects of the HT unit which are important to this thesis are discussed in chapters 4 and 6.

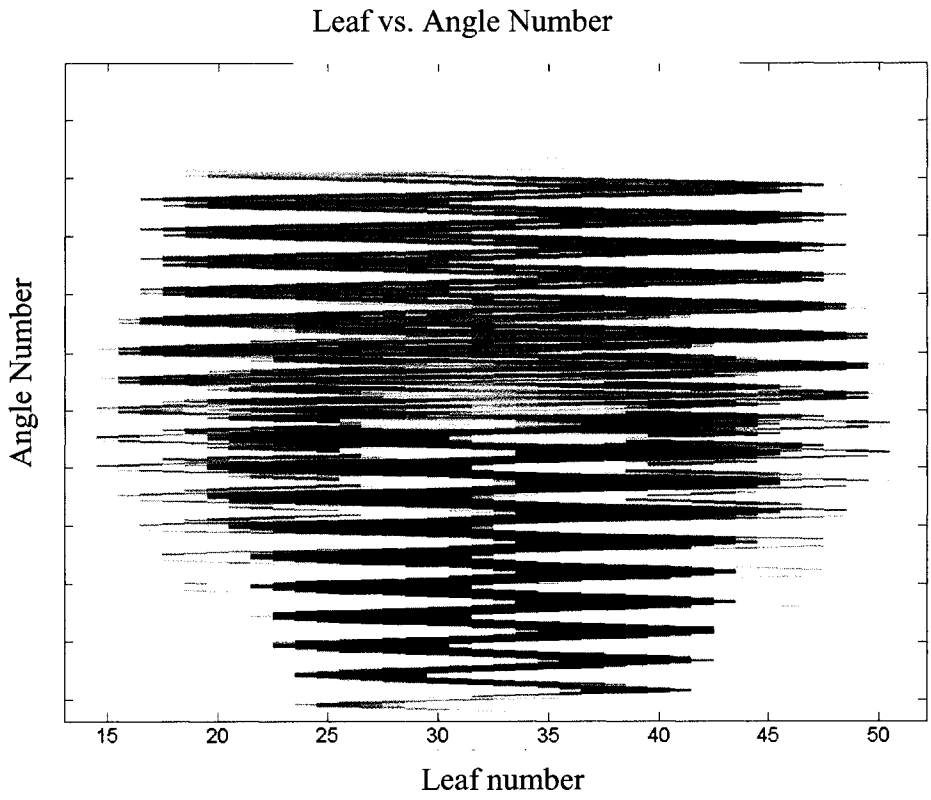

Figure. 2-4 A HT leafogram in which the beam angle number is listed in the y axis and leaf number is listed in the x axis. Black indicates the leaf is open for the entire beam angle and white indicates the leaf is closed for the duration of the beam angle and grey values indicate the leaf is open for part of the beam angle.

Due to the high complexity of IMRT and HT treatment plans, a comparatively high degree of vigilance is required from the medical physicist in assuring that the radiation treatment plan will deliver the dose as calculated. This process of delivery verification is treated in some depth in chapter 5.

2.5.4 Brachytherapy

Brachytherapy involves the use of sealed radioactive sources in close proximity to the tumor. Sources are chosen according to their particle type, energy and half life [23] (table 1-1) and are arranged to create a geometrically specific 3 dimensional dose pattern. Radiation effects are well localized in brachytherapy because of the ability to place these sources within very close proximity to the diseased tissue. There are four general brachytherapy techniques: [25]

1) Intracavitary brachytherapy involves the placement of the radiation source within a body cavity via a custom designed applicator. This technique is commonly used for gynecological tumors and represents the most widely performed brachytherapy procedure.
2) Intraluminal brachytherapy is a technique in which the radiation source is placed within the lumen of a vessel. This technique is often used to treat blood vessels, the esophagus, bronchus or the bile duct.
3) Surface molds and Plaques (forms used to hold specific arrays of seeds) for brachytherapy in which sources are placed upon the tumor surface instead of within the tumor. In this technique the source arrangement is accomplished using custom designed plaques or molds. This technique is the least used of the four techniques.
4) Interstitial Brachytherapy involves placement of sources within tissues. The most common site for this technique is the prostate. This type of brachytherapy is the subject of chapters 7 and 8.

Table. 2-1 Radionuclides employed in brachytherapy treatments [23]

Radionuclide	Half Life	Particle	Principal or Mean Energy (MeV)
Radium-226	1622 years	Photon	0.830
Cesium-137	30 years	Photon	0.662
Iridium-192	74 days	Photon	0.380
Gold-198	2.7 days	Photon	0.412
Iodine-125	60 days	Photon	0.028
Palladium-103	17 days	Photon	0.021
Strontium-90	29 days	Electron	0.50
Ytterbium-90	64 hours	Electron	2.27
Phosphorous-32	14 days	Electron	1.71
Californium-252	2.65 years	Neutron	2.15

Brachytherapy treatments are further classified with respect to the dose rate used and treatment duration. The wide range of dose rates used in brachytherapy has been categorized into three groups:[26] low dose rate (LDR) defines the dose rates between of 0.4 and 2.0 Gy/hr, medium dose rate (MDR) defines the dose rates between 2 and 12 Gy/hr and finally high dose rate (HDR) defines dose rates above 12 Gy/hr. In pulsed dose rate (PDR) brachytherapy, a sealed radioactive source which is capable of delivering medium dose rates of ~5Gy/hr is inserted into the diseased site for a fraction of an hour each hour to give a biologically equivalent lower dose rate (usually in the LDR range). The final categorization deals with the duration of the treatment and is divided into permanent implants and temporary implants. Like the name suggests, permanent implants are implanted permanently into the tumor. They typically employ

short half life radio isotopes [e.g. ^{125}I and ^{103}Pd, with half lives of 57.4 days and 17 days, respectively] with the radioactivity decaying to a safe level within a couple of weeks or months. In a temporary implant the radioactive source is moved into or into close proximity to the tumor until the desired dose has been delivered, and it is then removed.

In the last decade, imaging has played an increasing role in brachytherapy both in treatment planning and delivery assessment. Current pre-implant dose planning allows for three dimensional dose distributions to be assessed and modified as per the images of patient anatomy. Three dimensional source localization techniques employing tomographic images allow for 3 dimensional dose distributions of the delivered treatment to be assessed.[26]

2.6 Thesis Objectives: Assessment of dose delivery

This thesis deals with several aspects for the assessment of dose delivery of both external beam radiation therapy and prostate seed brachytherapy. Part 1 of the thesis deals with assessing dose delivery from the Hi Art 2 HT unit. A Monte Carlo derived TG-51 calibration for HT is established allowing for a higher degree of accuracy when making ion chamber dose measurements of the radiation output from the HT system. The three-dimensional dose distributions resulting from the delivered plans on the Hi Art 2 system are measured using EDR2 film and an ion chamber in order to compare with the calculated dose distributions.

Part 2 of the thesis deals with two aspects pertaining to the use of the MRI modality for post implant dosimetric evaluation of prostate brachytherapy plans. Susceptibility information is used to map the local magnetic-field distortions around each particular brachytherapy seed. The magnetic distortion map is then used to model the slice selection and the frequency encoding of the signal around the seed. The MRI artifacts which result from the spatial encoding processes can then be predicted and simulated. Unlike the case of an MRI image, the exact location of the seed is known *a priori* in the model. This evaluation provides information as to the seed location within the artifact pattern present in MR images of brachytherapy seeds for spin echo acquired images. 3.0 T MRI scanners with their associated increase in signal to noise ratio (SNR) allow for increased resolution which may help resolve the issues of seed location uncertainty. This increase in resolution may however be offset by a subsequent increase in the MR artifact size. To evaluate this a brachytherapy seed is suspended in a 3% by weight porcine gel and is scanned using both gradient echo and spin echo pulse sequences at both 1.5 T and 3.0 T. General artifact characteristics such as the maximum length and width as well as the volume are determined at various slice thicknesses. This is done to asses the feasibility of performing post implant dosimetric evaluations at the higher 3.0 T field. We have published versions of chapters 3, 4 and 5 as articles[28-30]

References

[1] Canadian Cancer Society, Cancer glossary, http://www.cancer.ca (2003)

[2] ASTRO, Radiation Therapy for Cancer: Facts to Help Patients Make an Informed Decision, (2004)

[3] Statistics Canada,Health Statistics. http://www.statscan.ca/ (2005)

[4] J.W.amd E.J. Sondik, Person-years of life lost due to cancer in the United States. 1970 and 1984" Am. J. Public Health **79** 1490-1493 (1989)

[5] National Cancer Institute of Canada, Canadian Cancer Statistics http://ncic.cancer.ca (2004)

[6] CancerBACUP, Booklet series. http://www.cancerbacup.org.uk (2002)

[7] J. VanDyk, "Radiation Oncology Overview" in *The Modern Technology of Radiation Oncology,* edited by J. VanDyk Medical Physics Publishing, Madison Wisconsin, 1-17 (1999)

[8] E.J. Hall, *Radiobiology for the radiologist*, William & Wilkins, Lippincott, Philadelphia (2000)

[9] L.W. Brady, S. Kramer S.H Levitt, R.G. Parker and E.W. Powers, "Radiation Oncology: contribution of the United States in the last years of the 20th century," Radiology **219**, 1-5 (2001)

[10] ICRU, "Prescribing Recording and Reporting Photon Beam Therapy," ICRU Report 50, ICRU, Washington D.C. (1993).

[11] ICRU, "Prescribing Recording and Reporting Photon Beam Therapy (Supplement to ICRU 50)," ICRU Report 62, ICRU, Washington D.C. (1999)

[12] T. Mizowaki, G. N. Cohen, A.Y. C. Fung, M. Zaidler, "Towards integrating functional imaging in the treatment of prostate cancer with radiation: Registration of the MR spectroscopy imaging to untrasounds/CT images and its implementation in treatment planning" Int. J. Radiation Oncology **54,** 1558-1564 (2002)

[13] R. Sinha, N. Pervez et al. "Multimodality biological imaging alters target definition compared to conventional target definition in Glioblastoma Multiforme." Radiotherapy and Oncology **76** # 209 September (2005)

[14] F.M. Khan. *The Physics of Radiation Therapy.* William & Wilkins Baltimore, Maryland (1994)

[15] R. Urtasun, "Technological improvement and local tumor control," in *Teletherapy: Present and Future*, edited by T.R. Mackie and J.R. Palta. AAPM Advanced Medical Publishing, Madison Wisconsin, 1-12 (1996)

[16] R.F. Bush, *Malignancies of the Ovaries Uterus and Cervix.* London Edward Arnold (1979)

[17] H. Kaplan *Hodgkin's Disease 2ed.* Harvard University Press, Cambridge Massachusetts, (1980)

[18] A.Brahme, "Dosimetric precision requirements in radiation therapy, " Acta Radiologica Oncology **23** 379-391 (1984)

[19] T. R. Mackie, T. Holmes, S. Swerdloff et al., "Tomotherapy: a new concept for delivery of dynamic conformal radiotherapy," Med. Phys. **20** 1709-1719 (1993).

[20] S. Webb "Intensity modulated radiation therapy: Dynamic MLC (DMLC) therapy, multisegment therapy and tomotherapy – and example of QA in DMLC therapy," Strahlentherapie Und Onkologie **174** 8-12 (1998)

[21] N. Chng, A.T. Kerr, MV Rogers, J. Shreiner, "Development of inverse planning and limited angle CT reconstruction for Cobalt-60 Tomotherapy" in the COMP Proceedings of the 51st annual scientific meeting. 235-237 (2005)

[22] R. Mohan, "Intensity modulation in RadioTherapy," in *Teletherapy: Present and Future*, edited by T.R. Mackie and J.R. Palta. AAPM Advanced Medical Publishing, Madison Wisconsin, 761-803 (1996)

[23] R. Nath. "Sources and Delivery Systems I: Radionuclides" *in Brachytherapy Physics Second Edition*, edited by B.R. Thomadsen, M.J. Rivard, W.M. Butler. AAPM Advanced Medical Publishing, Madison Wisconsin 25-30 (2005)

[24] R. Nath. "Overview of Brachytherapy Physics" *in Brachytherapy Physics Second Edition*, edited by B.R. Thomadsen, M.J. Rivard, W.M. Butler. AAPM Advanced Medical Publishing, Madison Wisconsin, 1-6 (2005)

[25] ICRU, "Dose and Volume Specificatin for Reporting Intracavitary Therapy in Gynecology," ICRU, Washington D.C. (1985).

[26] J. Rownd, "Localization II: Volume Imaging Techniques and Accuracy in Brachytherapy" *in Brachytherapy Physics Second Edition*, edited by B.R. Thomadsen, M.J. Rivard M.J. , W.M. Butler. AAPM Advanced Medical Publishing, Madison Wisconsin, 187-200 (2005)

[27] J. L.E. Williams, A, Liu and G.Wong "Monoclonal Antibodies and Other Internal Emitter Therapies" in the *The Modern Technology of Radiation Oncology,* edited by J. Van Dyk. Medical Physicis Publishing, Madison Wisconsin, 1021-1042 (1999)

[28] S.D. Thomas, M. Mackenzie, D.W. Rogers, B.G. Fallone. "A Monte Carlo derived TG-51 equivalent calibration for helical tomotherapy" Med.Phys. **32** 1346-1353 (2005)

[29] S.D. Thomas, M. Mackenzie, C.G. Field, A.M. Syme, B.G. Fallone. "Patient specific treatment verifications for helical tomotherapy treatment plans" Med. Phys. **32** 3793- 3800 (2005)

[30] K. Wachowicz, S.D. Thomas, B.G. Fallone, "Characterization of the susceptibility artifact around a prostate brachytherapy seed in MRI," Med. Phys. **33** 4459-4467 (2006)

Part 1

Delivery Verification with Respect to External Beam Radiation Therapy.

Chapters 3-4

Chapter 3: A TG-51 Calibration for Helical TomoTherapy™

3.1 Introduction

HT is a relatively new modality for delivering IMRT and as such needs a method of dose output calibration. The recommended procedure for absorbed dose to water calibration in the photon beams of conventional linear accelerators in North America is given in the AAPM's TG-51 protocol.[1] The procedure is based on an ion chamber calibrated in a reference ^{60}Co beam at a standards laboratory and is described in greater depth in appendix A. HT,[1] as a clinical modality for EBRT, requires the accurate calibration of absorbed dose to water per monitor unit of delivered radiation. The quality conversion factor, k_Q, has been calculated and tabulated in the TG-51 protocol as a function of the $\%dd(10)_x$ in water from the photon component of the beam at a SSD of 100 cm for a field size (FS) of 10x10 cm^2.(ref 2) Throughout this chapter this measurement set-up is referred to as the TG-51 reference conditions, and $\%dd(10)_x$ is typically referred to as the beam-quality specifier. The current $\%dd(10)_x$ lookup-table for k_Q is not suitable for the HT unit because the TG-51 reference conditions cannot be realized due to the physical design of the HT unit and, to a lesser extent, the differences in beam quality for the same mean electron energy impinging on the target (also due to the physical design of the HT unit).

The physical design of the HT unit imposes a maximum field dimension of 5 cm along the axis of the bore measured at the standard distance of isocenter (85 cm) from the source, instead of the 10 cm for which the data is tabulated in the TG-51 protocol. Furthermore, for HT, the bore diameter is 85 cm, and the maximum couch-to-isocenter distance (the distance from the top of the treatment couch to the rotational

isocenter) is approximately 28.5 cm. It thus becomes impractical to use 100 cm SSD and 10 cm depth for calibration as required by TG-51, because this would leave at most a few centimeters for back scatter.

The quality of the beam in the HT unit is different from other medical linear accelerators with similar mean incident electron energies (6 MeV) because of the absence of a flattening filter. The HT unit is inherently designed for IMRT treatments and uses its own MLC to modulate the beam. Since the beam can always be modulated it does not use a flattening filter because this would attenuate useful photons and result in prolonged treatment times. The absence of a flattening filter produces some appreciable differences in the beam's photon spectrum compared to conventional medical linear accelerators that employ flattening filters. The ion chamber measured transverse beam profile from the HT unit is significantly different from the cross-plane beam profile from a conventional 6 MV medical linear accelerator (figure. 3-1(a)). The "house" shaped HT profile is due to the unfiltered bremstrahlung distribution.[3] The Monte Carlo calculated energy spectrum of the HT unit photon beam is quite different from our calculation of the Varian 2100EX (Varian 21EX) conventional 6 MV medical linear accelerator and comprises a larger proportion of low-energy photons (figure. 3-1(b)) due to reduced beam hardening resulting from the absence of a flattening filter. The differences in spectrum and the difference in scatter from regions off the central axis, result in a depth-dose curve which differs from that of a conventional medical linear accelerator under the same measurement conditions. In this work, a new $\%dd(10)_x$ conversion function is

determined for use with the TG-51 protocol which accounts for the differences in both the reference geometry and the beam characteristics of HT.

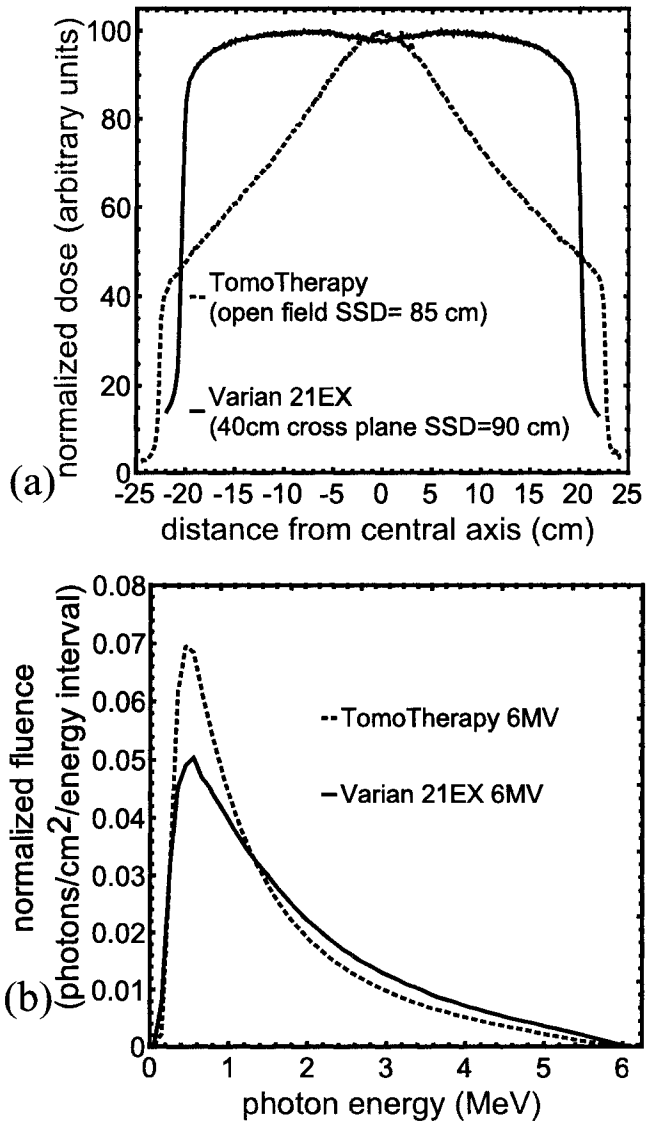

Figure. 3-1(a) Measured beam profiles normalized to the maximum absorbed dose for a HT open field at SSD=85 cm and the Varian 21EX in 40 cm wide cross plane at SSD = 90 cm. Both profiles are taken at 10 cm depth. The differences in SSD in the graph are unimportant as this is meant only as a qualitative comparison.

(b) Our Monte-Carlo calculated differential energy spectra of the full phase space file for the HT 6.0 MeV mean incident electron energy and the Varian 21EX. Both are scored in air for 5x10 cm^2 field at 85 cm SSD. The fluence was normalized such that the total fluence within the spectrum is equal to 1.

3.2 Methods and Materials

3.2.1 Ion Chamber

We used an Exradin A1SL [Standard Imaging, Middleton, WI] waterproof ion chamber with 1.1 mm walls of C552 air-equivalent plastic because its small volume (0.056 cm^3) minimizes volume averaging which could arise from the non-flat beam profile (figure. 3-1(a)). The Exradin A1SL (A1SL) ion chamber has a cavity diameter of 4.05 mm and a length of 4.4 mm. The central electrode of the ion chamber is also comprised of C552 air equivalent plastic.

3.2.2 k_Q

The quality conversion factor, k_Q, which converts a ^{60}Co absorbed dose calibration coefficient into one suitable for the HT beam is given by:[4]

$$k_{Q[HT\ TG\text{-}51]} = \frac{\left[\left(\bar{L}/\rho\right)_{air}^{water} P_{wall}P_{repl}P_{cel}\right]_{HT(SSD=85cm,\ fs=5X10cm^2,\ depth=10cm)}}{\left[\left(\bar{L}/\rho\right)_{air}^{water} P_{wall}P_{repl}P_{cel}\right]_{^{60}Co(SSD=100cm,\ fs=10X10cm^2,\ depth=10cm)}}, \qquad 3.1$$

where $\left(\bar{L}/\rho\right)_{air}^{water}$ is the ratio of mean restricted mass collision stopping power (spr) in water to that in air. P_{wall} is a correction factor that accounts for dose perturbations caused by the presence of the ion chamber wall material in the radiation field as described in appendix A. P_{repl} is a correction for fluence and gradient perturbations due also to the presence of the ion chamber cavity in the radiation field. In practice, P_{repl} for dose measurements in broad photon beams may be accounted for by using

an effective point of measurement. The correction factor P_{repl} is inherently contained in all of our calculations of k_Q. Thus dose determination for the HT unit will not require a shift in the reference position of the ion chamber after the initial measurement of $\%dd(10)_x$. P_{cel} is the correction accounting for the presence of the central electrode within the ion chamber. In the case of the A1SL, where the ion chamber central electrode is made of the same material as the ion chamber wall, P_{cel} is accounted for within P_{wall}. The k_Q for the A1SL is not included in the TG-51 document. We have thus calculated k_Q for the A1SL under the TG-51 reference conditions (figure. 3-2). The calculations for k_Q were made in the same manner and using the same data sources that are used in TG-51.[4-9]

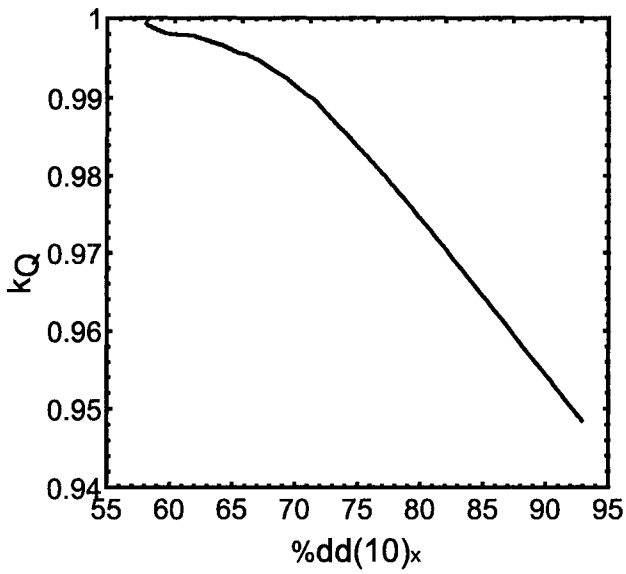

Figure. 3-2 Values of k_Q for the Exradin A1SL ion chamber as a function of $\%dd(10)_x$ are shown. These values are for conventional medical linear accelerators with a $\%dd(10)_x$ measurement made using the standard TG-51 reference conditions of SSD=100 cm and a 10x10 cm^2 field defined at the surface distance.

P_{wall} was determined using equation 3.2: [4]

$$P_{wall} = \frac{1}{\left(\bar{L}/\rho\right)_{air}^{water}\left[\alpha\left(\bar{L}/\rho\right)_{C552}^{air}\left(\overline{\mu_{en}/\rho}\right)_{water}^{C552} + (1-\alpha)\left(\bar{L}/\rho\right)_{water}^{air}\right]}, \qquad 3.2$$

where $\left(\bar{L}/\rho\right)_{C552}^{air}$ is the air-to-C552 ratio of mean restricted mass collision stopping powers, α is the fraction of ionization arising from electrons originating in the ion chamber wall, and $\left(\overline{\mu_{en}/\rho}\right)_{water}^{C552}$ is the C552-to-water ratio of mean mass energy absorption coefficients. All values required in the determination of k_Q were modeled for a ^{60}Co unit, a Varian 21EX 6 MV [Varian, Palo Alto, CA] medical linear accelerator as well as an HT unit (Siemens accelerator, proprietary collimator / MLC) at five different mean incident electron energies. In each case, the phase space file of the incident photon beam was determined using the BEAMnrc user code.[10,11] The Varian 21EX 6MV medical linear accelerator was modeled to test the basic accuracy of the calculations and to ensure the congruence of our methods with those of TG-51. Starting from Eq. (3.1) the calculation of k_Q for HT is based on:

$$k_{Q[HT\ TG\text{-}51]} = \frac{\left[\left(\bar{L}/\rho\right)_{air}^{water} P_{wall}\right]_{HT\ Calculated}}{\left[\left(\bar{L}/\rho\right)_{air}^{water} P_{wall}\right]_{Varian\ 6\ MV\ Calculated}} k_{Q[TG\text{-}51\ \%dd(10)x\ =66.6\%]}, \qquad 3.3$$

In this equation, the ratio of our calculated $\left(\bar{L}/\rho\right)_{air}^{water}$ P_{wall} is used to scale the TG-51 k_Q calculation of $\%dd(10)_x$= 66.6% for the Varian 21EX. This allows us to deal with minor discrepancies between our calculations and those of TG-51 by using our results only as a scaling factor for the TG-51 values. Equation 3.3 follows from Eq. (3.1) with the assumption that $P_{repl[HT]} = P_{repl[Varian\ 6\ MV]}$. This assumption is largely true for the A1SL ion chamber, for nominal accelerator potentials ranging from 4 MV to 6 MV[12] as the difference in P_{repl} for a 4 mm diameter chamber between 4 MV and 6 MV nominal accelerator potentials is only 0.02%.[7] There are indications that P_{repl} may change in very small IMRT beams,[13] but we further assume this is not an issue for the 5x10 cm^2 field used here. Thus the assumption of an invariant P_{repl} will result in a possible maximum error of 0.02% in our values of k_Q for HT. Using Eq. (3.3) instead of Eq. (3.1) corrects our data (as shown in the results section below) by 0.35% due to the reasons listed above as well as the inclusion of the P_{repl} correction which we have not calculated independently of Eq. (3.3). We determine k_Q as a function of the calculated value of $\%dd(10)_x$ under our HT reference conditions of a 5x10 cm^2 field at 85 cm SSD ($\%dd(10)_{x\ [HT\ Ref]}$) for different incident beam energies. The calculated values of k_Q are used to look up the equivalent value of $\%dd(10)_{x[HT\ TG\text{-}51]}$ (i.e. the equivalent value for TG-51 reference conditions that would give the same value of k_Q) for each simulated mean incident electron energy of the HT unit (see the results section below). A third order polynomial is then fit between the values of $\%dd(10)_{x[HT\ TG\text{-}51]}$ and $\%dd(10)_{x[HT\ Ref]}$.

3.2.3 Monte Carlo Calculations

The Monte Carlo method is described in some depth in appendix B.

3.2.3.1 BEAM Modeling Parameters

Modeling of all radiation sources was performed using the BEAMnrc user code.[10] The HT unit was modeled for mean incident electron energies of 6.25, 6.0, 5.75, 5.5 and 5.25 MeV. The electron inputs for the HT models used a Gaussian electron energy spread with a full width at half the maximum amplitude value (FWHM) of 12%; this is the same FWHM as used for other Siemens machines.[14] The effect of beam focal spot size on %dd was investigated, but as with conventional linear accelerators, the HT %dd was found to be insensitive to focal spot size.[14] The sensitivity of sprs to focal spot size was also investigated and, as with %dd, were found to be insensitive. The incident electron spatial distribution used for the six bremsstrahlung beams was a radial Gaussian function with a FWHM of 1.41 mm; this FWHM is a typical value.[15-17] Phase space data for the HT unit were generated at 85 cm from the source for a FS of 5x10 cm^2 defined at the surface of the phantom. A Gaussian incident electron energy spread with mean energy of 3% FWHM[14] and 6 MeV respectively was used for the Varian 21EX model. Phase space data for the Varian 21EX were generated at both 100 cm for a 10x10 cm^2 field and at 85 cm for a 5x10 cm^2 field. The latter scoring was done to investigate the effects of the reference conditions on the variables within k_Q. Range rejection with an ESAVEIN value of 1.5 MeV was used everywhere except the target where an ESAVEIN value of 0.7 MeV was used.[11] Selective bremsstrahlung splitting was also used for variance reduction.[18] For the ^{60}Co unit, a point source was

used with the ^{60}Co energy spectrum supplied with the EGS distribution.[19] The ^{60}Co unit phase space data were generated at 100 cm for a 10x10 cm^2 field. In modeling the radiation sources, values of ECUT and PCUT were 0.7 MeV and 0.01 MeV respectively.[11] Although the HT energy spectrum has a higher contribution of low energy photons, the increase in the very low part of the spectrum (i.e. below 100 keV) is insignificant from that of a conventional 6 MeV linear accelerator and thus the EGSnrc codes are expected to provide accurate results. The physical geometry of each of the treatment unit heads (i.e. relative positions of the target, collimator, jaws, MLC, ion chamber and the flattening filter of the Varian 21EX) was modeled according to schematics provided to us by Varian Inc. and TomoTherapy Inc. Materials information required to generate data needed for the Monte Carlo calculations (i.e cross sections, mean free paths and electron stopping powers) of each of the treatment heads modeled was also provided by Varian Inc and TomoTherapy Inc.

3.2.3.2 The value of %dd(10)$_x$ and Beam Profiles

The value of %dd(10)$_x$ and beam profile were modeled using the DOSXYZnrc user code.[20] The %dd(10)$_x$ calculations were performed in a 30x30x30 cm^3 virtual water phantom. For HT, energy deposited was scored in 4x4x1 mm^3 voxels (1 mm along the beam's central axis, 4 mm in the directions orthogonal to the beam). For ^{60}Co and Varian 21EX, where the beam profile is much flatter, the cross section of the scoring voxels was 20x20x1 mm^3. Range rejection was employed with an ESAVIN value of 0.8 MeV. DOSXYZnrc's non-uniform padding around the scoring voxels was also used. ECUT and PCUT were set to 0.7 MeV (the range of a 189 keV electron in

water is approximately 0.4 mm which is less than 1/3 the mean distance across the smallest scoring voxel) and 0.01 MeV, respectively.[11] The maximum amplitude of the beam profiles were determined by averaging the central 1.6 cm of the beam profile. The FWHM value of the measured and calculated beam profiles were determined by linearly interpolating between the adjacent data points.

All physical measurements were performed at the facilities of the Cross Cancer Institute. The value of $\%dd(10)_x$ was measured using the A1SL in a water tank of 30x30 cm^2 cross section and 20 cm depth. A shift of 1.2 mm (0.6 r_{cav}) upstream was applied to the depth-dose curve. The absorbed dose was integrated over a 10 second period at each depth. As HT does not servo the dose an in-air measurement was taken simultaneously in order to correct for any minor output variation from the HT unit.

Dose profiles were measured in a solid water phantom at a depth of 1.5 cm and SSD of 85 cm using Kodak EDR2 film. Film densities were converted to dose using a film calibration curve. A film calibration curve is a curve which relates the optical density of an irradiated film to the dose delivered to the film. Profile measurements were compared with the profiles calculated using the DOSXYZnrc code. In calculating the dose profiles, the energy deposited was scored in an array of 4x4x4 mm^3 voxels centered at 1.5 cm depth and aligned along both the long and short axes of the field. The dose profile along the long axis of a 5x40 cm^2 field was measured and calculated in order to tune the focal spot.[14]

3.2.3.3 Water-to-Air Stopping Power Ratio (spr)

The water-to-air spr for all seven photon beams modeled (HT at 5 mean electron input energies, the Varian 21EX and the ^{60}Co unit) was calculated using the SPRRZnrc user code.[21-23] The spr values were calculated in a virtual cylindrical water phantom of 20 cm radius and 30 cm depth. The simulated beam dimensions (5 X 10 cm^2) were significantly smaller than 20 cm. A cylindrical scoring voxel of 1 cm radius and 0.5 cm thickness was centered at a depth of 10 cm to determine the spr values at that depth. ECUT and PCUT were set to 0.521 MeV and 0.01 MeV respectively.[21]

3.2.3.4 Air-to-C552 spr

The air-to-C552 spr was determined for the seven different photon beams using the SPRRZnrc user code. A virtual cylindrical phantom of 20 cm radius was used. Cylindrical slabs of C552 3 cm thick (^{60}Co beam) and 5 cm thick (HT and Varian 21EX beams) were placed between 10 cm and 20 cm thick cylindrical slabs of water. The photon beams were incident on the surface of the first, i.e. 10 cm thick water slab. The cylindrical scoring voxel of 1 cm radius and 0.5 cm thickness was placed in C552 at a depth of 11.25 cm for the ^{60}Co beam and 12.25 cm for the HT unit and the Varian 21EX linear accelerator. This thickness of C552 was sufficient to ensure that the electrons for which the spr was determined were those originating in the C552. The 20 cm thickness of the second water slab following the C552 was used to allow for sufficient back-scattered photons. The α term in P_{wall} refers to the fraction of ionization arising from electrons originating in the ion chamber wall.[4] Since the ion-

chamber wall is made of C552, we are required to use the C552 slabs in water phantom for these calculations.

3.2.3.5 C552-to-Water Ratio of Mean Mass Energy Absorption Coefficients

In order to determine the ratio of mean mass energy absorption coefficients, the FLURZnrc user code[21] was used to determine photon fluence spectra in a cylindrical virtual water phantom of radius 20 cm and of thickness 22.5 cm. The fluence was calculated in a cylinder of radius 2.4 cm and thickness 5 cm centered at a depth of 10 cm along the beam central axis. This large scoring voxel was chosen to minimize the statistical uncertainty of the energy fluence. The difference in the photon spectrum of this larger sampling volume to the sampling volume used in the spr calculations was found to affect the mean mass energy absorption coefficient by less than 0.003%. The photon fluence was binned into 0.1 MeV intervals for the linear accelerator and HT unit and 0.01 MeV intervals for the ^{60}Co unit. The photon fluence was then used to weight the individual values of mass energy absorption coefficients μ_{en}/ρ of the medium:[24]

$$\left(\overline{\mu_{en}/\rho}\right)_{medium} = \frac{\int_0^{Emax} E \bullet \varphi(E) \left(\mu_{en}/\rho\,(E)\right)_{medium}\, dE}{\int_0^{Emax} E \bullet \varphi(E)\, dE} \qquad 3.4$$

where $\varphi(E)$ is the photon fluence spectrum. In the case where National Institute of Standards and Technology (NIST) gave no direct mean mass energy absorption

coefficient value for a corresponding energy bin, the mass energy absorption coefficient was interpolated on a log-log scale.[24] The water and C552 mean mass energy absorption coefficient values calculated from Eq. (3.4) were then used to calculate the ratio of mean mass energy absorption coefficients.

3.2.3.6 Determination of α

Values of α for the Varian 21EX and the ^{60}Co unit were obtained from Lempert et al.[8] using the value of $\%dd(10)_x$ as the beam quality specifier.[4] The results of the Lempert et al. experiment are widely used in various dosimetry protocols.[2,7,9,25] In the case of the HT calculations, the value of $\%dd(10)_x$ would not be an appropriate beam quality specifier for α due to both the difference in the measurement geometry and the beam quality. For the HT beams, the calculated value for the water-to-air spr was associated with what would be the TG-51 equivalent value for $\%dd(10)_x$.[5] This equivalent $\%dd(10)_x$ value was then used to determine α from the data of Lempert et al. as is done in TG-51.[4,8] The water-to-air spr was chosen as the beam quality transfer quantity since it represents the most rapidly changing parameter as a function of beam quality and it is relatively insensitive to geometric factors.[22]

3.3 Results and Discussion

3.3.1 Monte Carlo Calculations

3.3.1.1 The Value of $\%dd(10)_x$ and the Beam Profile

Calculated values of $\%dd(10)_x$ for the ^{60}Co and the Varian 21EX nominal 6 MV beam were 58.4(2)% and 66.6(2)%, respectively, whereas our measured values

are 58.6% and 66.7%, respectively. The calculated values of $\%dd(10)_{x[HT\ Ref]}$ were found to range between 58.8(3)% and 60.8(3)% for the range of energies simulated (see figure. 3-3(a) and table. 3-1). The statistical uncertainties in the last decimal place are given in brackets and represent one standard deviation. The measured value of $\%dd(10)_x$ for the HT unit at our centre was 59.5% indicating a mean incident electron energy of 5.63 MeV (figure. 3-3(a)). The value of $\%dd(10)_x$ for the Varian 21EX under the same reference conditions as our HT unit was calculated to be 62.7(2)% and measured to be 63.0%. Thus the change in reference conditions leads to a change of 3.9% in the value of $\%dd(10)_x$ for the Varian 21EX calculation. The calculated $\%dd(10)_x$ value of our HT Unit (6 MeV) mean incident electron energy was 60.4(3)%, and thus lower than what we calculated for Varian 21EX under the HT reference conditions. The difference in $\%dd(10)_{x[HT\ Ref]}$ obtained with a mean incident electron energy of 6 MeV to the $\%dd(10)_x$ obtained with the Varian 21EX under the HT reference conditions of 85 cm SSD and 5x10 cm^2 field is 2.3%. In comparing the measured and calculated beam profiles of the 5x10 cm^2 field, the calculated FWHM agrees with the measured FWHM to within 1.5 mm along the long axis and 0.05 mm along the short axis (figure. 3-3(b)). The calculated full width 80% maximum agrees with the measured to within 2 mm of the long axis and 2.3 mm of the short axis (figure. 3-3(b)). Also shown, is the long axis dose profile comparison for a 5x40 cm^2 field (figure. 3-3(b)).

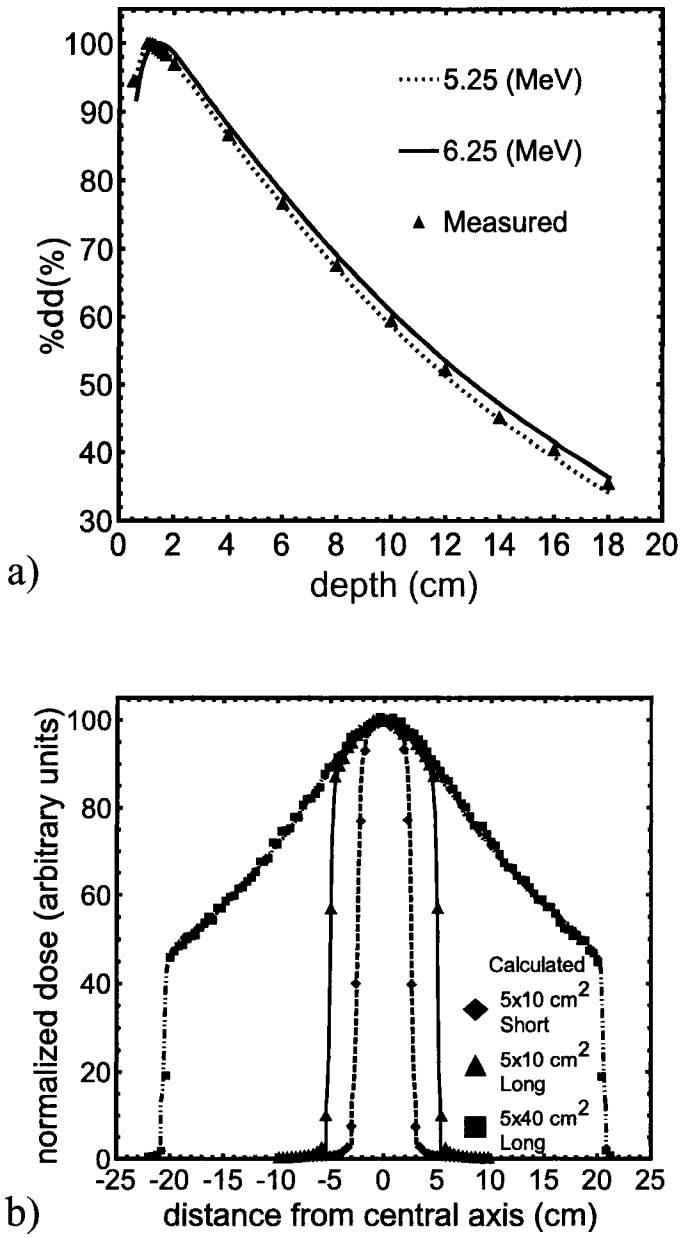

Figure. 3-3(a) The calculated percent depth dose curve of the 5.25 MeV and 6.25 MeV HT mean incident electron energy as compared to the measured percent depth dose. (b) The calculated absorbed dose profiles of the HT unit (5.5 MV) compared to the measured profiles of the HT unit. Measurements were made with Kodak EDR2 film. Lines are the measured data of their corresponding calculated values.

Table. 3-1 A comparison of values required for the %dd conversion. For the statistical error calculations of k_Q any error less than 0.0001 was rounded up to 0.0001. Error in the α value of P_{wall} or the TG-51 value of k_Q for the Varian 6 MV was not considered. The error in $\%dd(10)_{x\,[HT\ TG\text{-}51]}$ corresponds to the error in k_Q.

Mean Incident Electron Energy (MeV)	$\left[\left(\bar{L}/\rho\right)^{water}_{air} P_{wall}\right]^{HT\,Calc}_{Varian6MV\,Calc}$	$k_{Q\,[HT\ TG\text{-}51]}$	$\%dd(10)_{x\,[HT\ Ref]}$	$\%dd(10)_{x\,[HT\ TG\text{-}51]}$
5.25	1.0030(2)	0.9981(2)	58.8%(3)	59.8%(+16/-6)
5.50	1.0025(2)	0.9976(2)	59.2%(3)	62.2%(+7/-4)
5.75	1.0021(2)	0.9972(2)	59.8%(3)	63.0 %(+4/-5)
6.00	1.0017(2)	0.9967(2)	60.4%(3)	63.9%(+4/-4)
6.25	1.0012(2)	0.9963(2)	60.8%(3)	64.6%(+3/-3)

3.3.1.2 Calculation Accuracy

The water-to-air sprs for the ^{60}Co unit and the Varian 21EX conventional medical linear accelerator were found to be 1.1337(<1) and 1.1205(<1), respectively; these are within 0.02% and 0.06% of the values used by TG-51 in determination of k_Q[5] (table. 3-2). The air-to-C552 sprs for the ^{60}Co and 6 MV Varian 21EX linear accelerator were found to be 1.0040(1) and 1.0174(1), respectively. These values are within 0.08% and 0.06% respectively, of the values used by TG-51 in determination of k_Q[6,9] (table. 3-2). The C552-to-water ratio of mean mass energy absorption coefficients for the ^{60}Co and 6 MV linear accelerator were found to be 0.9003(<1) and 0.9018(<1), respectively. The calculated numbers agree to within 0.07% for ^{60}Co and 0.02% for the Varian

21EX with the values used in calculating k_Q for TG-51.[9] Our calculated values used in the definition of the wall correction factor given in Eq. (3.2) yield a value of P_{wall} for the A1SL of 0.9796 in a ^{60}Co beam and of 0.9829 for the Varian 21EX. Our P_{wall} values agree to within 0.12% for the ^{60}Co unit and 0.01% for the Varian 21EX to P_{wall} generated using the TG-51 data[5,9] (table. 3-3). It should be noted that the air-to-C552 spr and the C552 -to-water ratio of mean mass energy absorption coefficients for ^{60}Co agree to within 0.01% of more recent calculations[26,27] although our discrepancies with the corresponding TG-51 values are slightly larger.

Table. 3-2 A comparison of our Monte-Carlo calculated quantities and the corresponding TG-51 equivalents[5,9] to demonstrate the accuracy of our calculations. The values in the brackets are the statistical uncertainties of the last decimal place for the number that they append and represent 1 standard deviation. i.e. 1.1337(1) is equivalent to 1.1337±0.0001.

	^{60} Co Unit			6 MV Varian 21 EX %dd(10)$_x$ = 66.6%		
Quantity	Present	TG-51	%Diff	Present	TG-51	%Diff
$\left(\bar{L}/\rho\right)_{air}^{water}$	1.1337(<1)	1.1335	0.02%	1.1205(<1)	1.1212	0.06%
$\left(\bar{L}/\rho\right)_{C552}^{air}$	1.0040(<1)	1.0048	0.08%	1.0174(1)	1.0168	0.06%
$\left(\overline{\mu_{en}/\rho}\right)_{water}^{C552}$	0.9003(<1)	0.9009	0.07%	0.9018(<1)	0.9016	0.02%

3.3.1.3 Effect of Change in Reference Conditions

In this section, we determine the effect of changing the reference conditions on the dosimetric quantities for the Varian 21EX. This was done to determine what portion of the change in k_Q is due to the difference in measurement setup. To accomplish this, we compare the values of the water-to-air spr, air-to-C552 spr, as well as the C552-to-water ratio of mean mass energy absorption coefficients calculated for both the HT reference conditions and the TG-51 reference conditions. The water-to-air spr calculation using the Varian 21EX phase space data generated under HT reference conditions (5x10 cm^2 field at an 85 cm SSD) yielded a value of 1.1197(1). This value was 0.07% lower than our calculation for the same linear accelerator under TG-51 reference conditions. The decrease in spr indicates a slightly higher mean energy beam under the HT reference conditions. This is primarily because of the smaller FS with the HT reference conditions. The air-to-C552 spr which was calculated for the Varian 21EX under the HT reference conditions yielded a value of 1.0182(1), which is 0.08% greater than our calculated value for the TG-51 reference conditions. This increase further indicates a slightly greater mean energy of the beam in the Varian 21EX with HT reference conditions. The calculated C552-to-water ratio of mean mass energy absorption coefficients was identical under the two reference conditions. This is because this ratio is very insensitive to the difference in beam quality over the region of interest as compared to both the water-to-air spr and air-to-C552 spr.[9] When the same value of α (0.62) as used in TG-51 was used to calculate P_{wall} for the HT reference conditions, the value did not change. Finally, the $\left(\bar{L}/\rho\right)_{air}^{water} P_{wall}$ value for the Varian 21EX calculated under the HT reference

conditions differed from the value calculated under the TG-51 reference conditions by 0.07%, again indicating a higher energy beam. The major factor in the difference of the sprs values is the difference of the number of lower energy scattered photons when calculated using the different FS of the two reference conditions. The smaller FS has lower number of lower energy scattered photons (figure. 3-4).

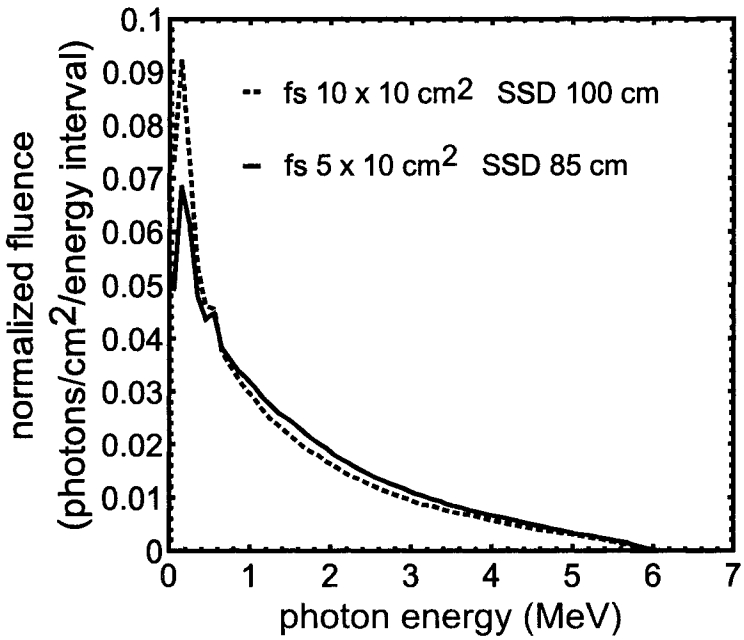

Figure. 3-4 The photon spectra (calculated in water at 10 cm depth) of the Varian 21EX 6 MV accelerator for two sets of reference conditions. These photon spectra are the same as used for the mean mass energy absorption coefficient calculation described in the methods section. The TG-51 reference conditions result in a higher contribution of low energy photons scattered in from the larger initial primary beam. Here the photon fluence from the FLURZnrc has been normalized such that the sum of the total fluence equals 1.

3.3.1.4 Helical TomoTherapy™ Results

The water-to-air spr values for the HT beam decreased by 0.3% as the mean incident electron energy varied from 5.25 to 6.25 MeV (see table. 3-3). The water-to-air spr for the 6.0 MeV mean incident electron energy is 0.25% greater than for the Varian 21EX under the same reference conditions. Over the same 5.25 to 6.25 MeV range, the air-to-C552 spr values for the HT calculations increased by 0.32% (see table. 3-3). The air-to-C552 spr value for the 6.0 MeV mean incident electron energy is 0.26% less than the value for the Varian 21EX under the same reference conditions. The HT calculations for the C552-to-water ratio of mean mass energy absorption coefficients increased by 0.04% as the mean incident electron energy varied from 5.25 to 6.25 MeV (table. 3-3). The calculated value for the HT beam for the 6 MeV mean incident electron energy was 0.04% less than that of the Varian 21EX under the same reference conditions. The value of α determined for the HT unit decreased by 9.7% as the mean incident electron energy increased from 5.25 to 6.25 MeV (table. 3-3). The calculated value of α for a 6.0 MeV mean incident electron energy beam on the HT unit was 3.2% greater than the calculated value for the Varian 21EX. This difference affects the value of P_{wall} by 0.1%. Using these values in Eq. (3.2), P_{wall} was found to increase from 0.9819 to 0.9831 with an increase of mean incident electron energy from 5.25 to 6.25 MeV (table. 3-3). The HT-to-Varian 21EX ratio of the $\left(\bar{L}/\rho\right)_{air}^{water} P_{wall}$ product was found to decrease by 0.18% as the mean incident electron energy increased from 5.25 to 6.25 MeV (table. 3-1). When multiplied by the Varian 21EX TG-51 value for k_Q, the HT calibration value of k_Q decreased from 0.9981 to 0.9963 as the mean incident electron energy increased from 5.25 MeV to 6.25 MeV

(table. 3-1). These values of k_Q for the HT unit correspond to values of $\%dd(10)_{x[HT\ TG\text{-}51]}$ that range from 59.8% to 64.6% (table. 3-1). These values of $\%dd(10)_{x\ [HT\ TG\text{-}51]}$ were plotted (figure. 3-5) versus the original DOSXYZnrc determined $\%dd(10)_{x\ [HT\ Ref]}$ and fit to a third order polynomial expressed by Eq. (3.5).

$$\%dd(10)_{x[HT\ TG\text{-}51]} = 1.35805\times\%dd(10)_{x[HT\ Ref]}^{3} - 244.493\times\%dd(10)_{x[HT\ Ref]}^{2} + 14672.98\times\%dd(10)_{x[HT\ Ref]} - 293479.4. \qquad 3.5$$

The maximum error in the fit of Eq. (3.5) is 0.3% which results in an error of 0.02 % in k_Q. This is obtained by inspecting the maximum slope in the region of interest of the graph of figure. 3-2 with $\%dd(10)_{x[HT\ TG\text{-}51]}$ on the "x-axis". It should be noted that this conversion equation is only valid for $\%dd(10)_{x[HT\ Ref]}$ between 58.8% and 60.8% as outside this range the polynomial changes drastically.

Table. 3-3 The Monte-Carlo calculated quantities required for the determination of P_{wall} and k_Q for different mean incident electron energies of the HT unit. The calculations are carried out under the reference conditions of 85 cm SSD and a 5x10 cm^2 field.

Mean Incident Electron Energy (MeV)	$\left(\bar{L}/\rho\right)^{water}_{air}$	$\left(\bar{L}/\rho\right)^{air}_{C552}$	$\left(\overline{\mu_{en}/\rho}\right)^{C552}_{water}$	α	P_{wall}
5.25	1.1250(1)	1.0132(1)	0.9011(<1)	0.68	0.9819(1)
5.50	1.1240(1)	1.0141(1)	0.9012(<1)	0.66	0.9823(1)
5.75	1.1233(1)	1.0148(1)	0.9013(<1)	0.65	0.9825(1)
6.00	1.1225(1)	1.0155(1)	0.9014(<1)	0.64	0.9827(1)
6.25	1.1216(1)	1.0164(1)	0.9015(<1)	0.62	0.9831(1)

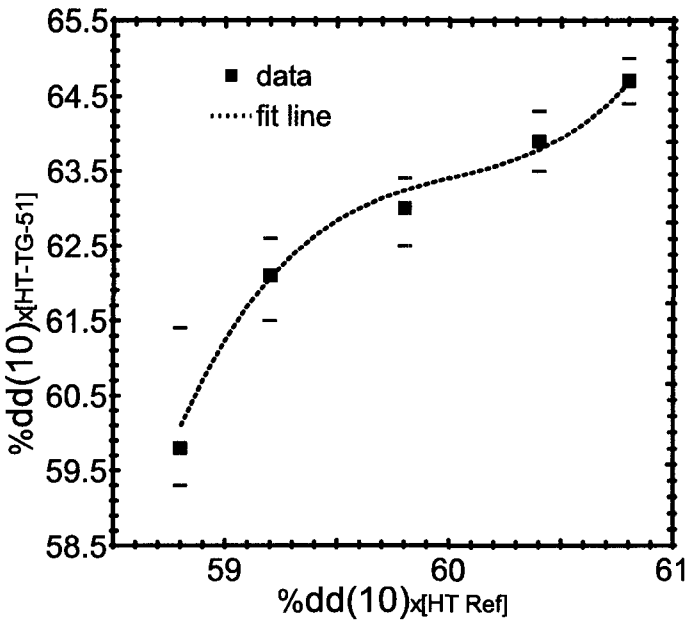

Figure. 3-5 $\%dd(10)_{x\ [HT\ TG-51]}$ versus $\%dd(10)_{x\ [HT\ Ref]}$ for the Exradin A1SL ion chamber. The error bars for the $\%dd(10)_{x\ [HT\ TG-51]}$ correspond to the error in k_Q that was used to determine $\%dd(10)_{x\ [HT\ TG-51]}$.

3.3.2 Summary

In the following , we list a step-by-step protocol procedure for incorporating this work into the TG-51 protocol.

1) Using the A1SL, measure $\%dd(10)_{x[HT\ Ref]}$ in water under the reference conditions of SSD = 85 cm and FS = 5x10 cm^2 defined at the phantom's surface. This measurement should incorporate the appropriate chamber shift as described in the TG-51 protocol
2) Determine $\%dd(10)_{x[HT\ TG\text{-}51]}$ from $\%dd(10)_{x[HT\ Ref]}$ using either Eq. (3.5) or figure. 3-5. The result should be an increase in $\%dd(10)_x$ of between 0.6% and 3.8%.
3) Apply TG-51 as written, using $\%dd(10)_{x[HT\ TG\text{-}51]}$ determined in step 2.

Note: as the standard k_Q for the A1SL ion chamber is not included in the TG-51 document, the k_Q listed in figure. 3-2 may be used.

3.4 Conclusions

Due to the design of the HT unit, setting the TG-51 reference SSD of 100 cm is impractical and the reference field of 10x10 cm^2 is impossible. This reference set up is required for the measurement of $\%dd(10)_x$ used for the k_Q look up table in the TG-51 protocol. In addition, the absence of a flattening filter within the HT unit also makes the beam different in terms of both beam flatness and energy spectrum from that of conventional medical linear accelerators. For these reasons, a $\%dd(10)_x$ conversion for

the Exradin A1SL has been created to allow for an HT unit $\%dd(10)_x$ measured under the reference conditions of 85 cm SSD and 5x10 cm^2 field to be converted to an equivalent $\%dd(10)_x$ to determine k_Q within the TG-51 protocol. The value of $\%dd(10)_{x[HT\ Ref]}$ was measured to be 59.5% which indicated that the mean incident electron energy of our HT is 5.63 MeV. From Eq. (3.5) and our measured value for $\%dd(10)_{x[HT\ Ref]}$, $\%dd(10)_{x\ [HT\ TG\text{-}51]}$ becomes 62.8% which yields a value for k_Q of 0.9973 (figure. 3-2). This value of k_Q is 0.1% lower than that calculated if the measured $\%dd(10)_{x[HT\ Ref]}$ was used instead of $\%dd(10)_{x\ [HT\ TG\text{-}51]}$. Throughout the range of mean incident electron energies for which calculations were done, the corrections increase from only 0.06% to 0.16%. This is because k_Q versus $\%dd(10)_x$ varies slowly in this energy region.

This conversion of the $\%dd(10)_{x[HT\ Ref]}$ values is expected to hold roughly for other chambers as the water-to-air spr is a good indicator of the air-to-C552 spr, [6,9,27] the ratio of mean mass energy absorption coefficients varies only slightly through the energy range studied and α is material insensitive. It should be noted that the statement $P_{repl[HT]} = P_{repl[Varian\ 6\ MV]}$ becomes less true for larger diameter chambers with the maximum error being approximately 0.05%. In addition, our values for the C552-to-air spr can differ from those used in TG-51 up to 0.1% as the value of $\%dd(10)_x$ decreases from 66.6%. Our values, however, agree with more recent calculations.[26,27] Furthermore, throughout the energy range studied, the central electrode correction factor for a 1 mm aluminum electrode would vary by 0.03%.[4] Thus, errors on the order of 0.1% would be expected as the value of $\%dd(10)_x$ decreases from 66.6%. The

larger chamber may also result in increased error due to volume averaging in measuring $\%dd(10)_x$ because of the non-uniform field of the HT unit.

References

[1]T. R. Mackie, T. Holmes, S. Swerdloff et al., "Tomotherapy: a new concept for delivery of dynamic conformal radiotherapy," Med. Phys. **20,** 1709-1719 (1993)

[2] P. R. Almond, P. J. Biggs, B. M. Coursey, W. F. Hanson, M. S. Huq, R. Nath, and D. W. O. Rogers, ''AAPM's TG–51 protocol for clinical reference dosimetry of high-energy photon and electron beams,'' Med. Phys. **26,** 1847-1870 (1999)

[3] R.Jeraj, T.R. Mackie, J. Balog, G, Olivera, D, Pearson. J Kapatoes, K. Ruchala, P Reckwerdt,. "Radiation charachteristics of helical tomotherapy," Med. Phys. **31**, 396-404 (2004)

[4] D.W.O. Rogers, "Fundamentals of dosimetry based on absorbed dose standards," in *Teletherapy: Present and Future*, edited by T.R.Mackie and J.R. Palta. AAPM Advanced Medical Publishing, Madison, 319-356 (1996)

[5] D.W.O. Rogers and C. L. Yang, ''Corrected relationship between $\%dd(10)_x$ and stopping-power ratios,'' Med. Phys. **26**, 538-540 (1999)

[6] P. Andreo, A.E Nahum and A. Brahme, "Chamber-dependent wall correction factors in dosimetry," Phys. Med. Biol. **31**, 1189-1199 (1986)

[7] AAPM TG–21, ''A protocol for the determination of absorbed dose from high-energy photon and electron beams,'' Med. Phys. **10**, 741-771 (1983)

[8] G. D. Lempert, R. Nath, and R. J. Schulz, ''Fraction of ionization from electrons arising in the wall of an ionization chamber,'' Med. Phys. **10**, 1-3 (1983)

[9] IAEA, "Absorbed Dose Determination in Photon and Electron Beams; An International Code of Practice," Technical Report Series Vol. 277, IAEA, Vienna, (1987)

[10] D. W. O. Rogers, B. A. Faddegon, G. X. Ding, Ma C.M. We J, Mackie T.R., "BEAM: a Monte Carlo code to simulate radiotherapy treatment units," Med. Phys. **22**, 503-524 (1995)

[11] D. W. O. Rogers, C.-M. Ma. B. Walters, G.X. Ding, D. Sheikh-Bagheri and G. Zhang, ''BEAMnrc Users Manual,'' Technical Report No. PIRS-509(a), National Research Council of Canada, Ottawa, Canada (2003)

[12] K.A. Johansson, L. Lindborg Mattson, and H Svensson, "Absorbed-dose determination with ionization chambers in electron and photon beams having energies between 1 and 50 MeV," in *Proceedings of the IAEA Symposium on National and International Standardization of Radiation Dosimetry.* IAEA, Vienna, **2**, 243-270 (1978)

[13] H. Buchard and J.P Seuntjens " Ionization chamber-based reference dosimetry of intensity modulated radiation beams," Med. Phys. **31**, 2454-2465 (2004)

[14] D. Sheikh-Bagheri and D. W. O. Rogers, "Sensitivity of megavoltage photon beam Monte Carlo simulations to electron beam and other parameters," Med. Phys. **29**, 379-390 (2002)

[15] P. Munro, J. A. Rawlinson, and A. Fenster, "Therapy imaging: source sizes of radiotherapy beams," Med. Phys. **15**, 517-524 (1988)

[16] Wendell. R. Lutz, Nasser. Maleki, and Bengt E. Bjarngard, "Evaluation of a beam-spot camera for megavoltage x rays," Med. Phys. **15**, 614-617 (1988)

[17] D. A. Jaffray, J. J. Battista, A. Fenster *et al.*, "X-ray sources of medical linear accelerators: focal and extra-focal radiation," Med. Phys. **20**, 1417-1427 (1993)

[18] D. Shiekh-Bagheri, ''Monte Carlo study of photon beams from medical linear accelerators: optimization, benchmark and spectra ,'' Ph.D. Thesis , University of Carleton, (1999)

[19] D. W. O. Rogers, G. M. Ewart, A. F. Bielajew J. Van Dyk, "Calculation of Electron Contamination in a Co-60 Therapy Beam," in *Proceedings of the IAEA Symposium on Dosimetry in Radiotherapy.* IAEA, Vienna, 303-312 (1988)

[20] B. R. B. Walters and D. W. O. Rogers,''DOSXYZnrc Users Manual,'' Technical Report No. PIRS-792, National Research Council of Canada, Ottawa, Canada (2002)

[21] D. W. O. Rogers, I. Kawrakow, J. P. Seuntjens, and B. R. B. Walters, ''NRC User Codes for EGSnrc,'' Technical Report No. PIRS-702, National Research Council of Canada, Ottawa, Canada (2000)

[22] A. Booth and D. W. O. Rogers, ''Effect on Phantom Size, Radial Position, and Depth on Monte Carlo Calculated Stopping Power Ratios ,'' Technical Report No. PIRS-507, National Research Council of Canada, Ottawa, Canada (1995)

[23] ICRU, " Stopping powers for electrons and positrons," ICRU Report 37, ICRU, Washington D.C. (1984)

[24] J. H. Hubbell and S. M. Seltzer, ''Tables of x-ray mass attenuation coefficients and mass energy-absorption coefficients 1 keV to 20 MeV for elements Z=1 to 92 and 48 additional substances of dosimetric interest,'' Technical Report No. NISTIR 5632, NIST, Gaithersburg, MD 20899,(1995)

[25] IAEA, "Absorbed Dose Determination in External Beam Radiotherapy: An International Code of Practice for Dosimetry Based on Standards of Absorbed Dose to Water," Technical Report Series, Vol. 398. IAEA, Vienna, (2001)

[26] E. Mainegra-Hing, I. Kawrakow, and D. W. O. Rogers, ''Calculations for plane-parallel ion chambers in ^{60}Co beams using the EGSnrc Monte Carlo code,'' Med. Phys. 30, 179-189 (2003)

[27] P. Andreo, "Improved calculations of stopping-power ratios and their correlation with the quality of therapeutic photon beams," in *Proceedings of the IAEA Symposium on Measurement Assurance in Dosimetry.* IAEA, Vienna, 335-359 (1993)

Chapter 4: Patient Specific Delivery Verification for 10 HT Treatment Plans

4.1 Introduction

HT is a novel modality for delivering IMRT.[1] HT is capable of delivering enhanced conformal dose distributions,[2] in part because this system makes use of 51 beam projection angles as compared with the 7-15 gantry angles used in conventional IMRT. A verification process to validate the accuracy of these highly complex plans must, however, be developed to ensure confidence in treatment delivery within the clinic. The basic steps for treatment delivery verification are as follows:

1) Recalculate the planned dose distribution(s) on a known and measurable phantom geometry.

2) Measure the planned dose distribution(s) using the phantom geometry.

3) Register and compare the measured and recalculated dose distribution(s).

The acceptable differences between measured and calculated dose distributions should be quantified based upon the treatment site and delivery technique. The radiotherapy community needs to establish clinically relevant acceptability criteria. The work presented here is a possible set of criteria for HT.

One metric that describes how well a measured dose distribution corresponds to a calculated dose distribution is the gamma function (the calculation for gamma is described in section 4.5.3 of this chapter).[3] The literature has previously recommended a number of different criteria for the calculation of gamma. The international commission on radiation units and measurement (ICRU) 42 report recommended a

distance to agreement (DTA) goal of 2 mm and a percent dose difference goal of 2 % as acceptance criteria.[4] These criteria require that once a measured and calculated data set are registered, a pixel within the reference image must correspond to a pixel in the comparison image within 2 % of the dose and 2 mm when added in quadrature. Van Dyk recommended the criteria of 4 mm and 3%,[5] and most recently, Winkler et al. recommended 3 mm and 5 %.[6] Van Dyk has further recommended that 67% of the dose elements (dose pixels) within the plan have a gamma value less than or equal to 1.[7]

In this chapter, we evaluated the agreement between the HT planned and delivered dose distributions using these three sets of criteria. The gamma function was calculated and tabulated for dose points in the calculated dose distribution with dose values above 50% of the maximum calculated dose in the plane examined (i.e the center horizontal plane of the phantom (figure. 4-1)) The reason for choosing >50% dose region for analysis is that 50% of the maximum dose for a single field defines the "high dose" region, and thus was used as a reasonable inclusion criterion for points of interest. The analysis was performed for 10 treatment plan data sets, calculated with the gammas defined from the following criteria: 2 mm & 2 %; 4 mm & 3 %; and 3 mm & 5 % according to the acceptance criteria appearing in the literature.[4-6] In addition, at least two point dose measurements were made for each plan. One point was located in a region of high dose, low dose gradient. A second point was in a region of low dose, low dose gradient. When necessary and feasible, additional points were measured in

the positions of critical structures. From these measurements, a set of standard acceptance criteria for average treatment plan verifications was developed.

4.2 Materials

4.2.1 Phantom

Film and point dose measurements for the HT system were made in a specially designed cylindrical solid water phantom [Standard Imaging, Middleton, WI] capable of accommodating ionization chambers (see figure. 4-1), and which is supplied with the HT unit. The phantom is a cylindrical phantom with a 15 cm radius and a length of 18 cm which is cut into two semi-cylindrical halves such that a sheet of film can lie along the central axis of the phantom. The phantom has a series of holes drilled into it, to allow for the insertion of an Exradin A1SL ion chamber [Standard Imaging, Middleton, WI] (A1SL) for point dose measurements to be made at the locations of the holes. The holes are filled with solid water plugs when the chamber is not used at that location. The phantom is widely known simply as the "Cheese Phantom".

4.2.2 Ion Chamber

All point dose measurements in this study were made using an A1SL ion chamber. The A1SL has a small volume (0.056 cm^3) which makes it a good candidate for point dose measurements. The ion chamber wall of the A1SL is 1.1 mm thick and both the ion chamber wall and the central electrode are made of C552 air equivalent plastic. The absorbed dose to water calibration coefficient for a ^{60}Co beam ($N_{D,w}^{^{60}Co}$) for the A1SL and electrometer was determined at a national standards lab (National Research

Council of Canada, NRCC). The beam quality conversion factor for the A1SL was determined according to work described in the preceeding chapter.[8]

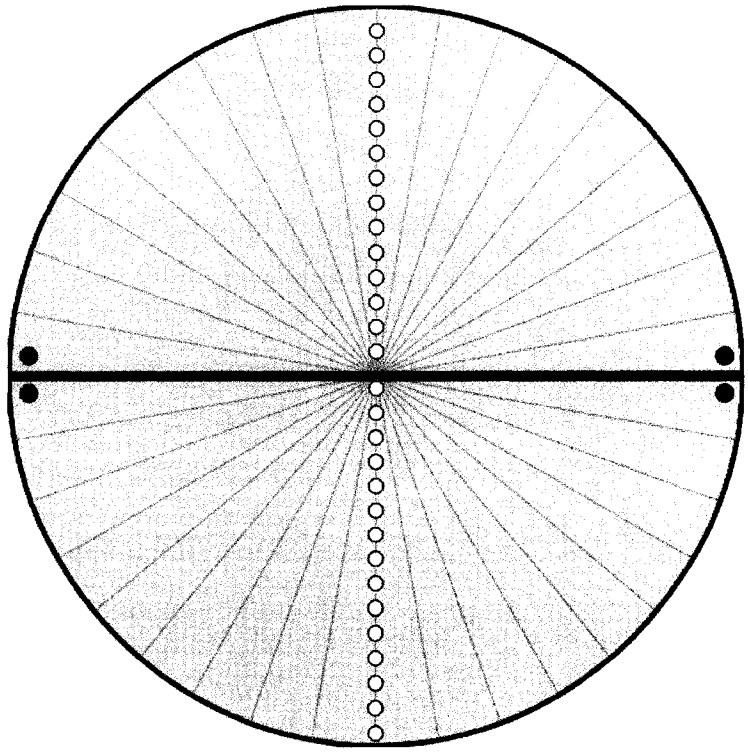

Figure. 4-1 A diagram of the cheese phantom. The white dots correspond to machined holes to accommodate the A1SL ion chamber. The black line cutting the cheese phantom in half is where the EDR2 film is inserted.

4.2.3 Film

All film measurements were made using Kodak EDR2 film.[9-11] The error in film dosimetry has been well studied in the literature and a brief overview of possible sources of error is listed below. Possible sources of error that are specific to the HT system and have not been previously discussed in the literature are investigated in section 4.3.2.

4.2.4 Sources of Error in Film Dosimetry

4.2.4.1 Film Orientation

EDR2 film, when oriented perpendicular to the axis of the beam was found to vary by less than 2% as compared to ion chamber measurements for linac generated photon beams when field sizes were less than 15 X 15 cm^2 and the depth of measurement was 15 cm or less.[10] Recent work using possible HT beam dimensions (5 cm X 2.5 cm) further suggests only very small errors.[11] When film is oriented parallel to the beam, the maximum deviation in the %dd measurement (beyond the depth of maximum dose and for a FS of 10 X 10 cm^2) as compared to ion chamber measurements was also found to be less than 2%.[6] It was suggested that this deviation can be attributed to air gaps between the film and the solid water.[6] Winkler recommends punching holes into the film packaging in order to allow for the escape of the air within the package. Air gaps are not expected to be a problem in the analysis done in this chapter as the film used in the study has been vacuum packed.

4.2.4.2 Time Delay between Film Irradiation and Processing

Recently work by Childress et al. has found that the time delay between film irradiation and processing can affect an increase in the optical density of film by 4-6%.[10] By using a delay of at least one hour, this variation is reduced to about 1%. Childress et al. has subsequently suggested a minimum time delay of one hour between film irradiation and processing.

4.2.4.3 Scanner Nonlinearity

Work done by Childress et al. has suggested that VIDAR scanners are non-uniform. A variation in OD of up to 0.2 between the center and the film edges for both uniform and OD wedges was found.[12] This effect has been attributed to photon scatter from the scanning light.[13] This effect was recently investigated by Hudson from our laboratory who found this effect to be negligible for the specific VIDAR scanner used in the following chapter.[14] These differences may be due to differences in scanner calibration.

4.3 Methods

Details of the 10 treatment plans which were verified in this work are listed in table. 4-1. The 4 treatment sites listed in the table are glioblastoma multiforme (GBM), head and neck (H&N), prostate (P) and palliative bone metastases (PBM) which occurred in no specific location. The two types of treatments listed are single dose prescription (SDP), which refers to plans with a single PTV, and simultaneous integrated boost (SIB) which contains two PTVs with different dose prescriptions. Other information listed includes the prescription dose, number of fractions, the short axis field width, pitch (pitch = table increment per rotation / jaw width), modulation factor, rotation period, number of point dose measured sensitive structures within each plan and the volume of each PTV. The modulation factor is defined as the maximum leaf open time of any leaf divided by the average nonzero leaf open time and is a measure of the range of beam intensities within a single projection. The general protocol for the delivery qualitly assurance (DQA) process employed in this study is

shown in figure. 4-2. For each plan a single dose plane was measured with EDR2 film. In addition to the film measurements between 2 and 4 point dose measurements were made per treatment plan (1 high dose/low dose gradient, 1 low dose/low dose gradient and up to 2 measurement points corresponding to critical structures) using an A1SL ion chamber. The analysis of all film and forward dose calculation data was done using a commercial math package [MATLAB, The Math Works Inc. Natick, Ma]. The primary reason for using this in-house developed software instead of that provided by TomoTherapy Inc. is that software provide by TomoTherapy Inc. does not allow one to constrain the gamma calculations or tabulations to specific regions.

Table. 4-1 Plan information for the 10 treatment plans. The 4 different treatments listed are glioblastoma multiforme (GBM), head and neck (H&N), Prostate (P) and palliative bone metastases (PBM). The 2 types of treatment listed are single dose prescription (SDP) which refers to 1 PTV and simultaneous integrated boost (SIB) which refers to two separate dose level PTVs.

Plan #	1	2	3	4	5	6	7	8	9	10
Treatment Sites	GBM	PBM	GBM	H&N	P	PBM	PBM	PBM	PBM	P
Type	SDP	SDP	SDP	SIB	SIB	SDP	SDP	SDP	SDP	SIB
Prescription Dose (Gy)	54.4	11	54.4	60.0 54.0	72 54	8	8	25	11	68 45
Fractions	20	1	20	30	30	1	1	10	1	25
Field Width (cm)	2.5	5	2.5	2.5	2.5	5	5	2.5	5	2.5
Pitch	0.30	0.20	0.25	0.43	0.43	0.22	0.22	0.43	0.22	0.40
Modulation Factor	2.40	1.40	2.10	1.80	1.80	1.20	1.25	1.40	1.10	1.80
Rotation Period (sec)	25	42	18	15	16	28	23	22	39	19
# Measured Critical Structures	2	0	2	1	0	0	0	0	0	1
Volume of PTV (cm^3)	165	162	318	406 499	112 143	170	117	1473	678	197 695

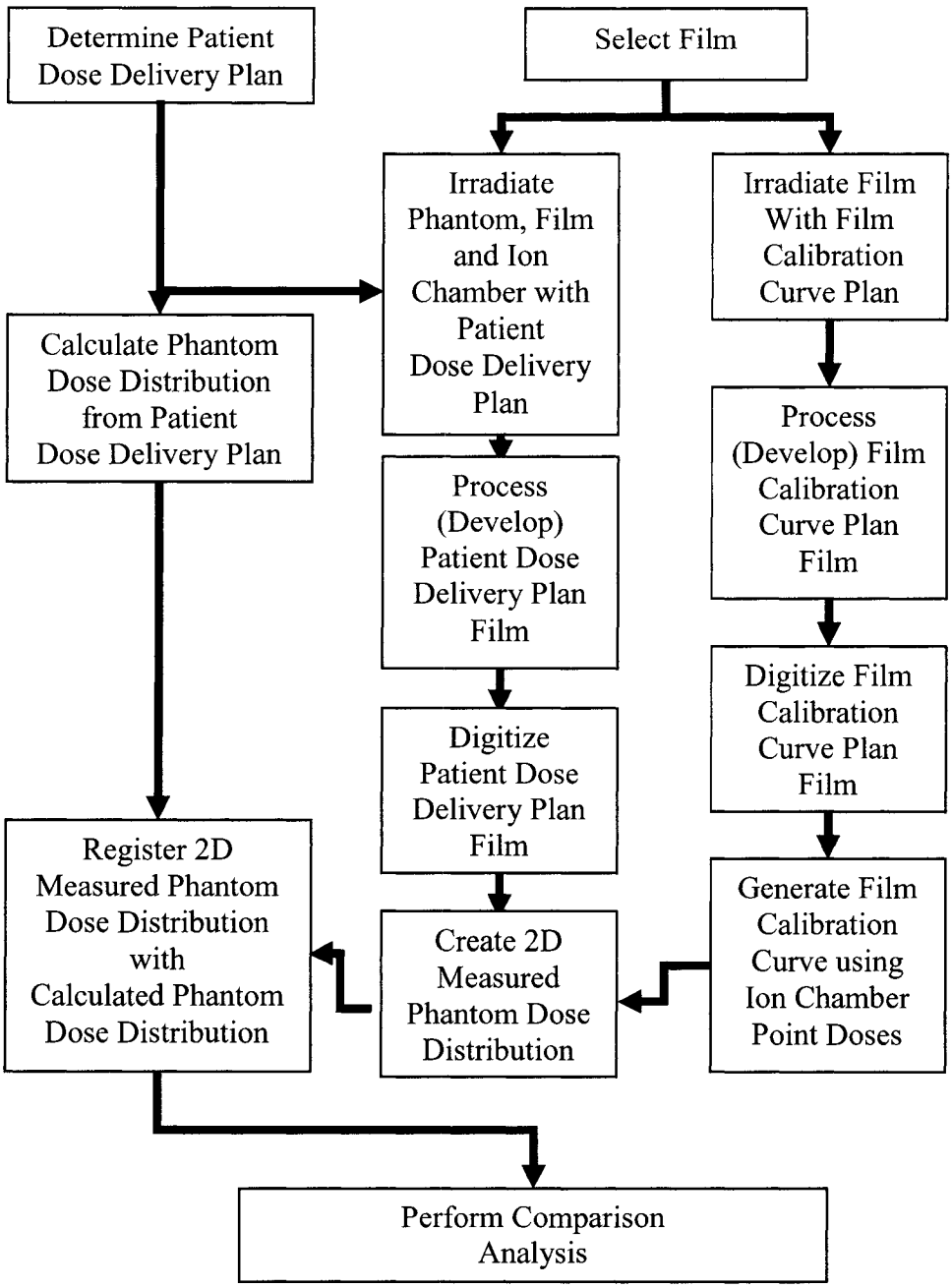

Figure. 4-2 A schematic diagram of the protocol required to perform a patient delivery verification using film.

4.3.1 Forward calculation of the patient treatment plan in the cheese phantom

For each treatment plan, a DQA plan was generated. This involves the forward dose calculation of the patient treatment plan on a DQA phantom, in our case a CT data set of the cheese phantom (figure. 4-3). In a forward calculation the dose is computed from a previously known photon fluence. Where necessary, (i.e single fraction deliveries (plans 2,6,7 & 9)) the DQA plan was scaled such that the delivered dose ranged between 1 - 4.0 Gy to ensure that the dose delivered to the film fell within the linear portion of the film calibration curve.[11] In general, the use of a DQA scaling factor may affect the agreement between measured and calculated dose distributions. For example, if all leaves are opened for 20 msec (an atypically low value) and these openings are scaled by 50% then none of the leaves will be opened because of the 18 msec minimum leaf opening time. This effect is not accounted for in the DQA process. In the 4 plans that we scaled, we investigated this effect by determining the number of leaf openings that would not be delivered when scaled by their appropriate values (0.50, 0.50, 0.35, and 0.3). The largest reduction in the total leaf open time was 0.14% for the plan with both the smallest scaling factor (0.30) and the largest modulation factor (1.4). Thus, we can assume that any errors introduced by the use of a DQA scaling factor for the 4 plans we verified will be negligible. Nevertheless, one should bear in mind that very short duration segments may be dropped, and so a DQA scaling factor should be used with some caution.

There are three requirements for the placement of the phantom with respect to the delivered dose distribution:

(1) The ion chamber point dose measurement within the phantom occurs in a low dose gradient region to minimize the measurement's sensitivity to position and to limit volume averaging within the chamber volume.

(2) Significant portions of the high dose region must intersect the plane in which the film is to be positioned.

(3) The ion chamber is more than 1 cm from the film to minimize the effect of the ion chamber on the film measurement.

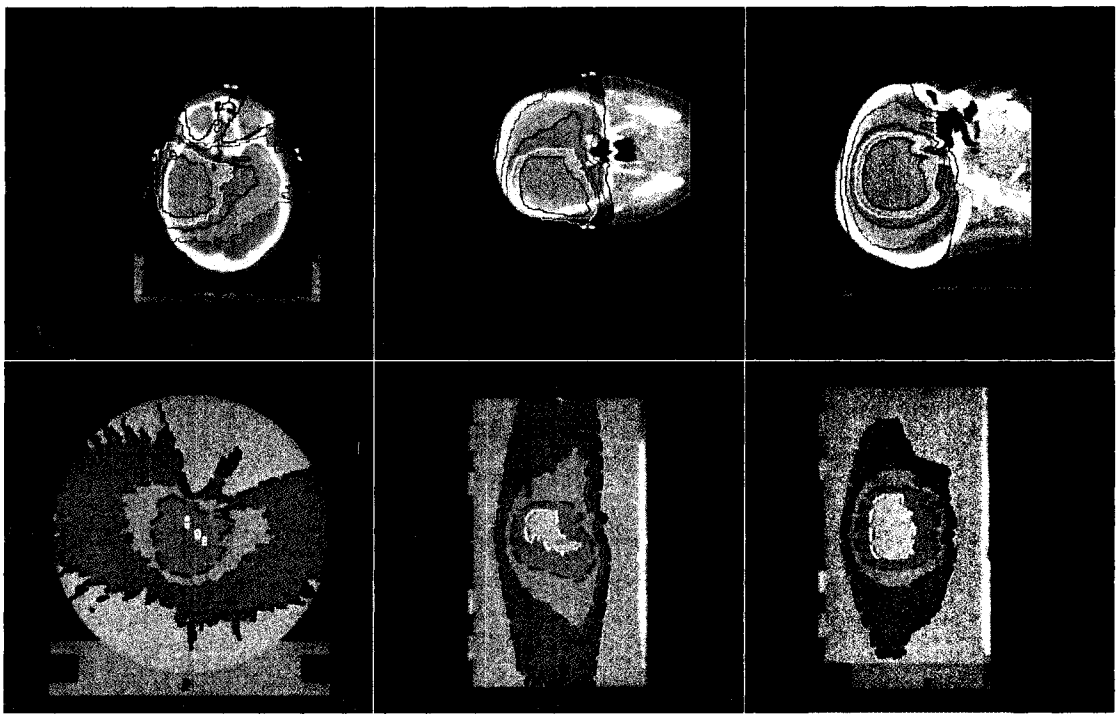

Figure. 4-3 Dose maps in the patient and the cheese phantom. The top three frames show transverse, coronal and sagittal views of a patient treatment plan. The bottom three frames show transverse, coronal and sagittal views of the same plan forward calculated onto the CT data of the cheese phantom.

4.3.2 Calibration of EDR2 film

A non-rotational dose plan termed "the film calibration plan" was created for calibration of the EDR2 films by modulating the multi-leaf collimator within a 5 x 40 cm^2 field to create a film calibration curve of 13 different dose regions for converting the measured optical density to dose (Figure. 4-4).[11] The dose in each region was measured at 1.5 cm depth (according to Eqn. A1) in a 15 x 55 x 5.5 cm^3 solid water phantom using the A1SL ion chamber to determine the ratio of the dose in each region to the central high dose region. The dose to the central region was then measured each day that a treatment or treatment verification was to occur, throughout the duration of this study. This amounted to 29 separate measurements with all measurements having occured on different days. Figure. 4-5 illustrates the variation in the ion chamber measured dose in the central region of the film calibration plan throughout this study. The average mean center region dose value of 4.51 ± 0.03 Gy acquired over these 29 measurements was scaled by the previously acquired dose ratios to determine the dose for all 13 regions. These doses were used in the determination of all the calibration curves used in this study. To assure ourselves that the dose ratios (i.e ratio of each dose region to that of the highest dose region) of the 13 regions had not changed during the study, the 11 high dose regions used in determination of the calibration curve were re-measured and the ratios re-determined at the end of the study. The mean change in the ratios between the two measurements (before and after the study) was found to be only 0.001±0.002 as shown in figure. 4-6. If two treatment verifications were performed on the same day a single calibration film was used for both treatment verifications. To determine the optical densities required for each film calibration

curve, a film was placed at 1.5 cm depth in a 6.5 x 55 x 5 cm^3 solid water and irradiated using the aforementioned film calibration plan. After irradiation, the film was left to stabilize for 2 to 3 hours before processing.[10] The stabilized film was digitized using a vidar film scanner. The mean vidar scanner value was then determined from a 4.68 x 4.68 mm^2 (13 pixels x 13 pixels) region of interest (ROI) in each of the 13 dose regions using matlab. These mean vidar scanner values were ploted vs their corresponding dose level to create the film calibration curve (figure. 4-7) again using matlab.

Figure. 4-4 An exposed film with the 13 dose levels used to calibrate the treatment film. The film was irradiated at a depth of 1.5 cm in solid water.

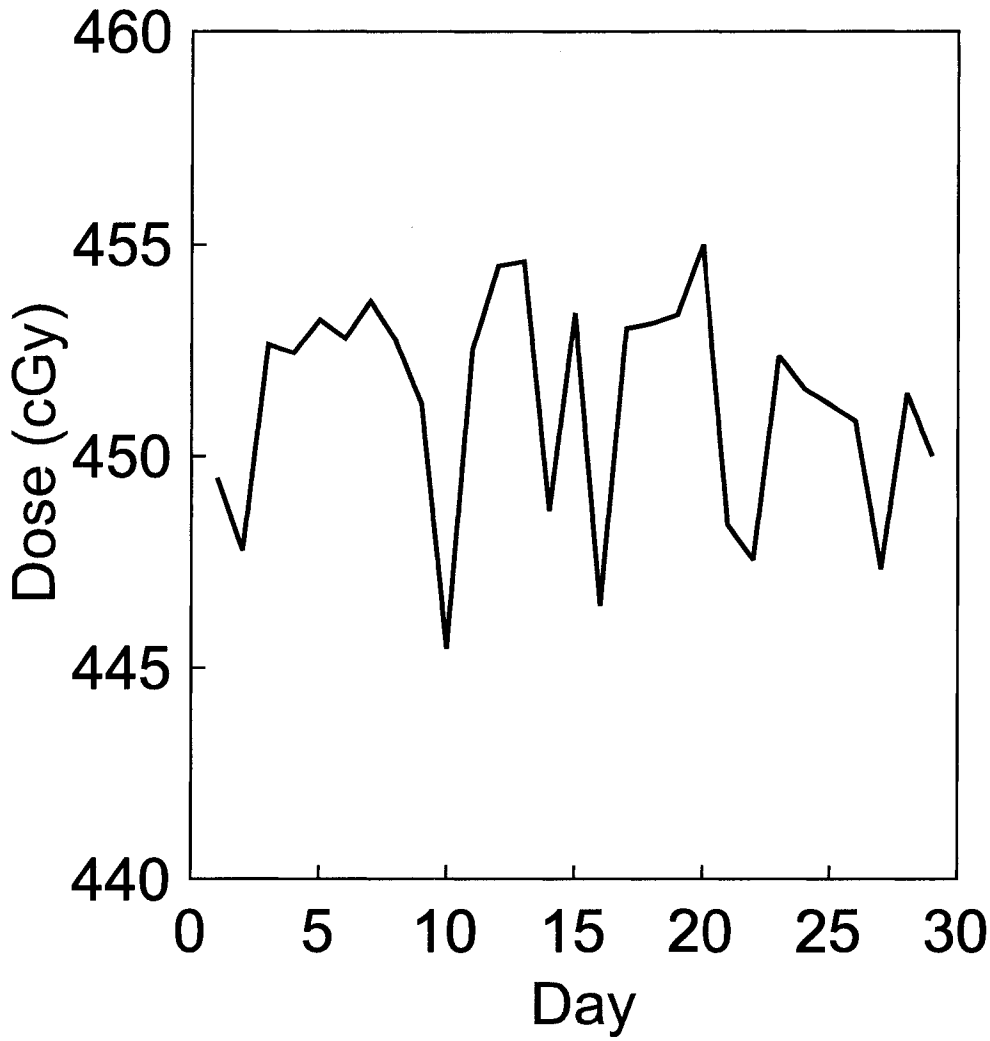

Figure. 4-5 The dose to the central dose region of the film calibration curve plan for 29 days as measured with an A1SL ion chamber. This dose was measured on any day that a delivery verification or patient delivery was to occur.

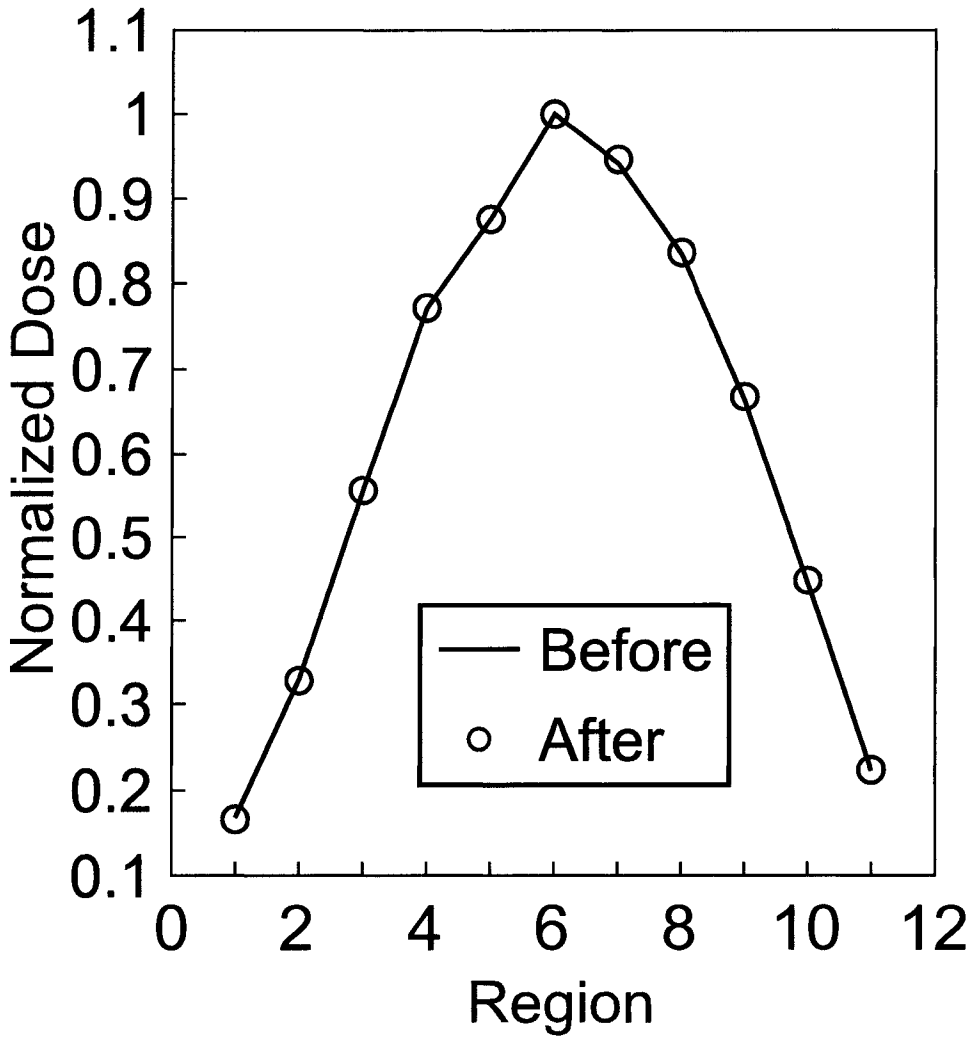

Figure. 4-6 Normalized dose values measured with an A1SL ion chamber for the 11 central dose (high dose) regions of the film calibration curve plan.

The effect of measurement depth on EDR2 film has been previously investigated in conventional linear accelerator photon beams.[15] The softer unfiltered beam of the HT unit[8] may however result in greater EDR2 film depth dependencies than would occur in a conventional linear accelerator beam. The depth dependence of the EDR2 film in the HT beam was investigated by creating two film calibration curves. The first curve was determined at 1.5 cm depth while the second curve was determined at 10 cm depth in a solid water phantom (figure. 4-7). Both were measured at a distance of 85 cm from the source. The doses at a depth of 10 cm for the 13 positions of the calibration pattern were measured with an A1SL ion chamber. The

agreement between the two curves was found to be excellent with a mean discrepancy of 0.2%. Leakage through the MLC on the calibration film is expected to affect the measurement by only 0.15%.[11] The film doses analyzed in this study ranged from 0.55 to 3.87 Gy which fall in the linear range of the film calibration curve as shown in figure. 4-7. Below this 0.55 Gy dose level all comparisons between measured and calculated doses were made with ion chamber point dose measurements.

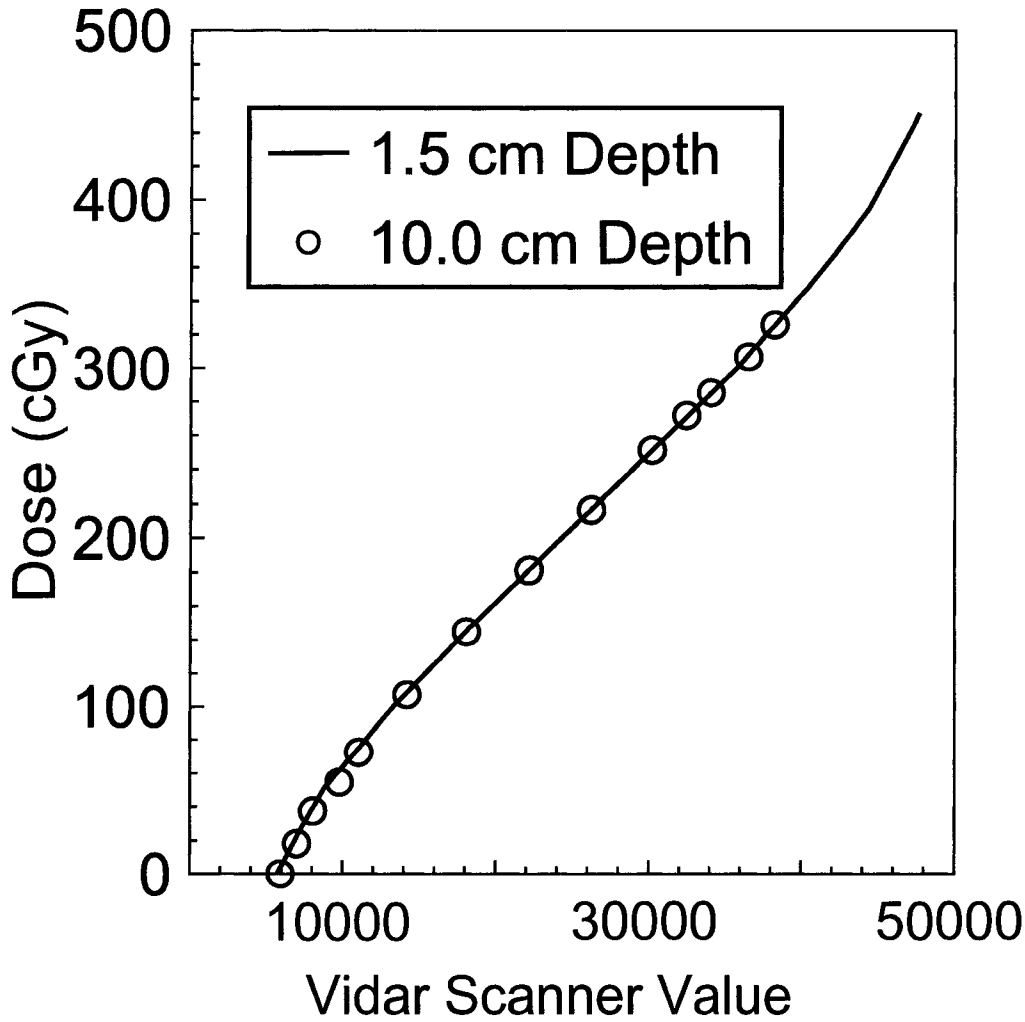

Figure. 4-7 Film calibration curves determined at 1.5 cm and 10.0 cm depths show excellent agreement.

4.3.3 Calibration of the Isocenter Lasers

The HT virtual isocenter is a point in space located 70 cm along the couch travel axis (the Y axis in the IEC 't' coordinate system)[17] from the mega voltage CT (MVCT) image and treatment isocenters. The virtual isocenter is used as a coordinate system reference point for the dose calculations and is matched to a set of stationary green lasers mounted above the couch and behind the bore. The following steps were taken to ensure that the physical position of the measured dose distribution corresponds to that of the virtual calculated dose distribution:

(1) A point object was positioned at the intersection of the green lasers. The object was then imaged with the HT onboard MVCT system. This determined the correct X and Z positions for the green lasers (figure. 4-8).

(2) For the Y and Z direction, the center of the radiation field (90° in figure. 4-8) relative to the green laser center was determined by marking the laser position onto a film which was then sandwiched between two 15 x 40 x 5 cm^3 blocks of solid water and placed perpendicular to a 5 x 40 cm^2 beam. The film/couch was moved into the bore to the radiation-isocenter of the HT system and irradiated. The Y-Z offset between radiation center and green lasers center was determined.[17] The same measurements were made with the gantry positioned at 0° as shown in figure. 4-8 to determine the corrections in the X-Y direction. These measurements verified that the image and treatment isocenters were coincident to within 2.0 mm; we believe this uncertainty results from errors in placing and marking the film. The calibration of the lasers was performed with the cheese phantom on the table, at a table height positioning the vertical centre of the cheese phantom at level of the coronal lasers. It

should be noted that couch flex can introduce positional errors which are dependent on the weight applied to the couch.

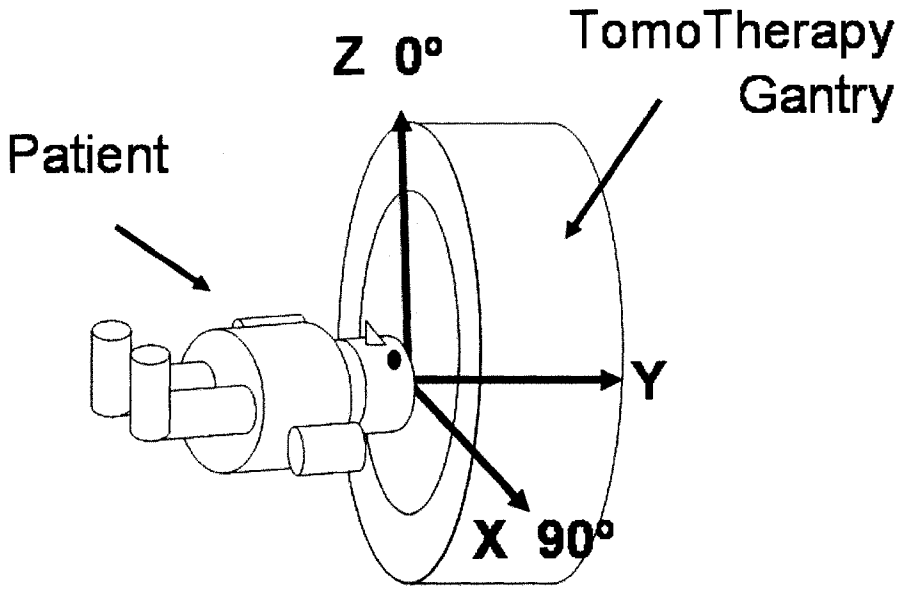

Figure. 4-8 Illustration of the coordinate system of the HT system as well as the 0° and 90° gantry positions.

4.3.4 Delivery of the Treatment Plan

The cheese phantom was aligned using the DQA module of the planning station software as described in 4.3.1 using the patient positioning (red) lasers, and scanned with the HT on-board (MVCT) scanner. To ensure correct position of the cheese phantom within the HT bore the resultant image was fused with the corresponding planning image obtained with conventional CT, and the X-Y-Z translation errors were determined. The cheese phantom was then retracted and the

position of the cheese phantom was corrected. The Z and Y translation errors were corrected automatically by applying the translation errors to the bed. The X translation error was corrected manually using a pair of adjustment screws on the bed. There was a slight discrepancy in the forward tilt of the MVCT image as compared to the CT planning phantom image (approximately 2 mm over 180 mm) which was not accounted for in our positional correction. This was most likely due to differences between the couch flex of the CT unit as compared to the HT unit. The EDR2 film was then inserted inside the cheese phantom along the XY plane of the bore. The HT XY virtual isocenter was marked on the film using the virtual isocenter (green) lasers. The A1SL was then placed in the phantom and the HT radiation plan was delivered. After irradiation, the film was left to stabilize for the same period of time as its corresponding calibration film prior to processing.[10] The HT radiation plan was then re-delivered, once for each separate point dose measurement. In two cases, the treatment plan had to be recalculated at a different location within the cheese phantom to allow the critical structure point dose measurements to be made.

4.3.5 Determination and Analysis of the Gamma Values and Point Dose Measurements

The treatment film was digitized at 0.36 X 0.36 mm^2 resolution using a VIDAR VXR film digitizer. The digitized optical density map was then converted to a dose map according to the film calibration curve (as described in 4.2.2) using Matlab. Small rotational corrections (which result from feeding the film into the VIDAR scanner) could then be applied to the measured dose distribution using the marks made

on the film according to the green external lasers. The calculated dose distribution corresponding to the plane of the measured dose distribution was then determined according to the position of the cheese phantom using TomoTherapy Inc. software. The size of voxels used in the dose calculations was 1.875 x 1.875 x 3 $mm.^3$ The calculated dose distribution was then up-sampled using nearest neighbor interpolation such that the dose pixel size of the measured and calculated dose distributions were both 0.36 X 0.36 mm^2. Two data sets were created, the first with the X and Y position of the measured dose distributions registered to the calculated one using the marks made on the film according to the green lasers. This un-normalized and film mark registered data set will be referred to as data set number 1 (DS#1). For data set number 2 (DS#2), the two dose distributions were manually matched using single pixel translations and normalized. The distributions were matched manually by aligning isodose lines and profiles. The dose distributions for DS#2 were normalized to each other by scaling the measured dose distribution such that the mean dose value for all dose pixels greater than 50% of the maximum calculated dose were the same for both dose distributions. For each of these data sets, gamma values were calculated for the region of the calculated dose map where dose pixel values were greater than 50% of the maximum calculated dose according to:

$$\gamma(r_c) = \min\{\Gamma(r_m, r_c)\}\forall\{r_m\} \qquad 4.1$$

where

$$\Gamma(r_m, r_c) = \sqrt{r^2(r_m, r_c)/\Delta d_M^2 + \delta^2(r_m, r_c)/\Delta D_M^2}\ , \qquad 4.2$$

$$r(r_m, r_c) = |r_m - r_c| \qquad 4.3$$

and

$$\delta(r_m, r_c) = \frac{(D(r_m) - D(r_c))}{D_{max\ calculated}} \times 100\% \ . \qquad 4.4$$

r_c is the position of the calculated dose pixel and r_m is the position of the measured dose pixel. $D(r_c)$ is the calculated dose at position r_c and $D(r_m)$ is the measured dose at position r_m. Δd_M is the distance to agreement criteria and ΔD_M is the dose difference criteria. Gamma ($\gamma(r_c)$) was calculated for three sets of Δd_M & ΔD_M criteria, namely 2 mm & 2%, 4 mm & 3% and 3 mm & 5%. $D_{max\ calculated}$ is the maximum calculated dose in the film plane, and acts as the reference point for the percent dose difference portion of the gamma calculation.[14] $\Gamma(r_m, r_c) = 1$ describes the surface of a volume of acceptance for the given criteria of Δd_M and ΔD_M. Any calculated dose pixel where $\gamma \leq 1$ has met the acceptance criteria and a calculated dose pixel where $\gamma > 1$ has failed the acceptance criteria. It should be noted that the gamma calculation used in this chapter is based on the calculated value $\gamma(r_c)$ instead of the gamma calculation based on the measured value $\gamma(r_m)$ as described by Low et al.[2] $\gamma(r_c)$ was chosen instead of $\gamma(r_m)$ because the goal of this exercise is to validate the calculated dose plan and not the measurement. The search radius for the gamma calculation was limited to 1.0 cm,

and no gamma calculations were made within 1.0 cm of the edge of the phantom. All steps required for the registration of the two dose distributions and gamma calculations were made using scripts developed in-house with Matlab. Gamma values were then binned into 8 bins of 0.25 widths and the percentage of dose pixels falling into each of the 8 bins was tabulated using the in-house developed software. The percentage of dose pixels passing and failing each of the three criteria sets for the gamma calculations was also tabulated. For the point dose measurement the percent discrepancy was calculated according to:

$$\%\text{Discrepancy} = \frac{(D_m - D_c)}{D_c} \times 100\% \qquad 4.5$$

where D_m is the measured point dose and D_c is the calculated dose at the same position.

4.4 Results and Discussion

4.4.1 Gamma Values Using Film Marks for Registration without Normalization

The percentage of pixels passing the 3 gamma criteria for all 10 treatment plans are tabulated in table. 4-2. Gamma value maps calculated with the 2 mm & 2%, 4 mm & 3% and 3 mm & 5% criteria are shown for treatment plan 4 (which represents the most typical patient in terms of the percentage of pixels passing the gamma criteria) of DS#1 in figure. 4-9(a), figure. 4-10(a) and figure. 4-11(a) respectively. For this treatment plan, the percentage of dose pixels passing the gamma test (i.e. $\gamma \leq 1$) calculated with the criteria of 2 mm & 2%, 4 mm & 3% and 3 mm & 5% are 66.55%,

94.53% and 95.23% respectively. A histogram of the mean gamma distributions for all treatment plans calculated using the three criteria is shown in figure. 4-12. The mean percentage of dose pixels passing the (DS#1) gamma test for the three criteria of 2 mm & 2%, 4 mm & 3% and 3 mm & 5% were found to be 69.8% ± 17.2%, 92.6% ± 9.0% and 93.4% ± 8.5%.

Table. 4-2 Percentage of pixels passing 3 different gamma criteria for 10 treatment plans.

Film marks for registration without normalization										
Plan #	1	2	3	4	5	6	7	8	9	10
2 mm & 2%	88.83	60.82	70.92	66.55	29.88	88.20	85.16	74.30	68.59	64.31
4 mm & 3%	99.29	94.70	92.12	94.53	68.66	99.87	99.87	90.23	92.23	94.96
3 mm & 5%	99.99	92.73	94.16	95.23	70.72	99.39	99.73	92.02	92.43	96.26
Manual registration and normalization										
Plan #	1	2	3	4	5	6	7	8	9	10
2 mm & 2%	92.80	96.04	93.31	90.60	96.98	94.26	95.40	79.38	84.11	88.76
4 mm & 3%	99.76	99.97	99.97	98.35	100.0	99.74	99.74	95.80	99.13	99.45
3 mm & 5%	100.0	99.96	100.0	98.32	100.0	99.95	99.95	97.65	99.17	99.91

4.4.2 Gamma Values using Manual Registration and Normalization

The mean shifts required for manual registration were -0.1±2.2 mm in the head-to-foot direction and 1.2±1.7 mm in the left-right direction. A possible source of the left-right offset is movement of the phantom when replacing the top half of the cheese phantom after inserting the film. Other possibilities include a misalignment of the green laser with respect to the virtual isocenter or errors generated in marking the laser points on the film. The ratio of mean measured dose to mean calculated dose for dose pixels greater than 50% of the maximum calculated dose was found to be 1.01±0.02. The percentage of pixels passing the 3 gamma criteria for all 10 treatment plans_using manual registration and normalization are tabulated in table. 4-2.

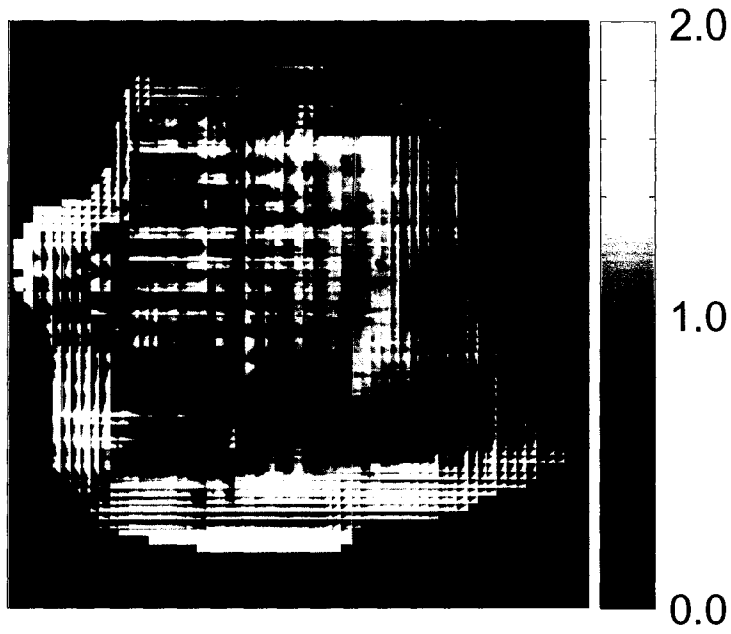

a)

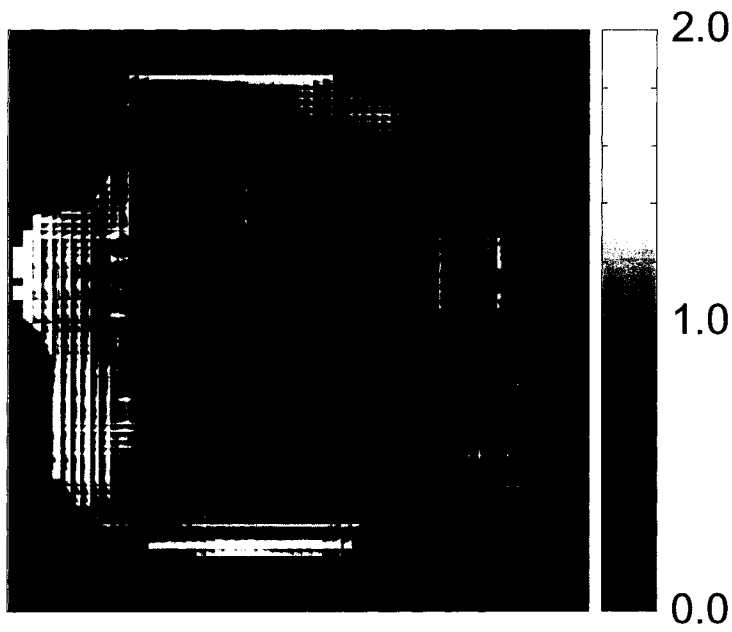

b)

Figure. 4-9 a) is a gamma map calculated using the un-normalized data/film mark registration for the 2 mm & 2% criteria. b) is a gamma map for the normalized/manually registered data set for the 2 mm & 2% criteria. The color bar indicates the color coding for the different gamma levels.

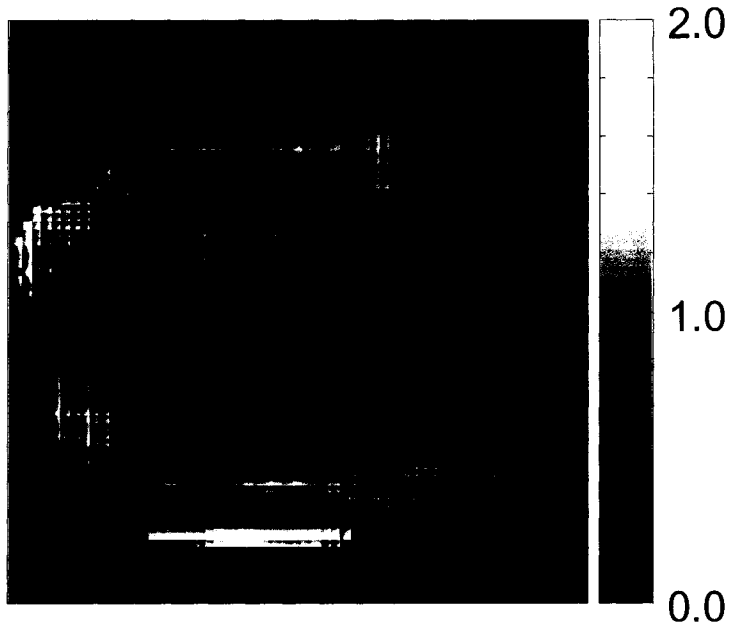

a)

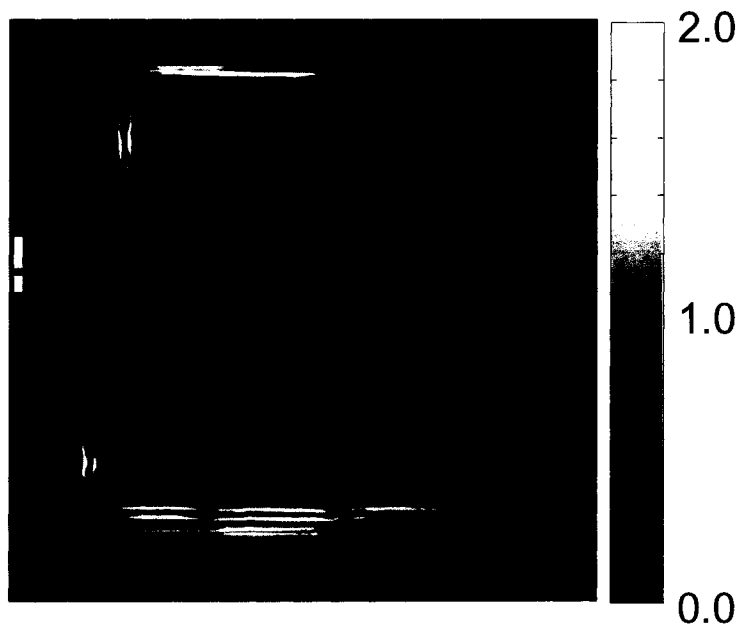

b)

Figure. 4-10 a) is a gamma map calculated using the un-normalized data/film mark registration for the 4 mm & 3% criteria. b) is a gamma map for the normalized/manually registered data set for the 4 mm & 3% criteria. The color bar indicates the color coding for the different gamma levels.

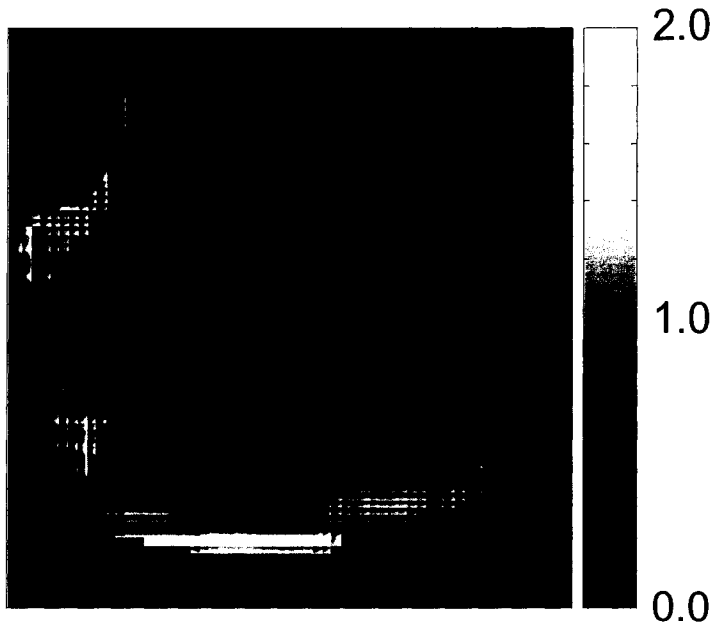

a)

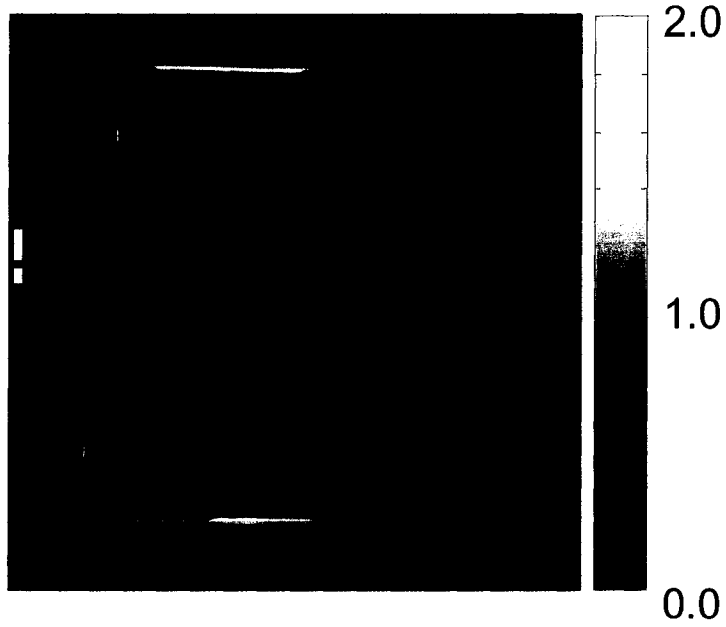

b)

Figure. 4-11 a) is a gamma map calculated using the un-normalized data/film mark registration for the 3 mm & 5% criteria. b) is a gamma map for the normalized/manually registered data set for the 3 mm & 5% criteria. The color bar indicates the color coding for the different gamma levels.

Gamma value maps are shown for the 2mm & 2%, 4 mm & 3% and 3 mm & 5% gamma criteria of treatment plan number 4 of DS#2 in figure. 4-9(b), figure. 4-10(b) and figure. 4-11(b), respectively. It is clear that the number of dose pixels with $\gamma(rc) \leq 1$ is much improved when using manual dose distribution matching and normalization. The mean gamma value histogram is shown in figure. 4-12 for the 2mm & 2% criteria for the DS#2 and more closely approximates the 4 mm & 3% criteria of DS#1. The mean percentage of dose pixels passing the gamma test for the three criteria of 2 mm & 2%, 4 mm & 3% and 3 mm & 5% were found to be 91.8%±5.6%, 99.1%±1.43% and 99.5%± 0.8%. Thus for DS#2, nearly 92% of the dose pixels within the region of interest fall within the strictest gamma criteria of 2 mm & 2%.

4.4.3 Point dose measurements

Point dose measurements for all ten treatment plans are shown in table. 4-3. The mean percent discrepancy for the high dose point dose measurements of the 10 treatment plans was found to be -0.5±1.1%. The mean percent discrepancy for the low dose point dose measurements of the 10 treatment plans was found to be –2.4±3.7%. The mean percent discrepancy for the critical structure point dose measurements of the 10 treatment plans was found to be -1.1±7.3%. The much larger standard deviation for the low dose and critical structure point dose measurements can be attributed to the fact that the majority of these points exist on dose gradients which makes them particularly sensitive to probe positioning and volume averaging effects.

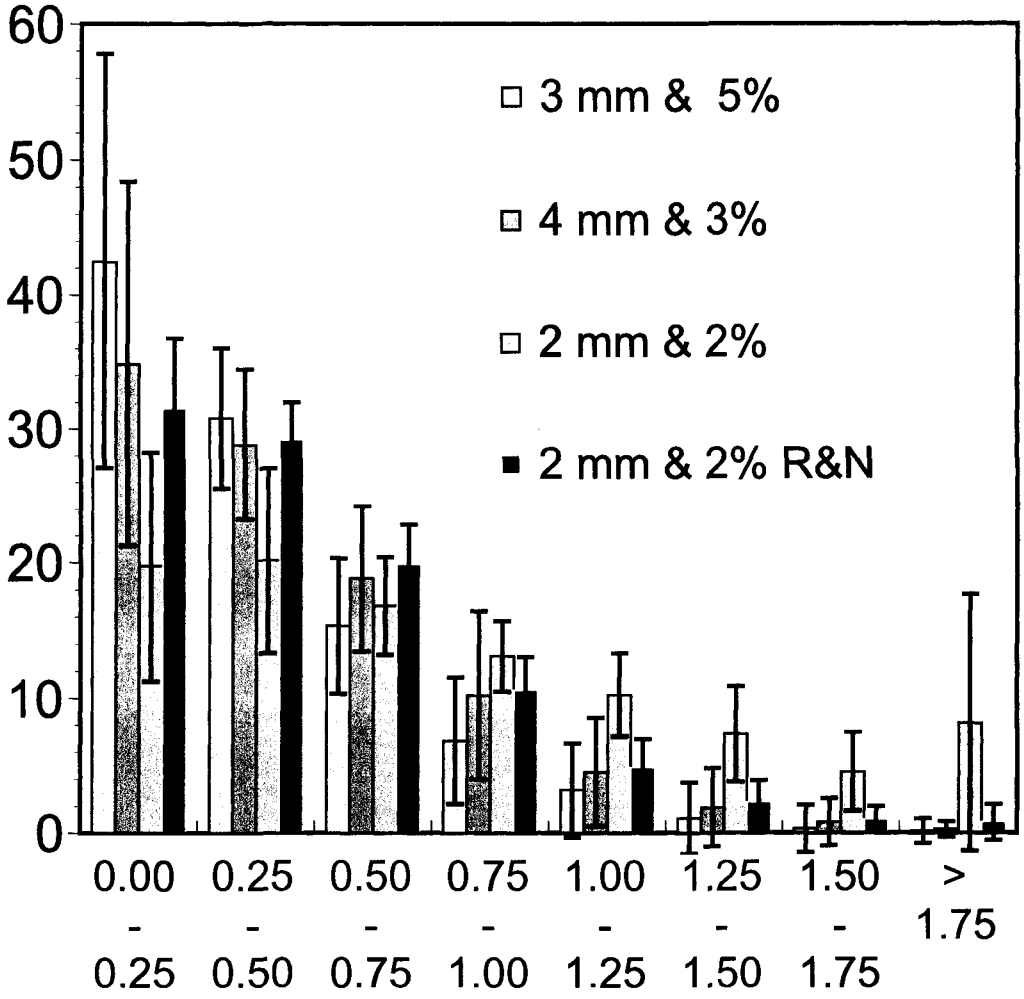

Figure. 4-12 The mean percentage of dose pixels falling into 1 of 8 gamma bins (i.e gamma value ranges). The results are for the 10 delivery verifications. R&N signify the manually registered and normalized data set (DS#2). The error bars represent 1 standard deviation.

Table. 4-3 Calculated and measured point doses for 10 treatment plans.

High Dose Region										
Plan #	1	2	3	4	5	6	7	8	9	10
Calculated Dose(cGy)	201.7	297.1	198.4	138.4	230.5	285.9	318.1	286.5	360.0	259.1
Measured Dose(cGy)	197.4	295.6	199.6	135.7	229.3	286.9	321.7	283.9	354.3	259.7
Percent Diff (%)	-2.1	-0.5	0.6	-2.0	-0.5	0.4	1.1	-0.9	-1.6	0.2
Low Dose Region										
Plan #	1	2	3	4	5	6	7	8	9	10
Calculated Dose(cGy)	40.8	94.1	65.8	57.9	58.8	83.4	94.8	144.4	144.7	75.8
Measured Dose(cGy)	37.4	95.9	62.0	59.0	59.0	82.9	91.6	139.5	144.8	81.3
Percent Diff (%)	-8.4	1.9	-5.7	1.9	0.3	-0.6	-3.1	-3.4	0.0	-7.3
Critical Structures										
Plan #	1	2	3	4	5	6	7	8	9	10
Calculated Dose(cGy)	128.7 137.6	N/A	10.1 137.6	57.9	N/A	N/A	N/A	N/A	N/A	110.4
Measured Dose(cGy)	111.3 141.2	N/A	10.1 144.2	54.4	N/A	N/A	N/A	N/A	N/A	116.4
Percent Diff (%)	-13.5 2.6	N/A	0 4.8	-6.0	N/A	N/A	N/A	N/A	N/A	5.4

4.5 Conclusion

The un-normalized, film mark registered dose maps (DS#1), satisfied the 2 mm & 2% criteria with 69.8±17.2% of the dose pixels passing. However, the agreement was deemed excellent for the 4 mm & 3% and 3 mm & 5% criteria where 92.6±9% and 93.4±8.5% of the dose pixels passed, respectively. When using dose maps which have been normalized and manually matched (DS#2), the agreement was excellent with 91.2±5.6% of the dose pixels agreeing to within 2 mm & 2% and 99.2±1.43%, and 99.5±0.8% agreeing for the 4 mm & 3% and 3 mm & 5% criteria, respectively. Both sets of gammas calculated using the 3 mm & 5% criteria agree within error to the

findings of Childress et al.[18] for their IMRT verifications, even though the methods used to determine the gamma maps are different. No obvious relationship between the planning parameters listed in table. 4-1 and the percentage of passing gamma pixels was found, however a larger sample size may reveal such dependencies.

At our center, we have established 3 tolerances for a successful treatment verification of an average treatment plan. Each tolerance gives criteria for a separate aspect of the treatment plan. The tolerance for the film mark registered and un-normalized dose map is 80% of the dose pixels passing the 3 mm & 5% gamma criteria.[18] This test allows us to identify major differences between calculation and measurement including all sources of error including positioning and the limitations of film as a dosimeter. We feel that the criteria of 3 mm & 5% should encompass all measurement error.[5] We also feel that the positioning error in the delivery verification gives a good indication of the limits of positioning accuracy during the treatment itself, and thus should remain visible in the treatment verification. The tolerance for the manually registered and normalized dose map is 80% of the dose pixels passing the 2 mm & 2% gamma criteria. This test provides information about how accurately the dose plan will be delivered assuming that all error in the first test is due to experimental error and the limitations of film as a dosimeter. The tolerance for the high dose point dose measurement is 2%. This test provides a more robust measure of the absolute dose difference between the calculation and delivered dose. We feel that the combination of these 3 tests provide a good method for identifying errant treatment plans. We have not specified any acceptability criteria for the low dose point

measurement or the critical structure point measurement. We feel that the interpretation of these measurements should be made on a patient-specific basis, perhaps with input from a radiation oncologist. Low dose regions are of particular interest if the potential exists for the patient to be retreated. The calculation of the patient treatment plan on the cheese phantom sometimes makes it difficult to accurately position the phantom for a critical structure measurement, particularly if the structure is small. This difficulty combined with the fact that these regions often contain or lie in close proximity to steep dose gradients suggest that setting a strict criterion for plan rejection could prove to be overly conservative. In some situations (i.e. patient retreats) strict criteria on critical structure low dose regions may be more important than our high dose region criteria.

References

[1] T. R. Mackie, T. Holmes, S. Swerdloff, P. Reckwerdt, J.O Deasy, J.Yang,B Paliwal T Kinsella, "Tomotherapy: a new concept for the delivery of conformal radiotherapy using dynamic collimation," Med. Phys. **20,** 1709-1719, (1993).

[2] M. van Vulpen, C. Field C.P. Raaijmakker, M.B. Parliament, C.H.Terhaard, M. MacKenzie, R. Scrimger, B.G. Fallone "Comparing step-and-shoot IMRT with dynamic helical tomotherapy IMRT plans for head-and-neck cancer" Int J Radiat Oncol Biol Phys **238** 1535-1539, (2005)

[3] D. Low, Harms W, Mutic S, Purdy J, "A technique for the quantitative evaluation of dose distributions," Med. Phys. **25**, 656-661 (1998).

[4] ICRU 42 "Use of Computers in External Beam Radiotherapy Procedures with High-Energy Photons and Electrons" (1987)

[5] J. Van Dyk, R. Barnett, J. E. Cygler, P.C. Shragge. "Commissioning and QA of treatment planning computers," Int. J. Radiat. Oncol. Biol. Phys. **26,** 261-273 (1993).

[6] Winkler P, B. Zurl, H. Guss, P. Kindl G Stuecklschweider. "Performance analysis of a film dosimetric quality assurance procedure for IMRT with regard to the

employment of quantitative evaluation methods," Phys. Med. Biol. **50**, 643-654 (2005).

[7] J. Van Dyk, R.B. Barnett, J.J. Battista, Computerized Radiation Treatment Planning Systems in The Modern *Technology of Radiation Oncology*, edited by J. Van Dyk Medical Physics Publishing, Madison Wisconsin, (1999)

[8] S. D. Thomas, M. Mackenzie, D. W. O. Rogers, B. G. Fallone, " A Monte Carlo derived TG-51 equivalent calibration for helical tomotherapy," Med. Phys. **32** 1346-1353 (2005)

[9] N. L. Childress, I. I. Rosen "Effect of Processing time delay of the dose response of Kodak EDR2 Film," Med. Phys. **31**, 2284-2288 (2004)

[10] X. R. Zhu, S. Yoo, P. A. Jursinic, D. F. Grimm, F. Lopez, J. J. Rownd, and M. T. Gillin, "Characteristics of sensitometric curves of radiographic films," Med. Phys. **30**, 912–919 (2003)

[11] Y, Yan, N Papanikolaou X. Weng, J Penagaricano, V. Ratanatharathorn. "Fast radiographic film calibration for helical tomotherapy intensity modulated radiation therapy dose verification," Med. Phys. **32** 1566-1570 (2005)

[12] N. L. Childress, I. I. Rosen DoseLab 3.04 User Manual. http://doselab.sourceforge.net/manual.html (2003)

[13] N. L. Childress, L. Dong,I. I. Rosen, "Rapid radiographic film calibration for IMRT using automated MLC fields," Med.Phys **29,** 2384-2390 (2002)

[14] A. Hudson, "Dose verification of treatment films using film" M.Sc Thesis, University of Alberta, (2004)

[15] J.Olch "Dosimetric performance of an enhanced dose range radiographic film for intensity-modulated radiation therapy quality assurance", Med.Phys. **32** 2159-2168 (2002)

[16] IEC, "Radiotherapy equipment- Coordinates, movements and scales" IEC 61217, Edition 1.1,IEC, Geneva Switzerland, (2002-03)

[17] J. D. Fenwick, W. A. Tome, H.A. Jaradat, et al. "Quality assurance of a helical tomotherapy machine, " Phys Med. Biol **49** 2933-2953 (2004)

[18] N.L Childress, R.A.White, C. Bolch, et al. "Retrospective analysis of 2D patient specific IMRT verifications," Med. Phys. **32**, 838-850 (2005)

Part 2

Seed Identifcation Required for

Delivery Varification in Brachytherapy.

Chapters 5-6

Chapter 5 Characterization of the Susceptibility Artifact Around a Prostate Brachytherapy Seed in MRI

5.1 Introduction

Brachytherapy with transrectal ultrasonography-guided transperineal implantation of interstitial radioactive seeds has become a common modality for treating localized prostate cancer. The aim is to place an array of seeds in and around the prostate in order to deliver a minimum prescribed dose to the cancerous cells while minimizing side effects to non-cancerous tissue. Post-implant dosimetric evaluation currently relies on X-ray computed tomography (CT). In order to optimize post-implant evaluation, accurate knowledge of seed location and excellent prostate delineation must be simultaneously realized. Although CT gives good localization of the brachytherapy seeds, it is poor at defining the volume of the prostate gland itself.[1,2] As opposed to CT, magnetic resonance imaging (MRI) provides excellent prostate delineation but larger uncertainty as to the precise source location. The artifacts surrounding the brachytherapy seeds are a major cause of uncertainty in seed localization using MRI. In MRI, the brachytherapy seeds are typically viewed as signal voids due to the absence of H^1 within the seeds.[1,2] For a general explanation of the MRI experiment please refer to appendix C. The actual appearance of seeds in MR images is much more complicated, however, due to the local magnetic field distortions caused by the seeds themselves. For most cases, the artifacts created by these distortions are expected to originate via two primary mechanisms. Firstly, the induced field gradients surrounding the seed will warp the planar nature of the slice selection, altering the anticipated image geometry. Secondly, the H^1 within the distorted

magnetic field will be spatially misrepresented in the frequency encoding process due to their altered resonance frequency. This will result in a pattern of signal accumulation and depletion at specific locations surrounding the brachytherapy seed. The nature of this pattern will depend on the direction and magnitude of the read gradient (G_{read}).

In this chapter, we model the local magnetic-field distortions around a particular brachytherapy seed, then use this information to model the slice selection and the frequency encoding of the signal around the seed. The MRI artifacts can then be predicted and simulated. Unlike the case of an MRI image, the exact location of the seed is known *a priori* in the model. Therefore, assuming a good agreement between the model and the actual MRI output, we can use the model to pinpoint the seed location within the artifact pattern present in MR images of brachytherapy seeds.

5.2 Materials and Method

5.2.1 MR imaging

A non-radioactive prostate brachytherapy seed (IMC6711, OncoSeed^{TM}) was obtained and suspended horizontally in a porcine gel (3% wt.). This particular seed is comprised of a 3 mm long and 0.5 mm wide cylindrical silver rod, onto which Iodine-125 is normally adsorbed. Surrounding this rod is a 0.05 mm thick titanium shell with an outer diameter of 0.8 mm (figure. 5-1) and a length of ~3.7 mm. At both ends of the titanium shell is a roughly hemispherical weld. All imaging experiments in this study were performed on a Philips 1.5 T Intera scanner, utilizing a read-only head RF

coil in conjunction with the body coil for transmission. The head coil was chosen as it best matched the size of the phantom. The seed was positioned in the coronal plane with its long axis aligned at 0° (parallel), 90° (perpendicular), and 45° with respect to the axis of the bore.(figure. 5-2) Parameters were chosen to obtain a non-interpolated in-plane resolution of 352 μm (see appendix C) and slice thicknesses of 1 mm. A fast spin echo (FSE) sequence[3] was used, with an effective echo time (TE) (defined as the time between the excitation and data acquisition over the center of k space (see appendix C)) of 80 ms, a Repetition Time (TR) (defined as the time between two sequential excitation pulses) of 1.5 s, a turbo factor of 9 (defined as the number of spin echoes that are used within a TR) and 2 signal averages (NSA) (defined as the number of times the signal is collected for an image). The parameters listed influence both the signal to noise ratio (SNR) and contrast of an image. As the phantom used in this chapter is homogeneous the choice of TR/TE (in terms of contrast) is somewhat arbitrary. Scans were performed with phase encode directions in both the right-left and foot-head directions.(figure. 5-2) The strength of read encode gradient was 5.74 mT/m

For comparison, a balanced fast field echo (BFFE) and a gradient echo scan were performed on the seed. For these scans, the seed was aligned with its long axis in the foot-head direction. Like the FSE scans above, the slice thickness was maintained at 1 mm. For the BFFE scan, the TR was 20 ms, the TE was 10 ms, the steady-state flip angle (see appendix C) was 45°and an NSA of 2 was used. The gradient echo scan was performed with a TR of 35 ms, a TE of 23 ms, a flip angle of 18° and an NSA of 2.

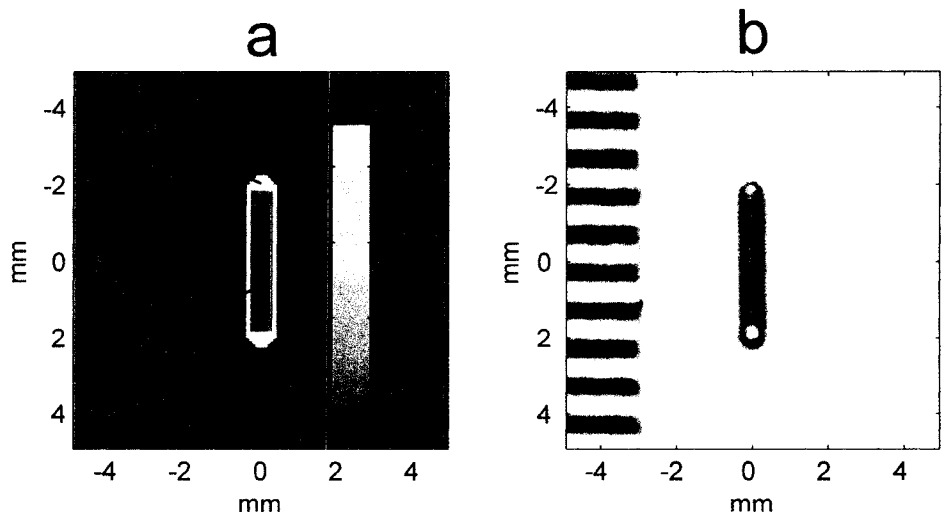

Figure. 5-1: (a) Diagram of seed components and their associated magnetic susceptibility values. (b) Photograph of Brachytherapy seed (OncoSeed, IMC6711).

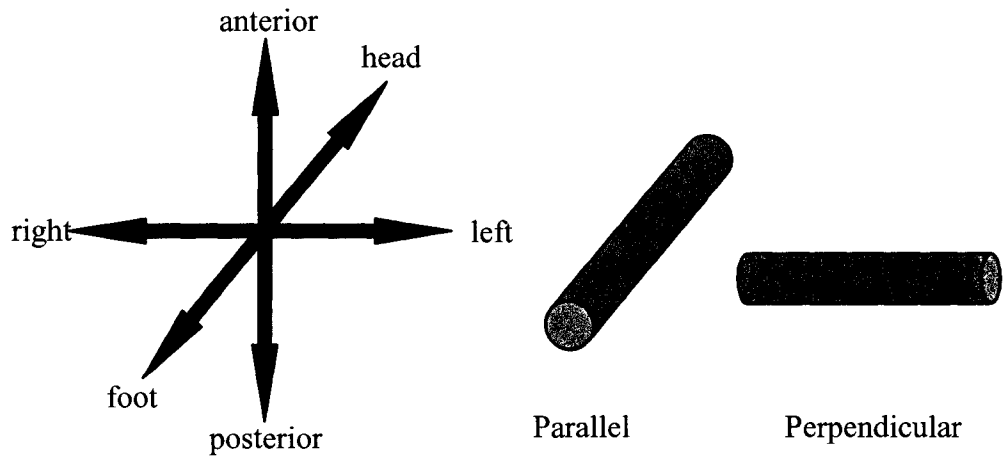

Figure. 5-2 Parallel and perpendicular alignments of the brachytherapy seed used in this chapter. The axis of the magnet bore and B_0 are both aligned with the Head/Foot axis. A coronal image would thus lie along the plane defined by the head/foot, left/right axis.

Additional FSE images were acquired on a different phantom. This phantom was constructed identically to the one described in 5.2.1, but with three pairs of seeds suspended in the gel instead of one. Each pair was arranged in-line with a different spacing for each pair: 0, 1.5, and 3 mm.(figure. 5-3) Two coronal images were acquired for each pair: one with the phase encode in the foot-head direction, and the other in the right-left direction. (figure. 5-3) The slice thickness was 1mm, the TE and TR were 30 ms and 1.5 s repectively and an NSA of 2 was used. The non-interpolated pixel size was 0.22 mm (interpolated 0.13), and the read encode gradient strength was 5.74 mT/m.

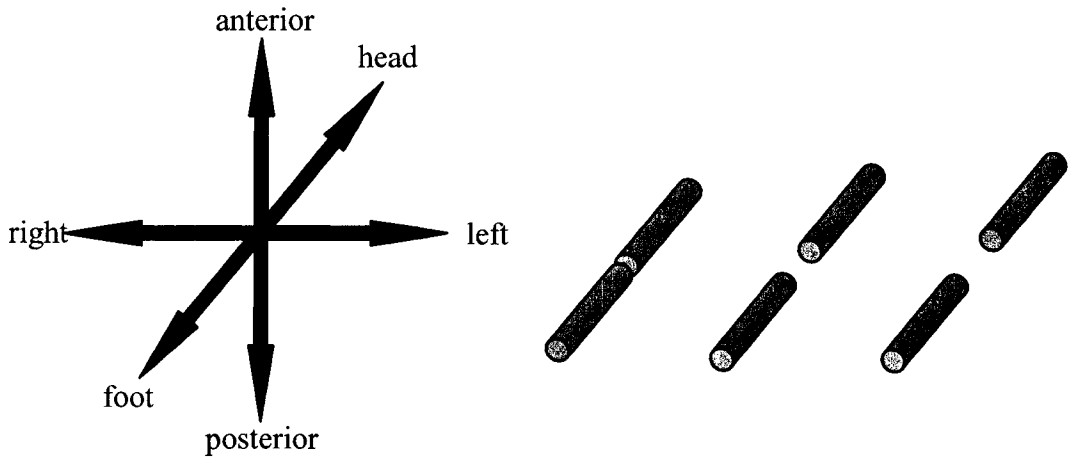

Figure. 5-3 Seed alignments for the seed pair phantom. The axis of the magnet bore and B_O are both aligned with the head/foot axis. A coronal image would thus lie along the plane defined by the head/foot, left/right axis.

A final imaging procedure saw the acquisition of two FSE images using the single-seed phantom. This time coronal images with 1 mm isotropic voxels were obtained with the seeds oriented in two different ways: firstly with the seed positioned

parallel to the bore,(figure. 5-2) and secondly with the seed rotated ~30° clockwise in the coronal plane. The scan employed a TE/TR of 30 ms and 1.5 s respectively, an NSA of 2 and a read encode gradient of 2.2 mT/m.

5.2.2 Simulated Images

5.2.2.1 Field Simulation

The simulation procedure was carried out using Matlab [The Math Works Inc. Natick, Ma] and in two stages. In the 1st stage, a high resolution magnetic field map was created based on the magnetic susceptibility constants and geometric arrangement of the seed components with respect to the main magnetic field (B_O) (figure. 5-1). As the end welds of the titanium shell were not well defined geometrically in available seed literature, they were assumed to be hemispheric and were modeled accordingly. The length of the titanium shell, including the two hemispheric welds (with radii of 0.4 mm) was taken to be 4.5 mm. The susceptibility of the silver rod and titanium casing were assigned values of -2.38×10^{-5} (Refs. 4,5), and 1.795×10^{-4} respectively (figure. 5-1) (Refs. 4,6). In all our simulations, as in the acquired MR images, the seed was positioned in a horizontal plane with respect to the B_O field. To make the simulation more realistic, the silver rod was made to rest on the lower surface of the titanium casing. This relative position of the silver rod with respect to the casing is expected to have little effect on the resultant magnetic field distribution given the order of magnitude increase of the susceptibility constant of the titanium as compared to the silver. The field map simulation was calculated using a three-dimensional extrapolation of the method described in Bhagwandien et al.[7]

The 1st step in the simulation is to introduce a uniform magnetic intensity field field **H** corresponding in our case to a nominal magnetic field of 1.5 T, according to the relation

$$\mathbf{H} = \frac{\mathbf{B}}{\mu_0}, \qquad 5.1$$

where μ_0 is the permeability of free space having a value of $4\pi \times 10^{-7}$ [H/m] and H has the units of A/m. To obtain a solution the magnetic scalar potential (Φ_M) is iterated forward. Φ_M is initially defined as

$$\mathbf{H} = -\nabla\Phi_M . \qquad 5.2$$

This initial definition assumes no induced macroscopic magnetization, **M**. An initial solution space was chosen with a three-dimensional span large enough to ensure that the induced magnetization will not perturb the boundary values of Φ_M away from there initial values in Eq. 5.2 (i.e. there will be no change in the initial boundary conditions). As solution time and memory requirements escalate rapidly with increased matrix size, it was necessary to iterate the solution several times. At each iteration the previous solution was used to define new boundary conditions surrounding a smaller region. Required for this numerical approach are both the spatial locations of the susceptibility constants and the magnetic scalar potential at the boundary.

Since from Maxwell's equations,

$$\nabla \cdot \mathbf{B} = 0, \qquad 5.3$$

and given that

$$\mathbf{B} = \mu_M \mathbf{H} \text{ (in linear media)}, \qquad 5.4$$

then Eq. 5.3 can be re-written:

$$\nabla \cdot (\mu_M \nabla \Phi_M) = 0. \qquad 5.5$$

The numerical solution is based on Eq. 5.5 with the magnetic permeability (μ_M) distribution required in Eqs. 5.4 and 5.5 is defined according to

$$\mu_M = \mu_0 (1 + \chi_M), \qquad 5.6$$

where χ_M is the dimensionless magnetic susceptibility constant.

An artificial iteration parameter τ is introduced such that.

$\frac{d\Phi_M}{d\tau} \to 0$, as $\tau \to \infty$. Hence, Eq. 5.5 can be re-written as

$$\Phi_M(\mathbf{r};\tau + d\tau) - \Phi_M(\mathbf{r};\tau) = \nabla \cdot (\mu_M(\mathbf{r}) \nabla \Phi_M(\mathbf{r};\tau)). \qquad 5.7$$

As τ is iterated forward, Φ_M will converge to a solution.[7] To implement this a three-dimensional mesh with node distance dL was created, such that the derivatives from the operators in Eq. 5.7 could be approximated at any point by using the mesh values immediately surrounding it (figure. 5-4). The derivatives were determined using finite difference approximations such that:

$$\Phi_M(0;\tau+d\tau)-\Phi_M(0;\tau)=\sum_{i=1}^{6}C(i)*\Phi_M(i;\tau)+C(7)*\Phi_M(0;\tau), \qquad 5.8$$

where the C coefficients are constants described by

$$C(i)=\left[\mu_M(0)+\frac{\mu_M(i)}{4}-\frac{\mu_M\left(rem\left(\frac{i+3}{6}\right)\right)}{4}\right]\times\frac{d\tau}{\mu_0(dL)^2} \text{ for i = 1 to 6, and}$$

$$C(7)=-\frac{6\mu_M(0)\cdot d\tau}{\mu_0(dL)^2}. \qquad 5.9$$

To ensure a stable convergence, the maximum step of the iteration parameter $d\tau$, is defined as

$$d\tau \leq \frac{\mu_0 (dL)^2}{6\mu_M}, \qquad 5.10$$

according to the Fourier criterion.[8] For our case μ is taken to be the largest magnetic permeability value in the object, to ensure proper convergence over the whole model.

In order to accelerate convergence and reduce computation time, a modification as per the Du Fort-Frankel algorithm[9] can be made by replacing the left hand term

$$\Phi_M(0;\tau) \text{ by } \Phi_M(0;\tau - d\tau). \qquad 5.11$$

and the right hand term

$$\Phi_M(0;\tau) \text{ by } \frac{\Phi_M(0;\tau + d\tau) + \Phi_M(0;\tau - d\tau)}{2}. \qquad 5.12$$

This gives the new algorithm

$$\Phi_M(0;\tau + d\tau) = \sum_{i=1}^{6} D(i) * \Phi_M(i;\tau) + D(7) * \Phi_M(0;\tau - d\tau), \qquad 5.13$$

where the D coefficients are new constants based on the ones calculated previously:

$$D(i) = \frac{2 * C(i)}{2 - C(7)} \text{ for } i = 1 \text{ to } 6, \text{ and}$$

$$D(7) = \frac{2 + C(7)}{2 - C(7)}. \qquad 5.14$$

This algorithm is unconditionally stable for an arbitrary iteration step $d\tau$.[10] Use of this algorithm allows $d\tau$ to be increased by a factor of up to 100 (Ref. 10), while maintaining stability. The computation time for a 128x128x16 matrix field simulation on a Pentium 4, 2.4 GHz computer is 2.5 minutes.

5.2.2.2 Fast spin echo image prediction

In the second stage, the field map determined in the first stage was used to simulate MR images as they would appear according to our model. To model the potential signal for the FSE sequence investigated, a binary signal matrix (M_{SIG}) of the same dimensions as the magnetic distortion map was created in which the signal was 1 everywhere except within locations corresponding to positions within the volume of the seed in which case it was 0. This matrix describes where H^1 protons are available to deliver signal if excited (i.e. everywhere but within the seed itself).

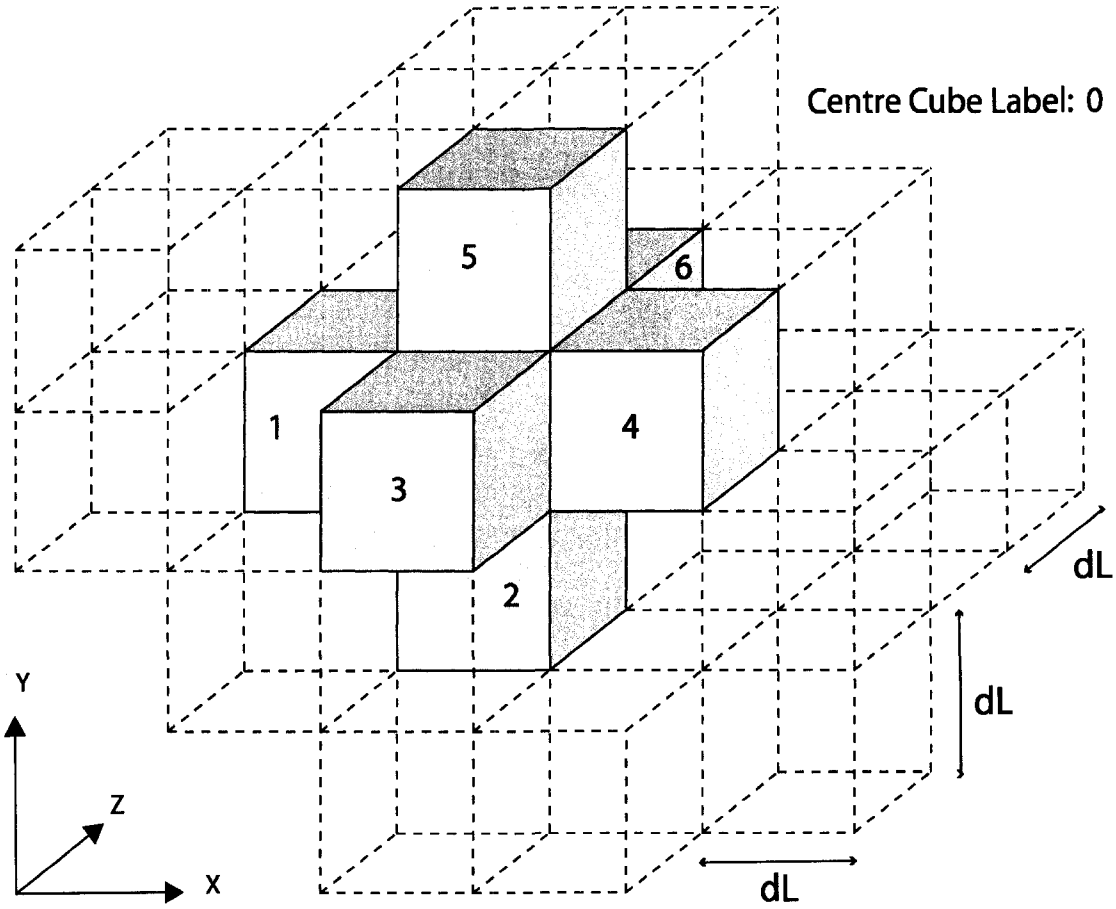

Figure. 5-4 Diagram of the mesh grid upon which the numerical solution is implemented.

The major assumption in our model of the FSE sequence is that all transverse magnetization (M_{xy}) whose absolute value gives rise to the signal within any voxel was refocused by the 180 degree refocusing pulses. Thus any dephasing is due solely to T2 dephasing which is largely insensitive to the background field.[11] In light of this there were two primary mechanisms for the imaging artifacts present when imaging with the FSE sequence. The 1st mechanism arrives due to the effect of the magnetic distortion on the precession frequency of the H^1 protons being excited. This distortion causes some protons in close proximity to the seed to avoid the resonance condition of the applied excitation pulse and thus fail to be excited. In addition to this, other H^1 protons which are intended to be excluded from excitation by use of the slice selection gradient will as a result of the magnetic distortion fall into the resonance criteria and thus be excited producing M_{xy} magnetization. To model this affect during slice selection, a slice selection gradient (G_{SS}) in mT was added to the magnetic distortion map F_Z (which includes both the distortion and the Bo field) and a binary slice selective mask (M_{SS}) was created according to:

$$M_{SS} = 1 \quad \text{where } |\mathbf{F}_Z + \mathbf{G}_{ss} - B_0| \leq (sl/2 \times g_{SS}), \text{ and} \qquad 5.15$$

$$M_{SS} = 0 \quad \text{where } |\mathbf{F}_Z + \mathbf{G}_{ss} - B_0| > (sl/2 \times g_{SS})$$

where M_{SS} is the slice selective mask, B_0 is the 1.5 T main magnetic field, sl is the slice thickness, and g_{SS} mT/m is the nominal slice-selective gradient strength. The simulations were obtained using the same slice-select gradient strength as was employed in the MR scans. Because we assume complete signal refocusing for the

FSE sequence the available M_{xy} magnetization during the frequency encode/signal acquisition stage is determined according to:

$$Sig_{FSE} = M_{SIG} \times M_{SS} \qquad 5.16$$

The 2nd distortion mechanism arrives due to the misrepresentation of the spatial locations of the M_{xy} magnetization which occurs during the frequency encoding. The locations of the misrepresented M_{xy} magnetization in the image were determined according to:

$$\begin{bmatrix} x^*_{SIG} \\ y^*_{SIG} \\ z^*_{SIG} \\ 1 \end{bmatrix} = \begin{bmatrix} 1 & 0 & 0 & (F_Z(x_{SIG}, y_{SIG}, z_{SIG}) - B_0)/g_{xR} \\ 0 & 1 & 0 & (F_Z(x_{SIG}, y_{SIG}, z_{SIG}) - B_0)/g_{yR} \\ 0 & 0 & 1 & (F_Z(x_{SIG}, y_{SIG}, z_{SIG}) - B_0)/g_{zR} \\ 0 & 0 & 0 & 1 \end{bmatrix} \begin{bmatrix} x_{SIG} \\ y_{SIG} \\ z_{SIG} \\ 1 \end{bmatrix} \qquad 5.17$$

where x^*_{SIG}, y^*_{SIG} and z^*_{SIG} are the apparent positions of the real and imaginary components of the M_{xy} magnetization and g_{xR}, g_{yR} and g_{zR} are the X, Y and Z components of the read gradient. $F_Z(x_{SIG},y_{SIG},z_{SIG})$ is the distorted magnetic field strength at the correct M_{xy} magnetization locations x_{SIG},y_{SIG},z_{SIG}. The simulations were obtained using the same read encode gradient strength as was employed in the MR scans.

Due to the large susceptibility differences present in the brachytherapy seed, the intra-voxel gradient of magnetic field distortion can be substantial. In light of this,

assigning the magnetization within a voxel a single displacement leads to pixilation of the predicted image. (figure. 5-5) In order to remedy this problem, the displacements in the read encode direction were calculated using the F_Z distortion map which was interpolated (with a spline interpolation) by a factor of 15 (chosen arbitrarily to produce a satisfactory image). The signal from the source voxels was then distributed accordingly. It should be noted there will be no such shift in the phase encode direction. This is because there will be no change in the phase accumulated between adjacent phase encode steps. Finally the three dimensional signal matrix was summed in the slice select direction to yield a simulated MR image. The computation time for a 128x128x16 matrix image simulation on a Pentium 4, 2.4 GHz computer is 69 seconds.

5.2.3 Center of Mass Calculations

Centre-of-mass calculations were implemented on all the high resolution FSE simulations as described above. A threshold was set at one half of the average surrounding gel signal, and the regions that were included in the calculation were those that fell below. All values within the artifact were equally weighted for the center-of-mass determination. This calculation provided an estimate of possible seed position errors.

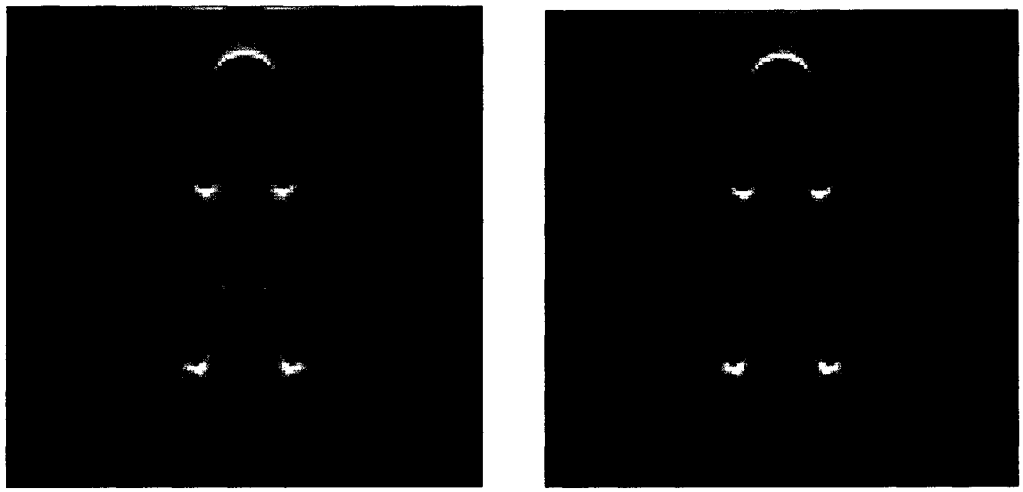

a) b)

Figure. 5-5 demonstrates the pixilation which occurs from assigning magnetization within a voxel a single displacement. a) is determined with no interpolation b) is determined with a factor of 15 interpolation.

5.2.4 Normalized Cross Correlation Comparison

Two single-seed images with 1 mm isotropic resolution were obtained with different orientations in the coronal plane (chosen arbitrarily). The first was parallel to the bore, and the 2nd was rotated roughly 30° clockwise from it (as described in Methods and Materials A.). An array of high resolution simulations (with pixels at 78 um) was simulated at 5 degree intervals of rotation between -40° and 40° with respect to the bore. Each simulation in the array was then compared to both of the low resolution images according to a normalized two-dimensional cross-correlation algorithm. These results were then used to identify the optimally oriented simulation as well as position of the seed within the experimentally acquired image. The reason for this was to demonstrate that images acquired under realistic in-vivo resolutions

would retain sufficiently distinct distortion patterns as to allow the effective use of the simulations in pinpointing the seed location.

5.3 Results and Discussion

Magnetic field maps in column (a) of figures. 5-6 through 5-8 show magnetic field distortions caused by the presence of the brachytherapy seed within the B_O field. The greatest field effects were found to occur in close proximity to the end welds of the seed. These areas of large field effect are also where the largest image distortions are expected. It can be seen that the spatial distribution of distortion is dependant on the orientation of the seed with respect to the B_O field.

As per the magnetic field maps, the simulated MR images predicted a distinct characteristic shape that is dependant on the seed's orientation with respect to the magnetic field, as well as the read encoding gradient direction and strength. The simulated images are displayed in column (b) of figures. 5-6 through 5-8, adjacent to their corresponding experimentally-acquired MR images in column (c). In general, the simulations were visually successful at predicting the MR image distortions. Minor discrepancies between the alignment of the seed generated in the model and that of the experimental images will result in marginal differences in image appearance. In addition to this, because of the large memory requirements our seed susceptibility maps had a resolution limit of 78 μm. This pixilation in the seed susceptibility maps may result in some additional minor discrepancies in the image artifacts particularly in the region of the titanium shell walls, which are only 50 μm thick.

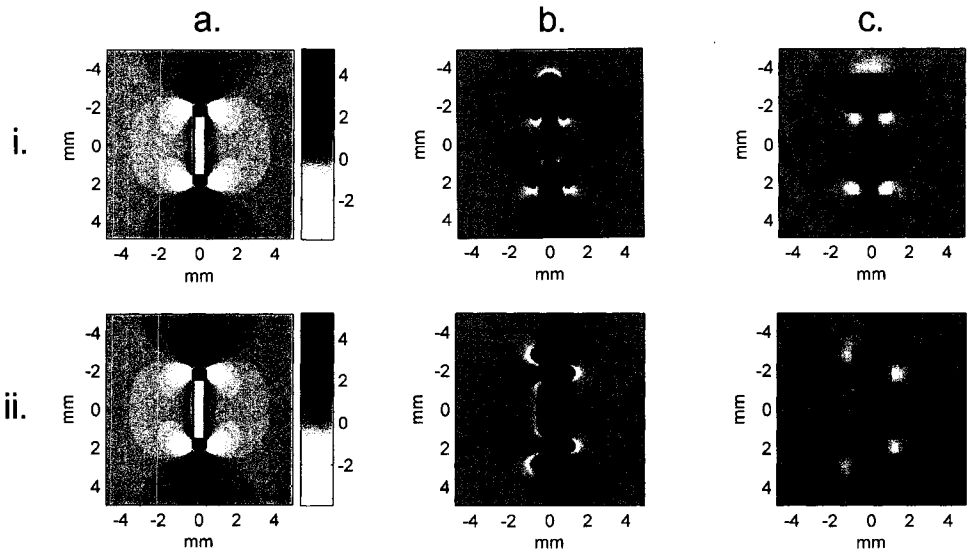

Figure. 5-6 Column (a) Magnetic field distortion maps for a brachytherapy seed placed parallel to the main magnetic field. Field distortion values (in ppm) are scaled as [sign(PPM) × ln(|PPM| + 1)] for better visualization. Column (b) The corresponding image simulations. Column (c) Experimentally acquired MR images for the same orientation and imaging conditions, displayed in the same scale as the simulations. The MR images were spline-interpolated by a factor of 2 for better visualization. The images in row (i) result from a read gradient, G_R, parallel to the main magnetic field (vertical axis), and in row (ii), perpendicular.

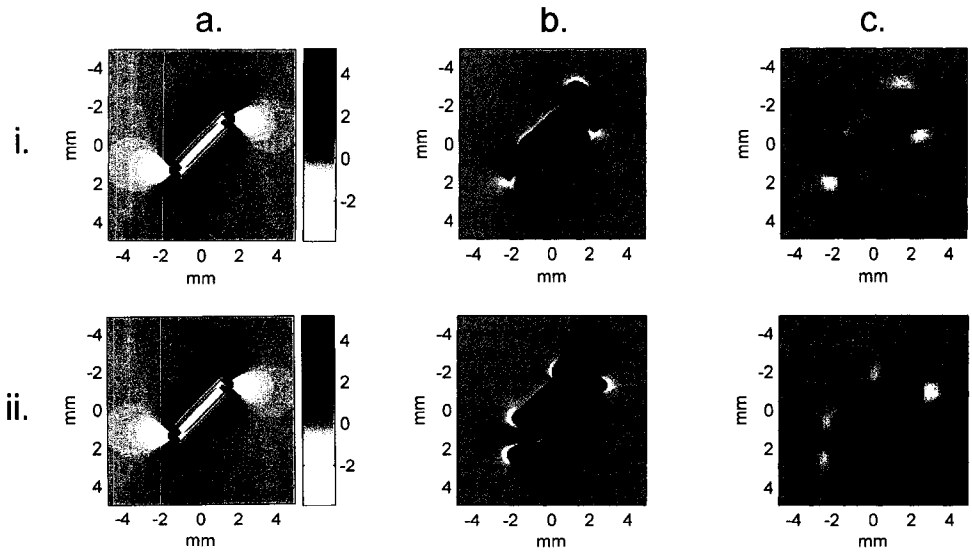

Figure. 5-7 Same as figure. 5-6, but with the seed oriented 45° to the axis of the main magnetic field.

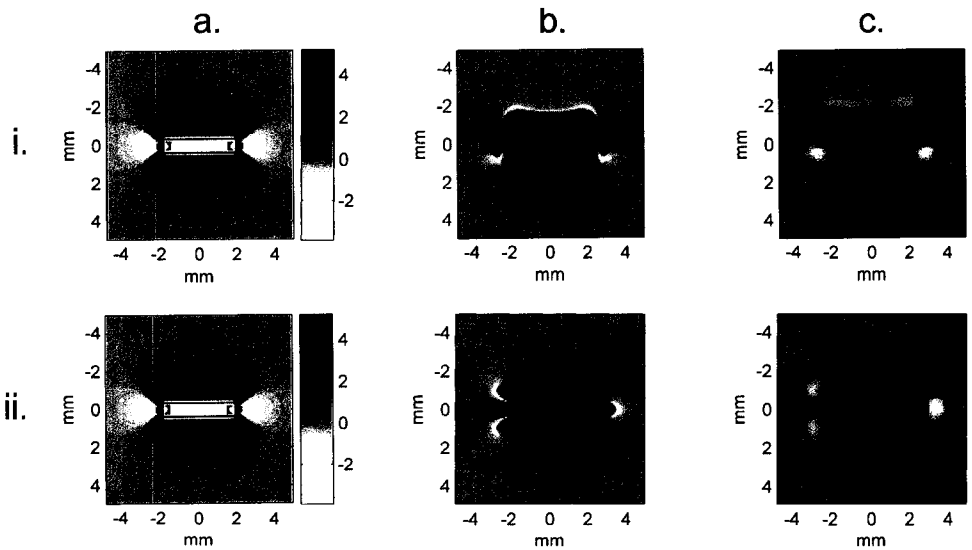

Figure. 5-8 Same as figure. 5-6, but with the seed oriented perpendicular to the axis of the main magnetic field.

The image artifacts depicted in the images shown should be scene in any pulse sequences employing unidirectional linear read encode trajectories. Techniques other than spin echo will be expected to exhibit additional distortions. Gradient echo images will have additional blurring due to intra-voxel dephasing losses within the magnetic field distortions around the seed (figure. 5-9(c)), and banding may occur around the seed in BFFE images due to induced off-resonance effects (figure. 5-9(b)).

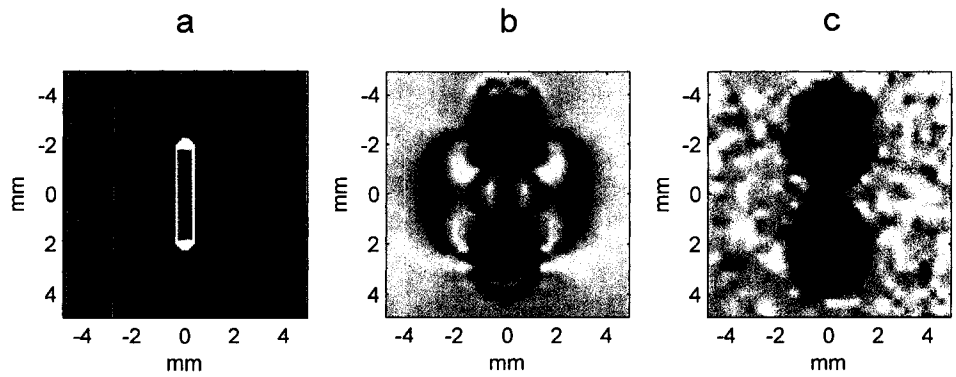

Figure. 5-9 (a) Scale representation of the seed component geometry. (b) BFFE image of the brachytherapy seed. (c) Gradient echo image of the brachytherapy seed. The images were spline-interpolated by a factor of 4 for better visualization.

Image simulations with the contours of the brachytherapy seed overlain are shown in figure. 5-10. It can be clearly seen that the artifacts extend past the brachytherapy seed itself. Use of these computer simulations of the images allow one to know the position of the seed within the characteristic distortion pattern. Furthermore the image artifact with respect to seed geometry opens the possibility of misinterpretation of the true seed location. Having no *a-priori* knowledge of the image distortions pattern may lead

to misinterpretation of the seed position with an error on the order of millimeters using the MR scans alone.

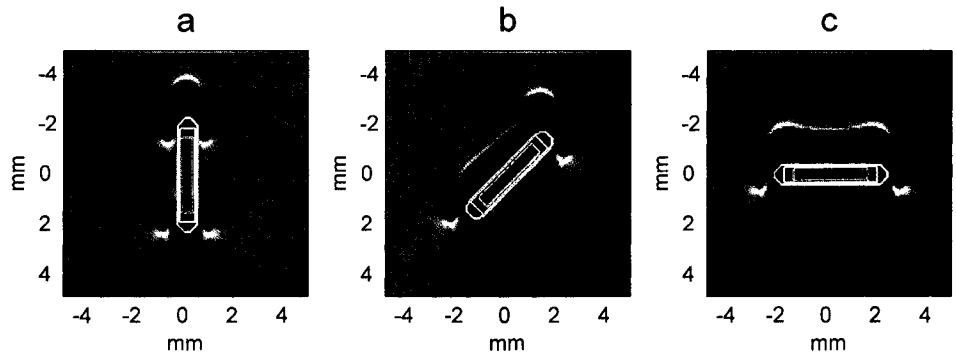

Figure. 5-10 Simulated images of a brachytherapy seed with the contours of the source brachytherapy seed geometry overlaid. In all three cases, both the main magnetic field and the read encode direction are parallel with the vertical axis.

Discrepancies between the centers-of-mass and the center of the true seed location are provided in table 1. The maximum discrepancy from this calculation was found to be 1.9 mm. Although this discrepancy will vary with the approach used to define the artifact region (the threshold value used here was very arbitrary) the discrepancies quoted in table 1 agree within error to those determined experimentally by Dubois et al.[12] The average displacement value quoted by Dubois et al. was 1.67 +/- 0.76 mm for seeds placed parallel to the bore. This same group found a similar displacement value of (1.59 +/- 0.64 mm) for the same experiment performed using CT. Dubois et al. did not state the reason for the error in the CT data set.

Table. 5-1. Deviation in mm between the artifact centre-of-mass and the seed centre for different seed orientations and read encode directions

Read Encode	Orientation of Seed		
	Parallel	45 degrees	Perpendicular
Foot-Head	1.7	1.1	1.1
Right-Left	1.9	0.5	0.8

As previously stated the errors in seed localization when viewing one seed images are likely limited to a few millimeters when using a spin echo technique. It is however possible that error of a greater magnitude may be present when a number of seeds are imaged in close geometrical proximity. In this situation distortions which extend beyond the seed geometry may make ascertaining where one seed ends and another begins, particularly difficult. It is plausible that in some situations the distortion artifacts appear more prominent than the seed geometry which may in higher noise images, lead to a distortion pattern being interpreted as two individual seeds. (For example, note in figure. 5-6c the top and bottom lobes of the distortion patterns.) In these circumstances, models of multiple seed may be of use in identifying the correct seed locations.

Images from three pairs of seeds with inter-seed spacings of 0, 1.5 and 3 mm along with their corresponding simulations are shown in figure. 5-11. This figure demonstrates that the simulation is capable of describing the image artifacts under the rigorous conditions of multiple seeds in close proximity. These two-seed simulations show good qualitative agreement with the measured images in pattern. Some minor discrepancies are expected between the model and the experimental images which may

result from limitations in the accuracy of seed placement when suspending the seeds in gelatin phantom.

Images of simulations varying between -40° and 40° rotation in 5° increments as well as the maximum normalized cross-correlation value associated with each simulation are shown in figure. 5-12(a). Shown in figure. 5-12(b) are the original low resolution images for both seed rotations in addition to a superposition of the appropriate simulation and image. Also shown in figure. 5-12(b) is an overlay of the seed outline on the low resolution image as determined by the normalized cross-correlation technique. For the 2 cases investigated the normalized cross correlation was successful in matching simulation to experiment for both the 0° and 30° rotated seeds. The method of the normalized cross correlation also provided a means to numerically identify the optimum location of the seed in the image (figure. 5-12(b)). The prostate tissue and surrounding anatomy is relatively homogeneous as compared to the massive susceptibility gradient surrounding the seed. Thus we expect no appreciable differences in the characteristic distortion pattern surrounding the brachytherapy seeds, whether in a gelatin phantom or implanted in vivo.

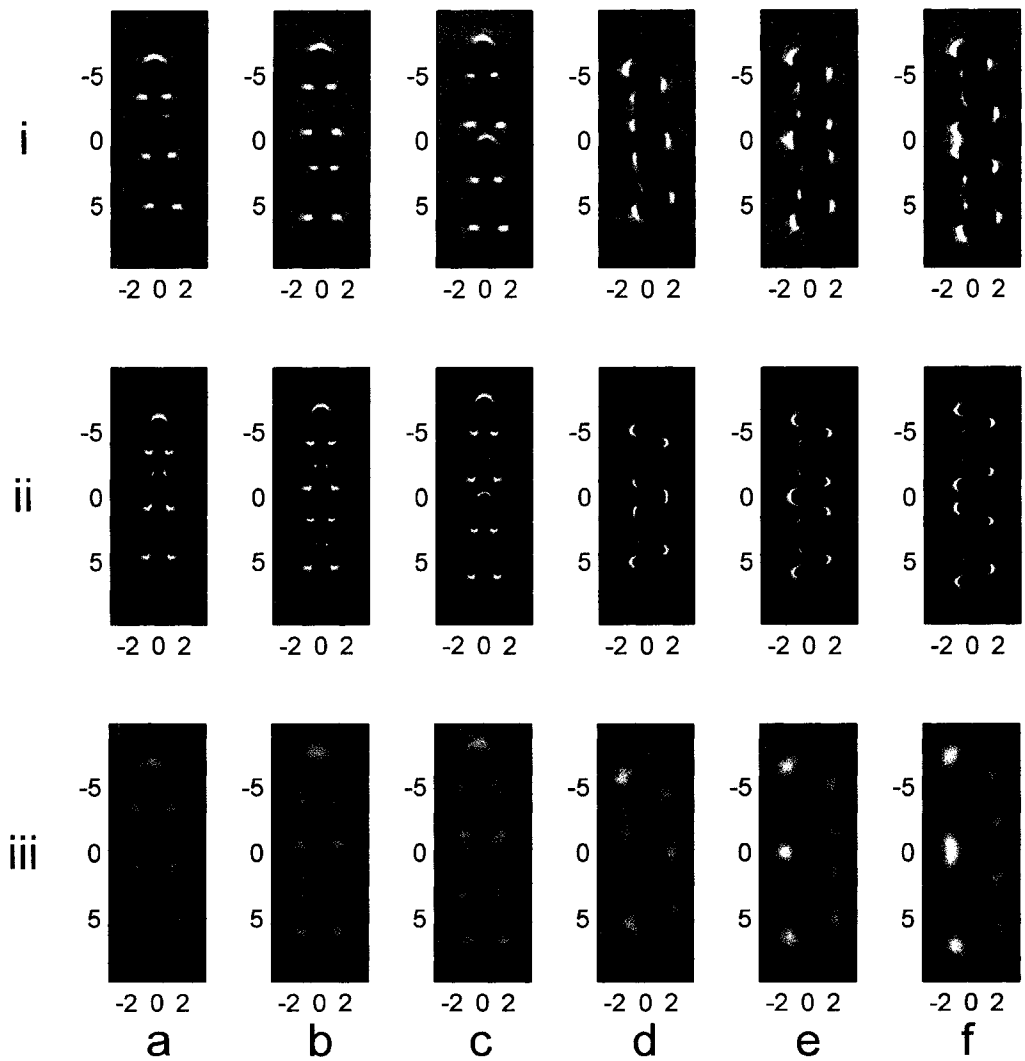

Figure. 5-11 Three pairs of brachytherapy seeds arranged in-line and separated by 0, 1.5, and 3mm were imaged with the read encode direction parallel to (a-c) and then perpendicular to (d-f) the axis of the seeds. Dimensions are given in mm. Row i displays high-resolution experimental images of the seed pairs, row ii shows corresponding image simulations, and row iii displays the same experimental images as in i, but reconstructed with truncated k-space data to obtain images with resolutions realistic of in-vivo imaging (1 mm pixels prior to interpolation).

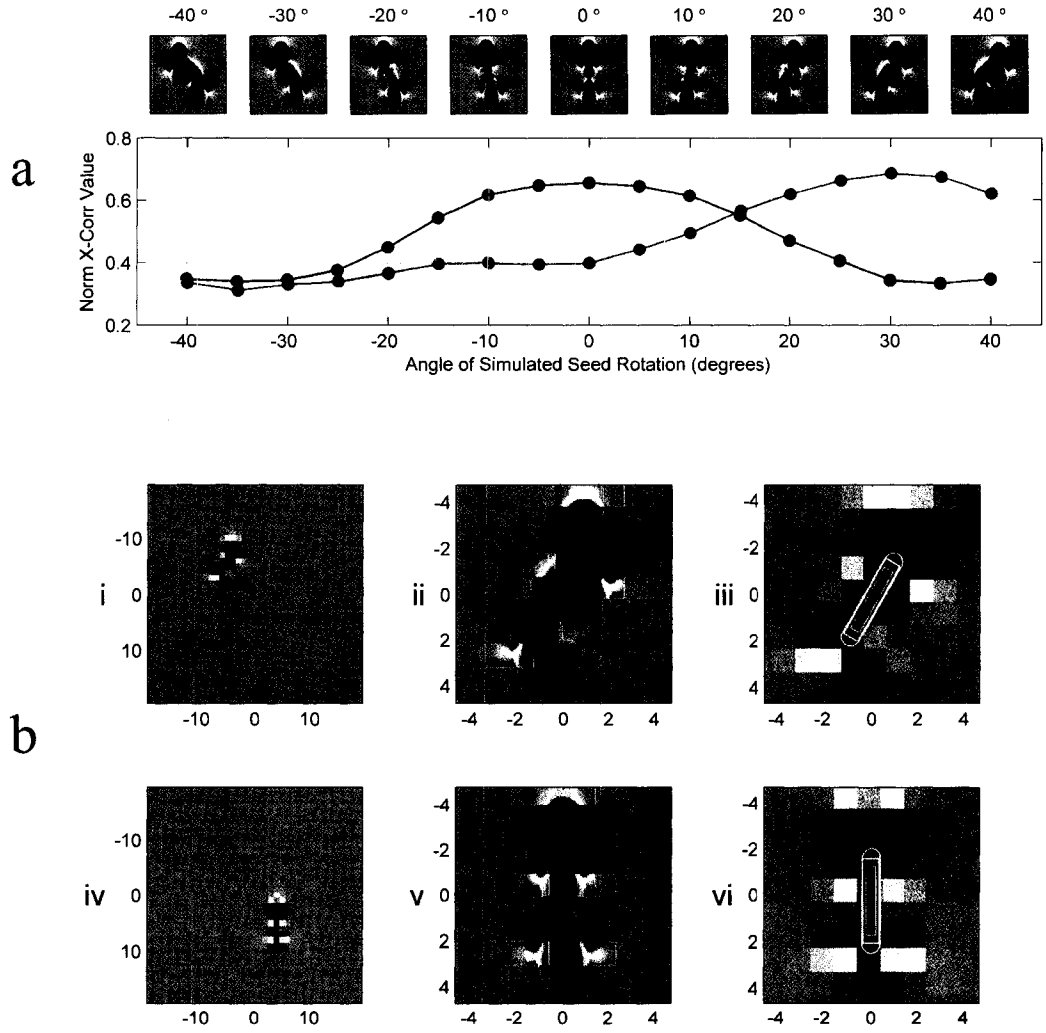

Figure. 5-12 (a) selection of simulation images at different angles of rotation with respect to B_0. Also displayed are the maximum normalized cross correlation value for every simulation (The red line corresponds to the seed rotated 30°, blue lines are for the seed rotated 0°). (b) Each row outlines the fitting procedure, beginning with the original image in i and iv, the superposition of the experimental image and appropriate simulation as determine by the normalized cross-correlation technique in ii and v, and the final determined position of the seed within the experimental images in iii and vi. Dimensions are given in mm.

5.4 Conclusions

The characteristic distortions for a typical brachytherapy seed within a clinical 1.5 T MR imager were measured experimentally. The measured results show significant deviations from the physical seed geometry. The distortion patterns were found to vary with both the orientation to the main magnetic field, as well as with the read encode direction. Simulations of the images based on the magnetic field induced by the brachytherapy seed materials were successfully performed allowing accurate localization of the seed within the distortion pattern. These distortions simulated and experimentally shown will be present in all images acquired using a unidirectional linear read encode trajectory. These distortion patterns proved to be sufficiently distinct to allow for successful automatic localization in two dimensions using the normalized cross correlation method at resolutions down to 1 mm. Other techniques such as gradient echo and BFFE will have further artifacts in addition to those demonstrated. Given the highly predictable nature of these distortion patterns offers the hope that perhaps an automatic localization algorithm can be produced that can pinpoint the location of implanted seeds from a single three dimensional MR scan.

References

[1] D.F. Dubois, B.R. Prestidge, L.A. Hotchkiss, W.S.Bice Jr., J.J. Prete, "Source localization following permanent transperineal prostate interstitial brachytherapy using magnetic resonance imaging," Int. J. Radiat. Oncol. Biol. Phys. **39**, 1037-1041 (1997).

[2] F.V. Coakley, H.Hricak, A.E Wefer, J.L Speight, J. Kurhanewicz, M.Roach III, "Brachytherapy for prostate cancer: Endorectal MR imaging of local treatment related changes," Radiology **219**, 817-821 (2001).

[3] J. Hennig, A. Nauerth, H. Friedburg, "RARE imaging: a fast imaging method for clinical MR," Magn. Reson. Med. **3**, 823-833 (1986).

[4] J.F. Schenck, "Review article: Role of magnetic susceptivility in MRI," Med. Phys. **23**, 815-850 (1996).

[5] R.R. Gupta, Diamagnetic Susceptibility, Vol II/16 of Landolt-Bornstein, Numerical Data and Functional Relationships in Science and Technology, Springer-Verlag, Berlin, (1986).

[6] E.W. Collins, P.C. Gehlen, "Some observations of the temperature dependences of magnetic susceptibility of titanium and titanium-aluminum," J. Phys. F: Met. Phys. **1**, 908-919 (1971).

[7] R. Bhagwandien, R. van Ee, R. Beersma, C.J.G. Bakker, M.A. Moerland, J.J.W. Lagendijk, "Numerical analysis of the magnetic field for arbitrary magnetic susceptibility distributions in 2D," Magn. Reson. Imag. **10**, 299-313 (1992).

[8] D.R. Croft and D.G. Lilly, Heat Transfer Calculations Using Finite Difference Equations, Applied Science Publishers, London, (1977).

[9] A.R. Mitchell and D.F. Griffiths, The Finite Difference Method in Partial Differential Equations, John Wiley and Sons, New York, (1990).

[10] J. Mooibroek and J.J.W. Lagendijk, "A fast and simple algorithm for the calculation of convective heat transfer by large vessels in three dimensional inhomogeneous tissues," IEEE Trans. Biomed. Eng. 38, 490-501 (1991).

[11] M.J Bronskill The physics of MRI 1992 summer school proceedings, Woodbury: American Institute of Physics, Inc (1993)

[12] D.F. Dubois, W.S. Bice, Jr., B.R. Prestige, "CT and MRI derived source localization error in a custom prostate phantom using automated image coregistration," Med. Phys. 28(11), 2280-2284 (2001).

Chapter 8: Imaging a prostate brachytherapy seed at 1.5 and 3.0 Tesla: an in Vitro study.

6.1 Introduction

The use of Brachytherapy with transrectal ultrasonography-guided transperineal implantation of interstitial radioactive seeds has become an accepted method for treating localized prostate cancer.[1,2] Although providing excellent anatomical delineation, post-implant evaluation using magnetic resonance imaging (MRI) - where seeds are typically viewed as signal voids- has met with limited success due to the large uncertainty associated with seed position.[3] As a result, evaluation currently relies on CT. The use of 3.0 Tesla clinical scanners with their associated increase in signal to noise ratio (SNR) allows for increased resolution which may resolve the issue of seed location uncertainty. The increased background field may however increase the magnitude of the image artifacts due to the increased magnitude of the susceptibility effects.[4] A comparison of seed images acquired at 3.0 T vs 1.5 T is required to assertain wether there is any advantage to be gained by imaging at higher field.

In this chapter, we investigate the artifacts generated when imaging a brachytherapy seed using two common imaging techniques and the effect of the background field B_O on these artifacts. The two imaging sequences investigated are fast spin echo FSE, and GE.[5,6] These two sequences were chosen as they represent the two primary imaging sequences employed today. Images of a brachytherapy seed in a 3% by weight porcine gel phantom are acquired at 1.5 and 3.0T. As the seed was

suspended in the uniform gel medium, no further constructs were required to stabilize the seed position. This allows the seed image artifacts to be assessed without complications arising from materials used to position the seed. Furthermore, the gel allows us to place the seed in known orientations which would be difficult to accomplish in-vivo. Finally, this method allows us to investigate the image artifact without concern of localized specific absorption rate issues which may be an issue when imaging in-vivo at the higher 3.0 T field strength. The specific absorption rate refers to the rate at which RF energy from the circularly polarized magnetic field (see appendix C) is deposited as heat. Single seed images are acquired with the seed orientated at 0° (parallel) and 45° with respect to B_O in the horizontal plane. For the GE acquired images, the effect of echo time was investigated. Images of two seeds in a parallel aligned configuration (figure. 6-1) are also taken with inter seed gaps of 0, 1.5, 3, 4.5 and 6 mm in order to determine the inter seed gaps required to completely distinguish two individual seeds. A third fast imaging sequence which is commonly used is balanced fast field echo (BFFE).[7,8] The artifact resulting from the BFFE technique is demonstrated however no analysis is performed. This study aims to provide an indicator as to the feasibility of identifying seeds in-vivo at the higher 3.0 T field strength. It should also aid in analyzing later in-vivo measurements by providing a baseline as to shape and size of the artifacts.

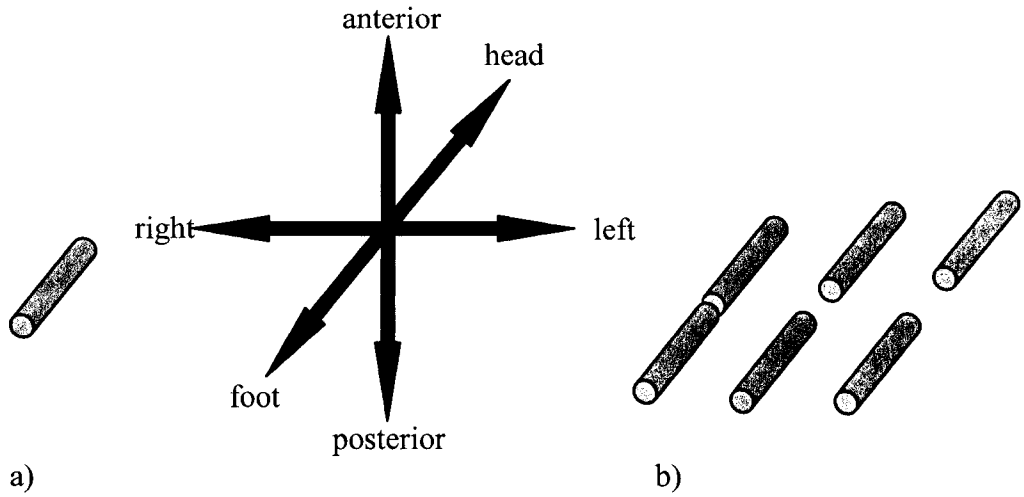

Figure. 6-1 Seed alignments for a single parallel seed a) and the seed pair phantom b). The axis of the magnet bore and B_O are both aligned with the head/foot axis. A transverse image would thus lie along the plane defined by the anterior/posterior, left/right axis.

6.2 Methods and Materials

6.2.1 Materials

The imaging phantom is produced by suspending, a single brachytherapy seed (IMC6711, OncoSeedTM) in 3% by weight, porcine gel. The outer physical geometry of the seed's titanium casing is cylindrical with two roughly hemispherical ends. The seed measures 4.5 mm from tip to tip, and its outer diameter is 0.8 mm. The first step of the phantom's construction involved combining boiling water with 3% gelatin (~300 bloom) by weight. The mixture was then divided into two equal quantities; one quantity was refrigerated to help the gel set and the other was left in hot water to inhibit solidification. After the first quantity had set until there was a thin film on top, the second (still liquid) quantity was slowly added to the top. The brachytherapy seed was carefully placed on top of the thin skin between the refrigerated and liquid layers.

The gel was then left for several hours until both layers were completely set. An additional phantom with two seeds in a parallel aligned configuration with inter- seed gaps of 0 1.5, 3.0, 4.5, 6.0 mm was made using 1.5 mm plastic shims which were placed between the two seeds and then carefully removed. All images were obtained on both 1.5 T and 3.0 T Philips Intera whole-body scanners. For the 1.5 T acquired images, excitation was performed using the body coil while the signal was received using the head coil. For the 3.0 T acquired images a head coil was used for both excitation and signal detection. The difference in the coils used with each MR scanner was solely a function of equipment availability and is not expected to affect the results of this study.

6.2.2 Imaging

6.2.2.1 Fast Spin Echo

Images were acquired with the seed both parallel to the axis of the magnet bore and 45° off axis to the magnet bore in the horizontal plane. The two orientations were chosen as they represent a range of what may occur in-vivo. Two dimensional FSE transverse images were acquired with the following parameters: slice thicknesses (sl) of 1, 3, and 5 mm, a 0 mm slice gap, a field of view (FOV) of 160 mm, a 256X256 sampling grid, and a right/left frequency encode direction.(figure. 6-1) Other parameters were a frequency encode gradient of 11.63 mT/m, an echo time (TE) of 8 ms, a repetition time (TR) of 3000 ms, a turbo factor of 16, and 2 signal averages (NSA). The number of slices was chosen to cover 4 cm in the slice direction. All the images were reconstructed in the coronal direction using multi-planar reconstruction

(MPR) provided by the Philips scanner software. The MPRs had a reconstructed voxel size of 0.625 X 0.625 X 0.625 mm^3. Images were reconstructed in the coronal plane to better demonstrate the entire brachytherapy seed artifact. The images were acquired 5 times for each resolution and for each of the five times, the slice center was moved forward 20% of the slice thickness. These five images are intended to give an estimate of the error for both the distortion volume and length that would result from slice averaging. Transverse images for the 2 seed phantom were acquired using the same parameters as for the one seed phantom except that only 1 mm slice thicknesses were used.

6.2.2.2 Gradient Echo

Two-dimensional transverse GE images were acquired with the following parameters: sl of 1, 3 and 5 mm with 0 mm slice gap, field of view (FOV) of 160 mm acquired on a 256X256 sampling grid, right/left frequency encode direction, frequency encode gradient of 11.63 mT/m, TEs of 11 and 22 ms, a TR of 300 ms, and 2 NSA. Again, the number of slices was chosen to cover 4 cm in the slice direction. Images were reconstructed in the coronal direction using MPR with a 0.625 mm slice thickness and a 0.625 mm in plane resolution. Again, for each slice thickness, five images were acquired. Transverse images for the 2 seed phantom were acquired using the same parameters as for the one seed phantom except that only 1 mm slice thicknesses were used. Finally a set of coronal images were acquired using a 1 mm sl with all other parameters as listed above for TEs of 5.5, 11, 16.5 and 22 msec. This

was done to give a more complete idea of how TE effects the image artifact for each field strength.

6.2.2.3 Balanced Fast Field Echo

Three-dimensional transverse BFFE images were acquired with the following parameters: field of view (FOV) of 160 mm acquired on a 256X256 sampling grid, right/left frequency encode direction, TEs of 3.25 ms, TR of 6.5 ms, 2 NSA and receiver offset frequencies of 0, 25, 50 and 75 Hz. The number of slices was chosen to cover 3 cm in the slice direction. A 3-dimensional sequence was chosen because the BFFE sequence does not cater to interleaved multi-slice so there was no time penalty for acquiring a 3-dimensional data set. Another image was taken with 4 NSA using balanced fast field echo offset averaging in order reduce the banding artifact.[8] No analysis was performed due to the fact that the images depend on both the T1 and T2 time constants which are different between the gel phantom and the prostate, and the artifacts are expected to differ from those that would be found in-vivo. Thus the analysis would be of limited use in-vivo. Although the specifics of the image artifact will change depending on the tissue in which the seed reside, the basic characteristics will remain the same and thus it was felt that including the images was prudent for completeness.

6.2.3 Analysis

All of the analysis for the brachytherapy seeds was performed with Matlab [The Math Works Inc. Natick, Ma]. The data sets analyzed are the coronal MPRs. For the single-seed analysis, 40 X 40 X 40 pixels surrounding the center of the image artifact (as judged by the authors) were taken to be the local region of interest. All images were normalized to the mean signal surrounding the artifact (where the mean signal around the artifact was given a value of 1). This was done by determining the mean value within 400 pixels on each slice (10 pixels X 10 pixels from each corner within the local area of interest). The image artifact was taken to be where the normalized signal dropped below 0.75. The literature generally describes the seed artifact as a signal void[1,2] so although the image artifact contains portions of elevated signal, these are not considered in the analysis of the artifact volume or dimensions. The length and width of the image artifact were respectively taken to be the longest dimension parallel and perpendicular to the direction of the seed. The volume of the image artifact was determined by summing the number of voxels below 0.75 of the normalized image artifact. No analysis was done on the BFFE images because of the differences between the in-vitro and in-vivo artifacts. The inter-seed gap (in 1.5 mm increments) required for the two brachytherapy seed artifacts to appear completely separate was also determined. The artifacts were taken as separate when their respective 0.75 value borders did not overlap.

6.3 Results

6.3.1 Fast Spin Echo

Reconstructed coronal FSE images of a single seed oriented parallel to B_O (for both 1.5 T and 3.0 T magnetic fields) are shown in figure. 6-2 (a-f). The artifacts originate from two primary mechanisms. Firstly, the induced field gradients surrounding the seed will warp the planar nature of the slice selection, altering the image geometry. Secondly, the hydrogen protons within the distorted magnetic field will be spatially misrepresented in the frequency encoding process due to their altered resonance frequency. It can be seen that imaging with the smaller slice thickness (figure. 6-2 (a,d)) results in a 2 lobed artifact which is diminished as the slice thickness increases. It can also be seen that the artifacts are larger when imaged at the 3.0 T magnetic field strength (figure. 6-2 (d-f)). The volume of the artifact (as defined by the >0.75 background region) when the seed is positioned parallel to B_O was found to be 11.1 ± 0.4, 10.2 ± 0.6, and 9.6 ± 1.10 mm^3 for 1, 3 and 5 mm slice thicknesses respectively when imaged at 1.5 T and 17.3 ± 0.5, 17.6 ± 2.3 and 21.1 ± 2.5 mm^3 when imaged at 3.0 T (table 6-1). The maximum dimensions of the artifact increase in both the long and short axis of the artifact when imaged at higher field strength although most dimensions were within 1 standard deviation of each other (table 6-1). FSE images of a single seed oriented at 45° with respect to B_O in the coronal plane (for both 1.5 T and 3.0 T magnetic fields) are shown in figure. 6-3 (a-f). When imaged in this 45° orientation, the large effect of slice averaging can be seen. In this orientation, when imaged using 3 and 5 mm slice thicknesses, the artifact (as defined by the >0.75

background region) often appears as either two distinct lobes at either end or a single lobe at one end of the seed.

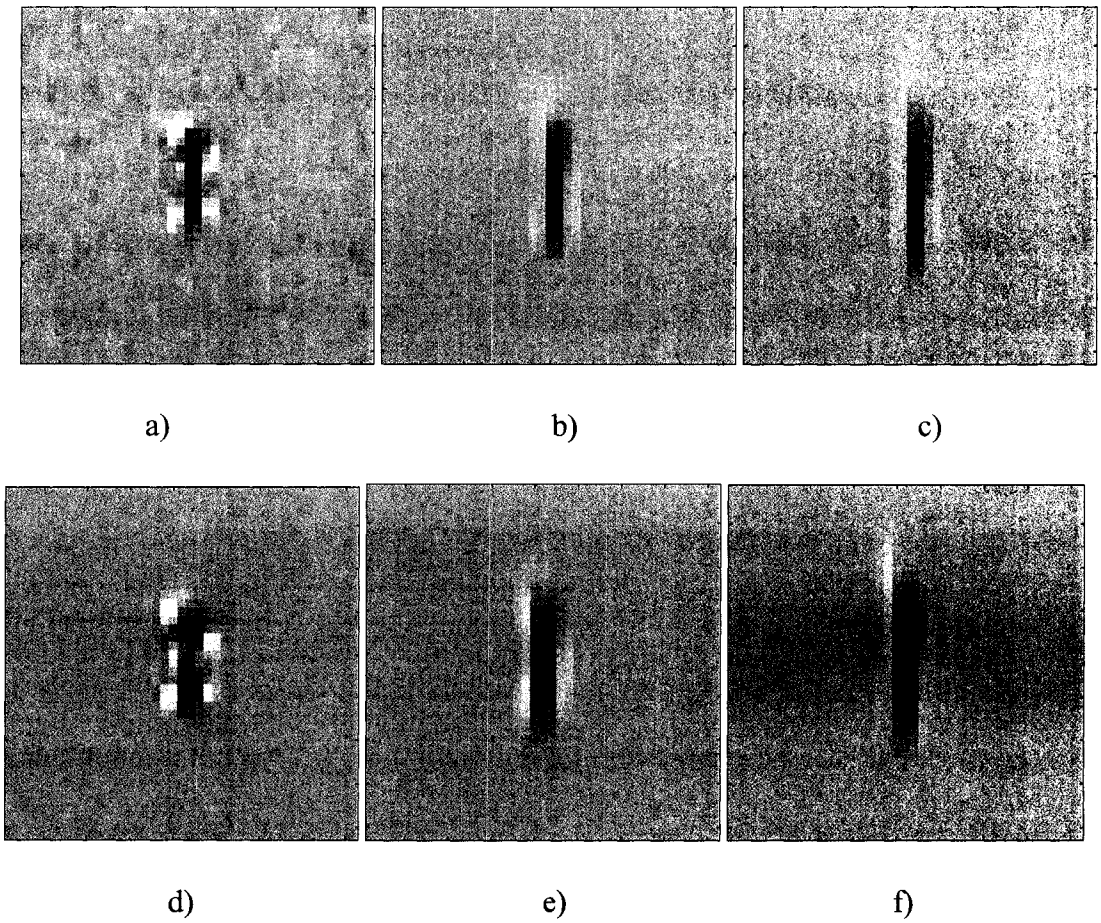

Figure. 6-2 FSE acquired images of a brachytherapy seed oriented parallel to B_O using 1 (a,d) , 3 (b,e) and 5 (c,f) mm slice thicknesses. The images were acquired at 1.5 T (a-c) and 3.0 T (d-f) field strengths. The field of view for the given images 25.6 X 25.6 mm^2.

Table. 6-1 Volume and the maximum length and width of FSE images with the seed oriented parallel to B_O.

	Volume (mm^3)	Maximum Length (mm)	Maximum Width (mm)
1.5 T (1 mm)	11.1 ± 0.4	6.86 ± 0.42	2.26 ± 0.30
3.0 T (1 mm)	17.3 ± 0.5	7.37 ± 0.32	2.28 ± 0.30
1.5 T (3 mm)	10.2 ± 0.6	7.73 ± 0.58	1.20 ± 0.05
3.0 T (3 mm)	17.6 ± 2.3	7.97 ± 0.46	1.71 ± 0.11
1.5 T (5 mm)	9.6 ± 1.1	8.32 ± 0.57	1.23 ± 0.03
3.0 T (5 mm)	21.1 ± 2.5	9.67 ± 0.51	1.70 ± 0.14

This effect is especially evident when examining the volume of the image artifact at 1.5 T: the artifact volume decreased from 15.5 ± 1.2 mm^3 to 3.9 ± 1.1 mm^3 when the slice thickness was increased from 1mm to 5 mm (table 6-2). The effect is reduced at 3.0 T where the volume of the artifact has greater consistency when imaged using the different slice thicknesses. At this 45° orientation the maximum dimensions of the artifacts increased in both length and width when imaged at the higher 3.0 T field strength. FSE images of two seeds aligned parallel to B_O are shown in figure. 6-4 (a-j). Two distinct image artifacts are visible when the seeds are separated by a 3 mm inter-seed gap when imaged at 1.5 T and 4.5 mm inter-seed gap when imaged at 3.0 T.

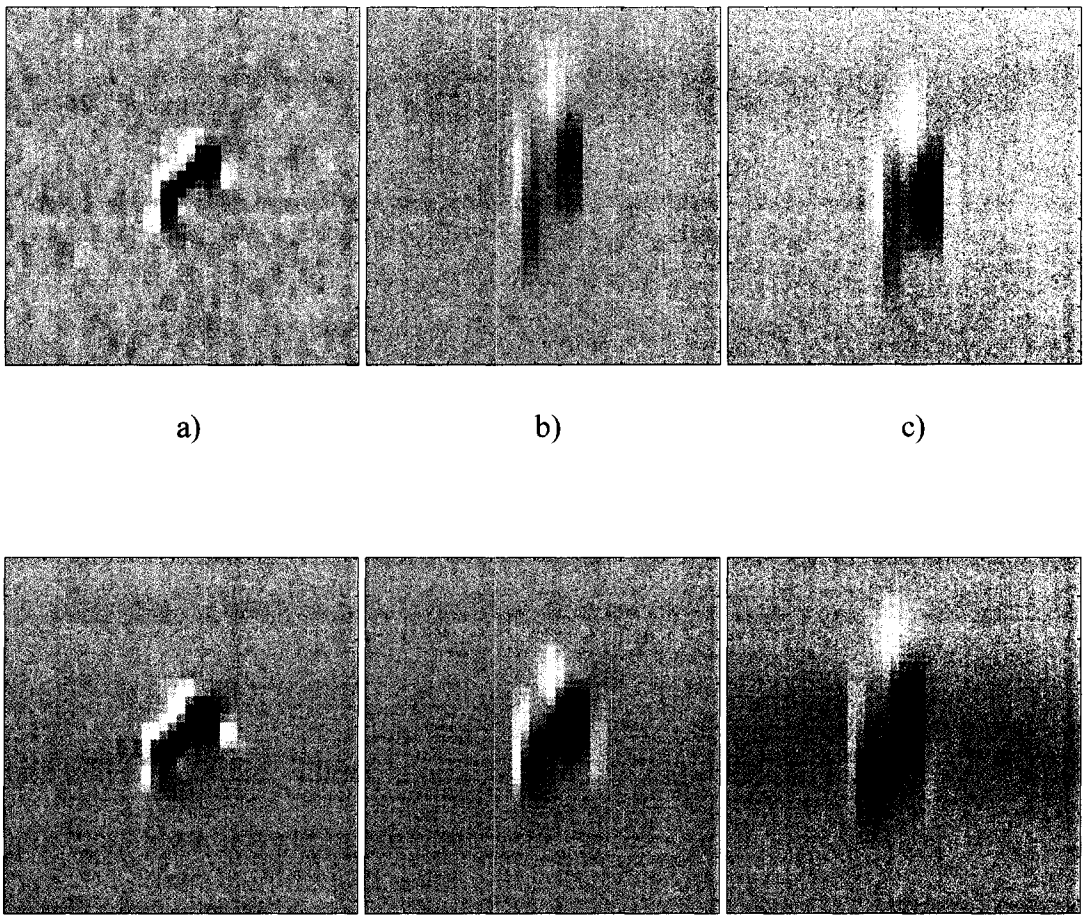

Figure. 6-3 FSE acquired images of a brachytherapy seed oriented 45° to B_O in the coronal plane using 1 mm (a,d) , 3 mm (b,e) and 5 mm (c,f) slice thicknesses. The images were acquired at 1.5 T (a-c) and 3.0 T (d-f) field strengths. The field of view for the given images 25.6 X 25.6 mm^2.

Table. 6-2 Volume and the maximum length and width of FSE images with the seed oriented at 45 ° to B_O in the coronal plane. N/A refers to measurements that could not be made because the artifact appeared as either two distinct lobes at either end or a single lobe at one end of the seed. The number within the brackets refer to the number of images (if less than 5) used to determine the mean maximum length and width.

	Volume (mm^3)	Maximum Length (mm)	Maximum Width (mm)
1.5 T (1 mm)	15.5 ± 1.2	6.35 ± 0.29	2.33 ± 0..35
3.0 T (1 mm)	24.1 ± 0.7	6.49 ± 0.23	3.04 ± 0.22
1.5 T (3 mm)	10.4 ± 0.7	N/A	N/A
3.0 T (3 mm)	23.0 ± 1.4	7.42 ± 0.17 (4)	3.46 ± 0.21(4)
1.5 T (5 mm)	3.9 ± 1.1	N/A	N/A
3.0 T (5 mm)	21.3 ± 3.2	7.48 ± 0.53 (3)	4.50 ± 0.26 (3)

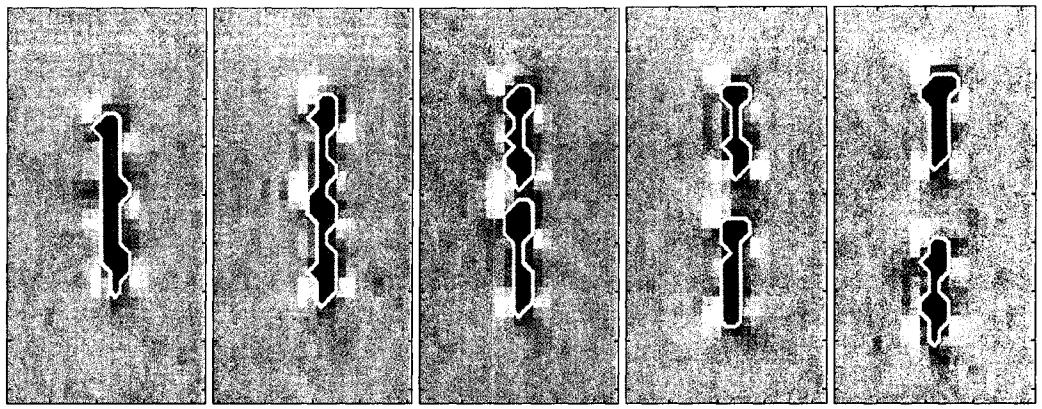

a) b) c) d) e)

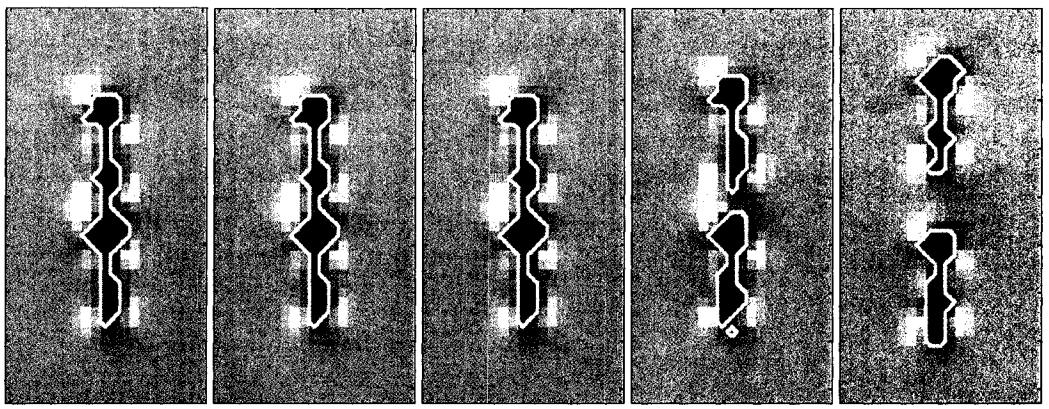

f) g) h) i) j)

Figure. 6-4 FSE acquired images of a 2 brachytherapy seed oriented parallel to B_O with. using 1 mm slice thickness. Inter seed gaps of 0 mm (a,f), 1.5 mm (b,g), 3 mm (c,h), 4.5 mm (d,i), and 6 mm (e,j) were used The images were acquired at 1.5 T (a-e) and 3.0 T (d-f) field strengths. The contours define where the normalized signal < 0.75.

6.3.2 Gradient Echo

GE images of a single seed oriented parallel to B_O acquired with a TE of 11 ms (for both 1.5 T and 3.0 T magnetic fields) are shown in figure. 6-5 (a-f). In addition to the two mechanisms responsible for the FSE image artifact, the GE artifact results from intra-voxel dephasing due to the magnetic gradients that exist close to the seed. The volume and the maximum width and length of the artifact (as defined by the >0.75 background region) when the seed is imaged parallel to B_O with a TE of 11 ms are given in table 6-3. The volume of these artifacts were found to be to be 61.1 ± 2.3, 112.5 ± 12.8, and 154.7 ± 28.1 mm^3 for 1, 3 and 5 mm slice thicknesses respectively when imaged at 1.5 T and 99.1 ± 1.3, 192.6 ± 30.0, and 295.8 ± 75.9 mm^3 when imaged at 3.0 T (table 6-3). Like the FSE images, the maximum dimensions in both the long and short axis of the image artifact increase when imaged at high field. GE images of a single seed oriented at 45° with respect to B_O in the coronal plane with a TE of 11 ms (for both 1.5 T and 3.0 T magnetic fields) are shown in figure. 6-6 (a-f). Due to the much larger size of the GE image artifact, the slice averaging problem that exists in the FSE sequence is not evident for the GE artifact. In this case, the volume of the image artifact is larger for the seeds imaged at 45° with respect to B_O than for those imaged parallel to B_O for both 1.5 and 3.0 (table. 6-4). For the two seed phantom, the artifacts appeared as two separate seeds at an inter-seed gap of 4.5 mm when imaged at 1.5 T and at 6.0 mm when imaged at 3.0 T (figure. 6-7). The larger artifacts of a brachytherapy seed when the TE is increased from TE of 11 ms to 22 ms are shown in figure. 6-8 (a-f). The volume and the maximum long and short dimensions of these artifacts are given in table 6-5.

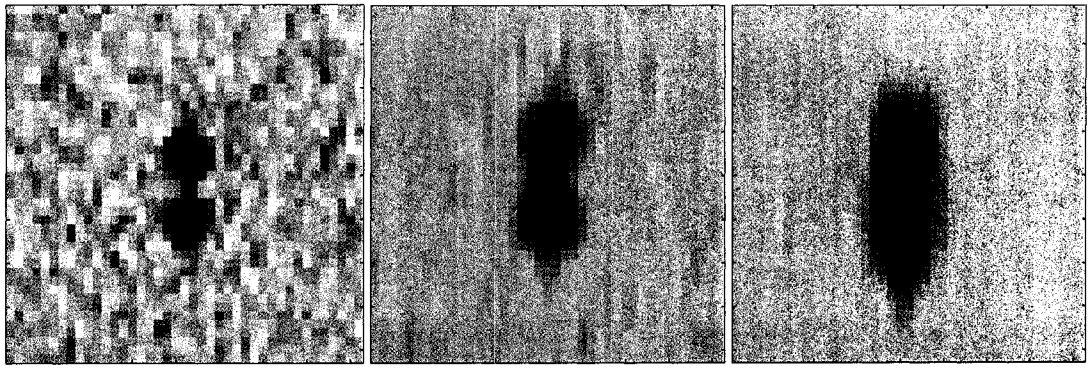

a) b) c)

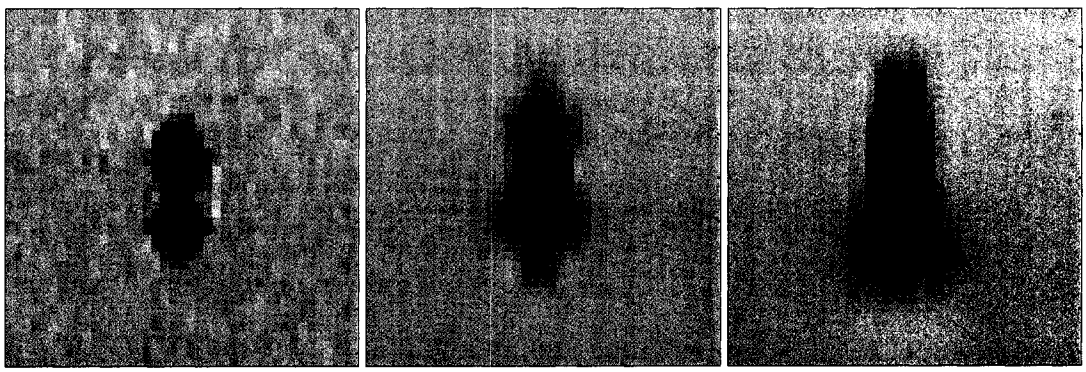

d) e) f)

Figure. 6-5 GE (TE=11 ms) acquired images of a brachytherapy seed oriented parallel to B_O using 1 (a,d) , 3 (b,e) and 5 (c,f) mm slice thicknesses. The images were acquired at 1.5 T (a-c) and 3.0 T (d-f) field strengths. The fields of view for the given images 25.6 X 25.6 mm^2.

The volumes of these artifacts were 100.2 ± 2.9, 201.0 ± 31.3, and 290.0 ± 68.9 mm^3 for 1, 3 and 5 mm slice thicknesses respectively when imaged at 1.5 T and 166.2 ± 2.2, 399.4 ± 27.1, and 642.72 ± 127.2 mm^3 respectively when imaged at 3.0 T (table 6-5). The volumes of the GE image artifacts, when imaged at 1.5 T with a 22 ms TE, closely resemble those when imaged at 3.0 T with an 11 ms TE. This indicates that the gradient of the local magnetic distortion surrounding the seed at 3.0 T is twice that at 1.5 T. Single seed images of the GE artifact when the seed is positioned at 45° with respect to B_O in the coronal plane with a TE of 22 ms (for both 1.5 T and 3.0 T magnetic fields) are shown in figure. 6-9 (a-f). The volumes and maximum long and short dimensions are given in table table. 6-6 and show an increase in both dimensions when imaged at higher field. For the two seed phantom imaged using a GE sequence and 22 ms TE, two distinct image artifacts are visible when the seeds are separated by a 6 mm inter-seed gap for both 1.5 T and at 3.0 T field strengths.(figure. 6-10). Finally GE acquired coronal images of a brachytherapy seed oriented parallel to B_O using 1 mm^2 resolution for a range of TEs are shown in figure. 6-11. The images demonstrate the progression of image artifact size as TE is increased.

Table. 6-3 Volume and the maximum length and width of GE (TE = 11 ms) images with the seed oriented parallel to B_O

	Volume (mm^3)	Maximum Length (mm)	Maximum Width (mm)
1.5 T (1 mm)	61.1± 2.3	9.40 ± 0.46	3.73 ± 0.05
3.0 T (1 mm)	99.1 ± 1.3	10.29 ± 0.34	4.51 ± 0.29
1.5 T (3 mm)	112.5 ± 12.8	12.69 ± 0.24	4.20 ± 0.24
3.0 T (3 mm)	192.6 ± 30.0	13.22 ± 0.53	5.60 ± 0.66
1.5 T (5 mm)	154.7 ± 28.1	14.18 ± 0.82	4.26 ± 0.53
3.0 T (5 mm)	295.8 ± 75.9	15.00 ± 0.53	6.18 ± 1.26

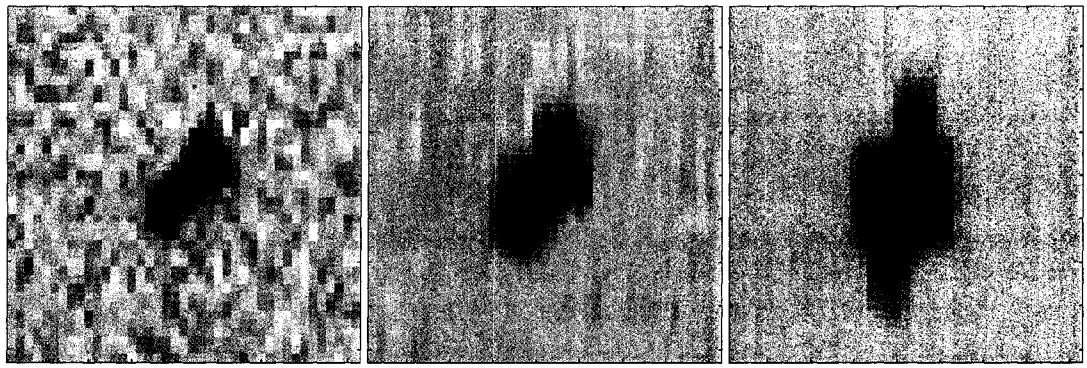

a) b) c)

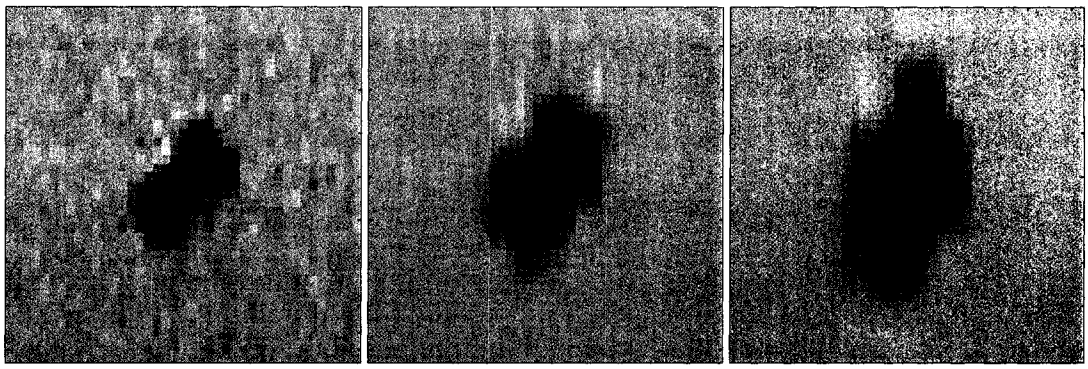

d) e) f)

Figure. 6-6 GE (TE=11ms) acquired images of a brachytherapy seed oriented 45° to B_O in the coronal plane using 1 mm (a,d) , 3 mm (b,e) and 5 mm (c,f) slice thicknesses. The images were acquired at 1.5 T (a-c) and 3.0 T (d-f) field strengths. The fields of view for the given images 25.6 X 25.6 mm^2.

Table. 6-4 Volume and the maximum length and width of GE (TE = 11 ms) images with the seed oriented at 45° to B_O in the coronal plane.

	Volume (mm^3)	Maximum Length (mm)	Maximum Width (mm)
1.5 T (1 mm)	82.4 ± 1.7	8.18 ± 0.25	4.41 ± 0.63
3.0 T (1 mm)	133.1 ± 2.8	8.78 ± 0.27	5.57 ± 0.24
1.5 T (3 mm)	161.9 ± 1.7	9.59 ± 0.24	6.16 ± 0.64
3.0 T (3 mm)	265.5 ± 5.8	10.24 ± 0.22	7.45 ± 0.36
1.5 T (5 mm)	225.7 ± 10.7	10.60 ± 1.16	6.93 ± 0.93
3.0 T (5 mm)	384.7 ± 31.7	12.21 ± 0.89	8.22 ± 0.66

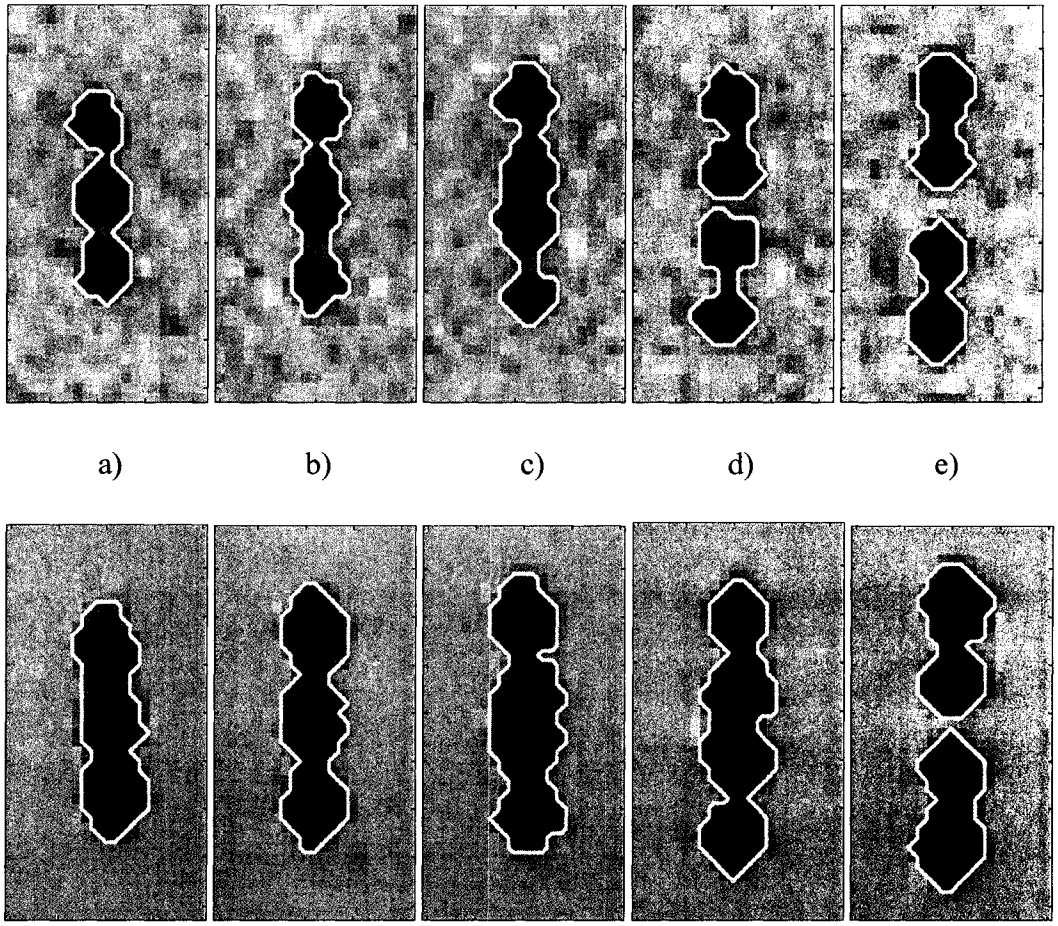

Figure. 6-7 GE (TE = 11ms) acquired images of a 2 brachytherapy seeds oriented parallel to B_O with. using 1 mm slice thickness. Inter seed gaps of 0 mm (a,f), 1.5 mm (b,g), 3 mm (c,h), 4.5 mm (d,i), and 6 mm (e,j) were used The images were acquired at 1.5 T (a-e) and 3.0 T (d-f)

Table. 6-5 Volume and the maximum length and width of GE (TE = 22 ms) images with the seed oriented parallel to B_O

	Volume (mm^3)	Maximum Length (mm)	Maximum Width (mm)
1.5 T (1 mm)	100 ± 2.9	10.70 ± 0.47	4.71 ± 0.35
3.0 T (1 mm)	166.2 ± 2.2	11.51 ± 0.37	5.23 ± 0.29
1.5 T (3 mm)	201.0 ± 31.3	13.55 ± 0.55	5.37 ± 0.41
3.0 T (3 mm)	399.4 ± 27.1	14.23 ± 0.56	8.18 ± 0.71
1.5 T (5 mm)	290.0 ± 68.9	15.97 ± 0.74	5.89 ± 0.80
3.0 T (5 mm)	642.72 ± 127.2	16.21 ± 0.54	10.47 ± 1.2

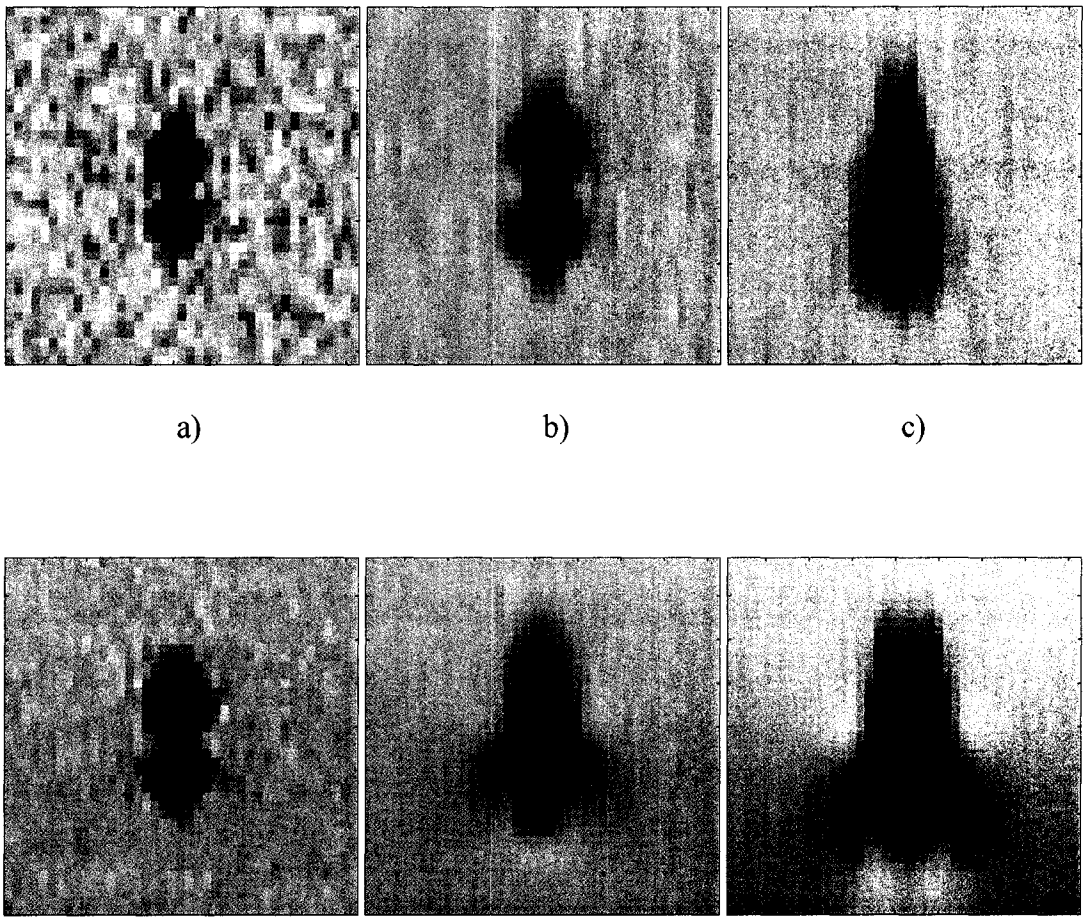

Figure. 6-8. GE (TE=22 ms) acquired images of a brachytherapy seed oriented parallel to B_O using 1 (a,d) , 3 (b,e) and 5 (c,f) mm slice thicknesses. The images were acquired at 1.5 T (a-c) and 3.0 T (d-f) field strengths. The field of view for the given images 25.6 X 25.6 mm^2.

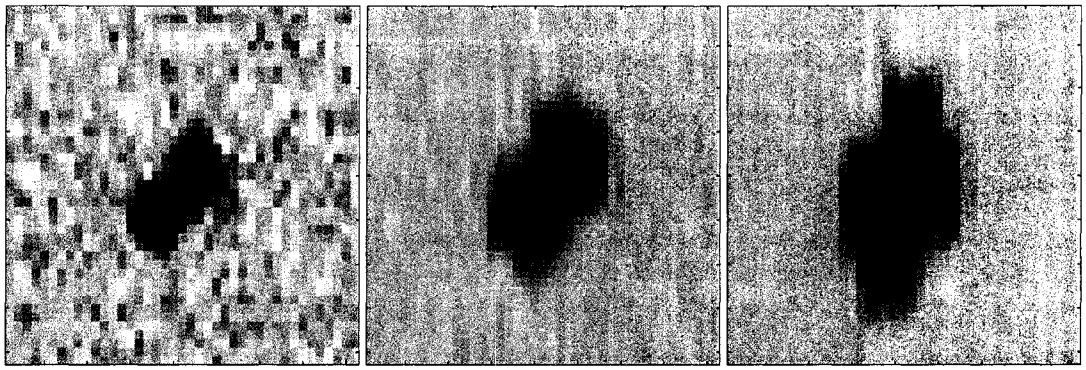

a) b) c)

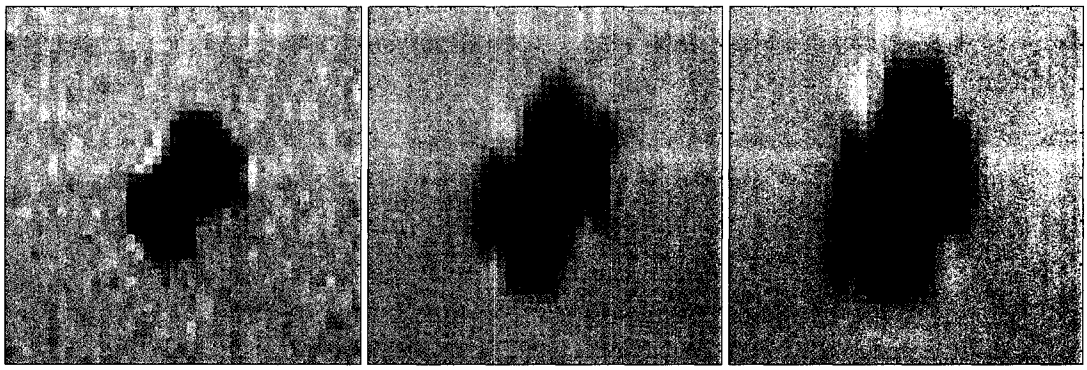

d) e) f)

Figure. 6-9. GE (TE=22ms) acquired images of a brachytherapy seed oriented 45° to B_O in the coronal plane using 1 mm (a,d) , 3 mm (b,e) and 5 mm (c,f) slice thicknesses. The images were acquired at 1.5 T (a-c) and 3.0 T (d-f) field strengths. The field of view for the given images 25.6 X 25.6 mm^2.

Table. 6-6 Volume and the maximum length and width of GE (TE = 22 ms) images with the seed oriented at 45° to B_O in the coronal plane.

	Volume (mm^3)	Maximum Length (mm)	Maximum Width (mm)
1.5 T (1 mm)	138.6 ± 4.3	9.36 ± 1.23	5.45 ± 0.29
3.0 T (1 mm)	220.6 ± 2.4	9.79 ± 0.23	6.37 ± 0.37
1.5 T (3 mm)	279.4 ± 8.50	11.03 ± 0.55	7.70 ± 0.21
3.0 T (3 mm)	462.9 ± 16.3	11.85 ± 0.50	9.51 ± 0.65
1.5 T (5 mm)	397.6 ± 34.0	12.96 ± 0.33	9.31 ± 0.78
3.0 T (5 mm)	634.5 ± 70.5	14.10 ± 0.70	11.22 ± 0.40

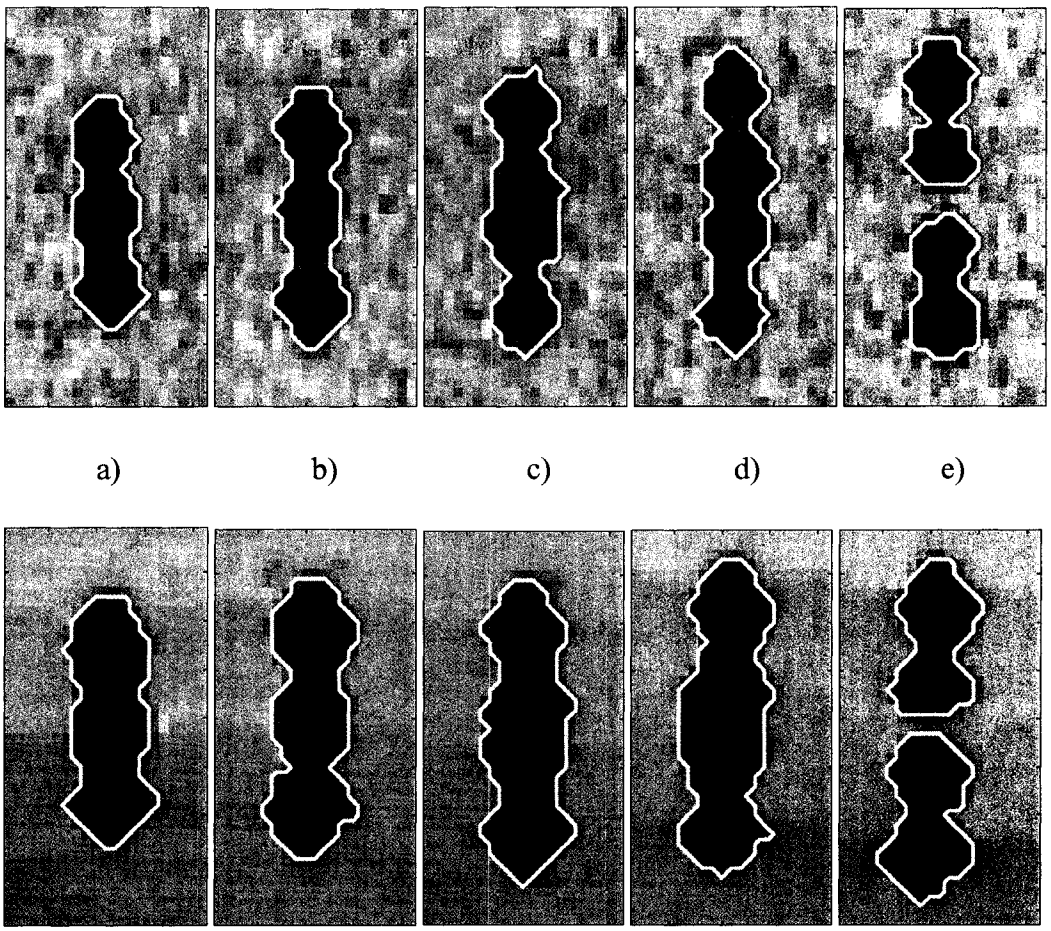

Figure. 6-10. GE (TE = 22 ms) acquired images of 2 brachytherapy seeds oriented parallel to B_O with. using 1 mm slice thickness. Inter seed gaps of 0 mm (a,f), 1.5 mm (b,g), 3 mm (c,h), 4.5 mm (d,i), and mm 6 (e,j) were used The images were acquired at 1.5 T (a-e) and 3.0 T (d-f).

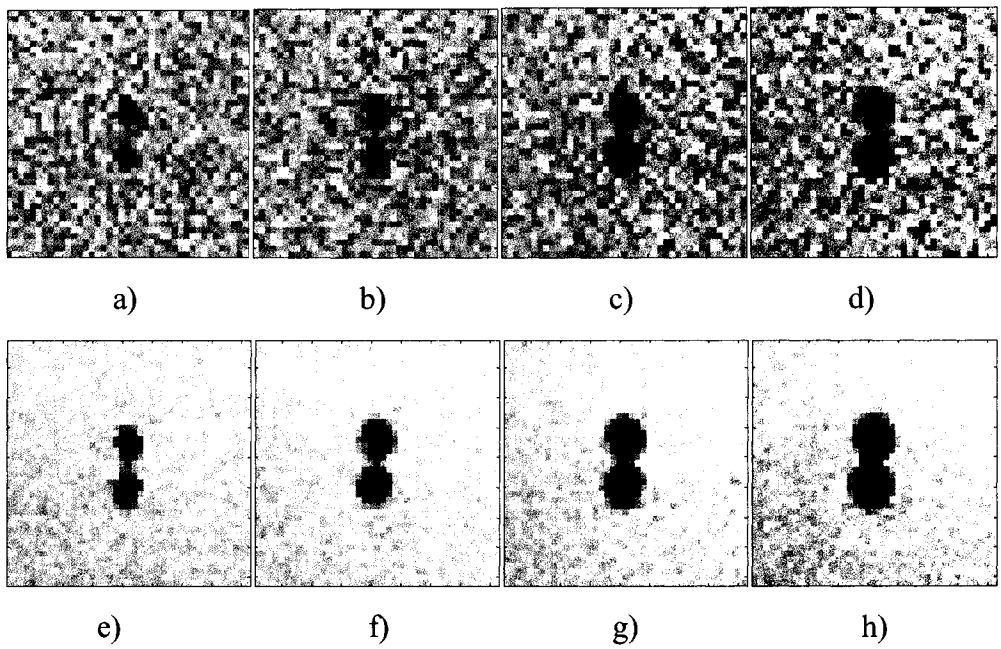

Figure. 6-11. GE acquired coronal images of a brachytherapy seed oriented parallel to B_O using 1 mm^2 resolution at TEs of 5.5 ms (a,e), 11 ms (b,f), 16.5 ms (c,g) and 22 ms (d,h). The images were acquired at 1.5 T (a-d) and 3.0 T (e-h).

6.3.3 Balanced Fast Field Echo

BFFE images of a single seed oriented parallel to B_O acquired with receiver offsets of 0, 25, 50, and 75 Hz (for the 3.0 T magnetic field) are shown in figure. 6-12 (a-d). In addition to the two mechanisms responsible for the FSE image artifact, the BFFE artifact results primarily from off-resonance effects. These off resonance effects, which are typically seen as a banding patterns in an image (figure. 6-12(a)), result from a variation of precession frequencies within close proximity of a seed and the resultant effect of the time evolution of the magnetization throughout the imaging sequence. Because these off resonance effects will depend on the local magnetic shim of the prostate it may be expected to vary across the image anatomy producing images such as those shown in figure. 6-12 (a-d). As the BFFE artifacts are also dependent on

the T1 and T2 time constants of the medium in which the seed is surrounded, it should also be expected that the frequency of the banding artifacts produced from in-vivo images will differ from the images presented in figure. 6-12 (a-d). Figure. 6-12(e) was acquired by using 4 averages in which the offset frequency was adjusted during each average and then data is combined in an attempt to minimize the banding pattern.[8] Though this technique will reduce the banding artifact, the duration of the scan will subsequently increase.

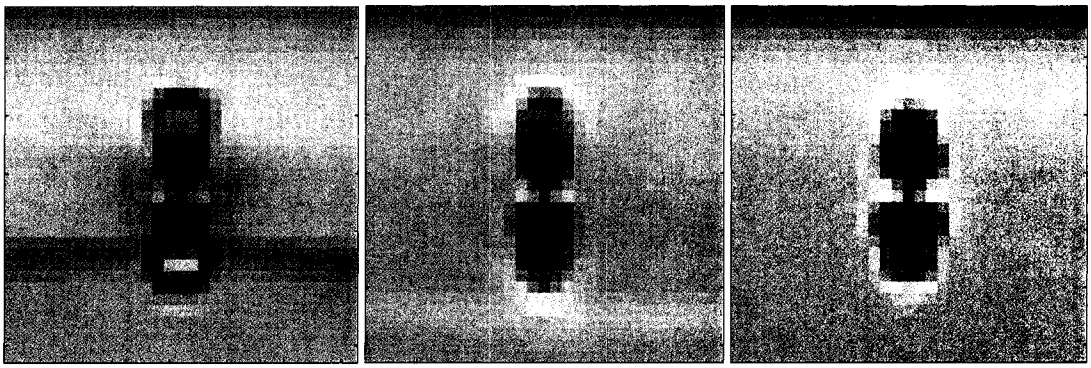

a) b) c)

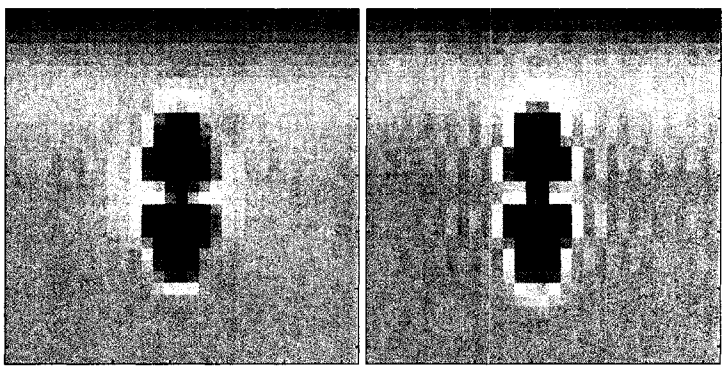

d) e)

Figure. 6-12 BFFE images of a single seed oriented parallel to B_O acquired with receiver offsets of 0, 25, 50, and 75 Hz (for the 3.0 T magnetic field) are shown in a-d and with offset averaging in e.

6.4 Conclusion

Although MR images provide excellent anatomical delineation, post-implant evaluation using magnetic resonance imaging (MRI) at 1.5T has met with limited success due to the large uncertainty associated in seed position. Clinical scanners at 3.0 T, with their associated increase in signal to noise ratio (SNR), allow for increased resolution which may resolve the issue of seed location uncertainty although the practicality of this should be investigated in-vivo. The FSE-and GE-acquired artifacts were both found to be larger when imaged at higher field. For the GE-acquired images the effect of imaging at 3.0 T was equivalent to doubling the TE. The size of the GE-acquired artifact at the 3.0 T field will make this sequence unsuitable for distinguishing seeds in close proximity. For the FSE sequence which have been the primary imaging sequence used for seed identification the length and width of the image artifact only increased by roughly 0.5 mm at maximum when 1 and 3 mm slice thicknesses were used. This larger 3.0 T FSE artifact may in fact aid in seed detection when the seed is not parallel to B_O (which is the most likely case) and thus plagued by slice averaging affects when employing thicker slice thicknesses such as 3 and 5 mm. The BFFE sequence may also provide a viable option especially if using offset averaging although for this sequence an in-vivo analysis is also recommended. Finally it should be noted that further investigation is required for both the effects of SAR as well as direct RF coupling which may occur for longer seed trains, [9,10]

References

[1] D.F. Dubois, B.R. Prestidge, L.A. Hotchkiss, W.S.Bice Jr., and J.J. Prete, "Source localization following permanent transperineal prostate interstitial brachytherapy using magnetic resonance imaging," Int. J. Radiat. Oncol. Biol. Phys. **39**, 1037-1041 (1997).

[2] F.V. Coakley, H.Hricak, A.E Wefer, J.L Speight, J. Kurhanewicz, M.Roach III, "Brachytherapy for prostate cancer: Endorectal MR imaging of local treatment related changes," Radiology **219**, 817-821 (2001).

[3] D.F. Dubois, W.S. Bice Jr. and B.R. Prestige, "CT and MRI derived source localization error in a custom prostate phantom using automated image coregistration," Med. Phys. **28**, 2280-2284 (2001).

[4] J.F. Schenck, "Review article: Role of magnetic susceptivility in MRI," Med. Phys.**23**, 815-850 (1996).

[5] J. Hennig, A. Nauerth and H. Friedburg, "RARE imaging: a fast imaging method for clinical MR," Magn. Reson. Med. **3**, 823-833 (1986).

[6] E.M. Haacke, P.A. Weilopolski and J.A. Tkach. "A comprehensive review of short Tr, fast magnetic resonance imaging techniques" Rev. Magn. Reson, Med., **3** (1991)

[7] A. Oppelt, R. Graumann, H. Barfuss, H,. Fisher, W. Hertl and W. Schjor " FISP: A new fast MRI sequence." Electromedica, **3** (1986)

[8] N.K. Bangerter, B.A. Hargreaves, S.S. Vasanawala, J.M. Pauly, G.E. Gold, D.G. Nishimura. "Analysis of multiple acquisition SSFP." Magn. Reson. Med. **51** 1038-1047 (2004)

[9] H. Graf, U.A. Lauer, A. Berger, F. Schick "RF artifacts caused by metallic implants or instruments which get more prominent at 3 T: and in vitro study" Magn. Reson. Imaging. **23** 493-499 (2005)

[10] U.A. Lauer, H. Graf, A. Berger, C.D. Claussen and F. Schick. "Radio frequency versus susceptibility effects of small conductive implants -- a systematic MRI study on aneurysm clips at 1.5 and 3 T." Magn. Reson. Imaging. **23** 563-569 (2005)

Chapter 7 Conclusions

7.1 TG-51 Calibration for Helical TomoTherapy™

A TG-51 calibration for HT was developed and implemented on the HT unit at our center. The primary motivation for the calibration was the inability of HT to meet the field size and SSD required for the k_Q lookup table in the TG-51 protocol. In addition, the absence of a flattening filter within the HT unit also makes the beam different in terms of both beam flatness and energy spectrum from that of conventional medical linear accelerators. Throughout the range of mean incident electron energies for which calculations were done, the k_Q corrections increase from 0.06% to 0.16%. The corrections are small due to the fact that k_Q versus $\%dd(10)_x$ varies slowly in this energy region. This conversion of the $\%dd(10)_{x[HT\ Ref]}$ values is expected to hold roughly for other chambers although some attention should be given to the central electrode correction factor and volume averaging affects which will affect chambers with aluminum central electrodes and larger volume chambers respectively.

7.2 Delivery Quality Assurance for 10 HT Patients

When the A1SL was used in conjunction with EDR2 film to perform DQA of 10 HT patients it was found that for un-normalized, film mark registered dose maps (DS#1) the agreement was deemed acceptable using the 2 mm & 2% criteria with 69.8±17.2% of the dose pixels passing. The agreement for the 4 mm & 3% and 3 mm & 5% criteria was 92.6±9% and 93.4±8.5% of the dose pixels passed, respectively. When using dose maps which have been normalized and manually matched (DS#2), the agreement was 91.2±5.6% of the dose pixels agreeing to within 2 mm & 2% and

99.2±1.43%, and 99.5±0.8% agreeing for the 4 mm & 3% and 3 mm & 5% criteria, respectively. We have at our center established 3 tolerances for a successful treatment verification of an average treatment plan. The tolerance for the film mark registered and un-normalized dose map is 80% of the dose pixels passing the 3 mm & 5% gamma criteria. This test allows us to identify major discrepancies between calculation and measurement including both positioning and film measurement errors. We feel that the positioning error in the delivery verification gives a good indication of the limits of positioning accuracy during the treatment itself, and thus should remain visible in the treatment verification. The tolerance for the manually registered and normalized dose map is 80% of the dose pixels passing the 2 mm & 2% gamma criteria. This test assumes that the error in the first test is due primarily to experimental error and the limitations of film as a dosimeter. The tolerance for the high dose point dose measurement is 2% and provides a more robust measure of the absolute dose difference between the calculation and delivered dose. The combination of these 3 tests provides a good method for identifying errant treatment plans. No acceptability criteria for the low dose point measurement or the critical structure point measurement has been specified as we feel that the interpretation of these measurements should be made on a patient-specific basis. Low dose regions are of particular interest if the potential exists for the patient to be retreated. The calculation of the patient treatment plan on the cheese phantom sometimes makes it difficult to accurately position the phantom for a critical structure measurement, particularly if the structure is small. This difficulty combined with the fact that these regions often contain or lie in close proximity to steep dose gradients suggest that setting a strict

criterion for plan rejection could prove to be overly conservative. In some situations (i.e., patients being retreated) strict criteria on critical structure low dose regions may be more important than our high dose region criteria.

7.3 Future Work in Regards to the Dosimetry of HT

Future work in the area may involve expanding the 2 dimensional comparison of measured and calculated doses of the HT plan to a full 3 dimensional comparison. This could be done using a polymer gel or something similar to the portal imaging devices currently used for IMRT delivery verification at our center. Using the full 3 dimensional data sets would give a complete comparison of the treatment plan and may locate errors that do not appear in 2 dimensional samplings of the 3 dimensional plans. Another area which deserves investigation is in understanding how errors which appear in phantom between calculated and measured doses manifest back within the original patient specific geometry. Finally, movement towards a delivery verification based tumor and tissue responses should also be investigated as in the end simultaneous realization of appropriate tissue and tumor response are the end goal of treatment.

7.4 Characterization of the Susceptibility Artifact Around a Prostate Brachytherapy seed in MRI

Although MR images provide excellent anatomical delineation, post-implant evaluation using magnetic resonance imaging (MRI) at 1.5 T has met with limited success due to the large uncertainty associated in seed position. The characteristic

distortions for a typical brachytherapy seed within a clinical 1.5 T MR imager were measured experimentally and found to show significant deviations from the physical seed geometry. The distortion patterns were found to vary significantly with both the orientation to the main magnetic field, as well as with the read encode direction. Simulations of the images based on the magnetic field induced by the brachytherapy seed materials were successfully performed allowing for accurate localization of the seed within the distortion pattern. These distortions simulated will be present in all images acquired using a unidirectional linear read encode trajectory. These distortion patterns proved to be sufficiently distinct to allow for successful automatic localization in two dimensions using the normalized cross correlation method at resolutions down to 1 mm.

7.5 Magnetic Resonance Imaging of Prostate Brachytherapy Seeds at 3.0 T an In Vitro Study

Clinical scanners at 3.0 T, with their associated increase in signal to noise ratio (SNR), allow for increased resolution which may resolve the issue of seed location uncertainty. For this reason some of the effects of background field on the produced images were investigated in-vitro. FSE and GE acquired artifacts were both found to be larger when imaged at higher field. For the GE acquired images the effect of imaging at 3.0 T was equivalent to doubling the TE. The size of the GE acquired artifact at the 3.0 T field will make this sequence unsuitable for distinguishing seeds in close proximity. For the FSE sequence which have been the primary imaging sequence used for seed identification the length and width of the image artifact only

increased by roughly 0.5 mm at maximum when 1 and 3 mm slice thicknesses were used. This larger 3.0 T FSE artifact may in fact aid in seed detection when the seed is not parallel to B_o (which is the most likely case) and thus plagued by slice averaging affects when employing thicker slice thicknesses such as 3 and 5 mm. The BFFE sequence may also provide a viable option especially if using offset averaging.

7.6 Future Work in Regards to Implant Prostate Evaluation using MRI

Future work for post implant prostate evaluation involves the assessment of the use of both the image prediction algorithm and the 3.0 T magnet in-vivo. Before in-vivo assessment of the use of high field magnets for prostate seed localization takes place, further investigation is required for both the effects of SAR as well as direct RF coupling which may occur for longer seed trains. Finally the highly predictable nature of these distortion patterns offers the hope that perhaps an automatic localization algorithm can be produced that can pinpoint the location of implanted seeds from a single three dimensional MR scan providing both accurate anatomical data in a addition to accurate seed positions within the anatomy.

Appendix A: AAPM Task-Group - 51 (TG-51)

A 1 Introduction

The AAPM's TG-51 protocol[1] for clinical reference dosimetry of both photon and electron beams was introduced in 1999. The TG-51 protocol is meant to provide an accurate method of calibrating photon and electron beams for radiation therapy and has widely replaced the previously used method of performing reference dosimetry in North America as described in the TG-21 protocol.[2] The method of photon beam reference dosimetry given in the TG-51 protocol is based on the absorbed dose calibration factor of an ion chamber in a ^{60}Co reference beam at a standards lab. This discussion will focus on the part of TG-51 related to photon beam dosimetry because it is of primary importance to the work done in the first part of this thesis. For photon dosimetry, the TG-51 protocol is valid for beam energies between 1.25 MeV and 50 MV bremsstrahlung spectra.[1] The TG-51 protocol offers several advantages over the method described in the TG-21 protocol. The first and primary advantage of TG-51 over TG-21 is that TG-51 is based on the absorbed dose to water and thus does not rely on an air-kerma-to-absorbed-dose-to-water conversion factors avoiding the the uncertainty associated with the calculation of these factors.[1,3] Secondly, TG-51 uses the more accurately calculated restricted mass collision stopping powers in the ICRU report 37 [4] as compared to TG-21 which uses mean restricted mass collision stopping powers from ICRU report 35.[5] More accurate stopping power values changes the reference dose from the photon beam by as much as 1.3%.[3] Thirdly, TG-21 does not make any corrections for the presence of metallic, primarily aluminum, central electrodes which exist in many ion chambers used today. The presence of 1 mm

aluminum central electrode can affect an increase in ion chamber response of beween 0.43% and 0.75% for photon beam energies between 24 MV and 1.25 MeV respectively.[6] It should be noted that the effects of these three shortcomings on the reference dosimety tend to cancel each other out. In addition to improved accuracy over TG-21, TG-51 is conceptually simpler than TG-21 as it does not involve air kerma. Implementation of the TG-51 dosimetry protocol results in an increase in reference dose of between 0.1 and 0.8% depending on the ion chamber used as compared with results obtained using the methods described in the TG-21 protocol.[7,8]

A 2 TG-51 Formalism for Photon Beams

According to TG-51 the absorbed dose to water is given by:[1]

$$D_w^Q = Mk_Q N_{D,w}^{^{60}Co} \qquad 1$$

where D_w^Q is the absorbed dose to water from a beam of arbitrary quality Q, at the point of measurement in water, M is the fully corrected electrometer reading. The electrometer is connected to an ion chamber with a ^{60}Co beam absorbed dose to water calibration coefficient $N_{D,w}^{^{60}Co}$. Finally k_Q is the beam spectrum quality conversion factor.

A 3 The Fully Corrected Ion Chamber Reading, M

The fully corrected ion chamber reading is calculated as follows.[1]

$$M = M_{raw} P_{T,P} P_{ion} P_{pol} P_{elec} \qquad 2$$

where M_{raw} is the raw electrometer reading, $P_{T,P}$ is the correction for altered air-density in the chamber due to the ambient temperature and pressure, P_{ion} is the correction factor accounting for undetected charge resulting from ionic recombination, P_{pol} is the correction for chamber polarity effects, and P_{elec} is the electrometer calibration factor. M_{raw} has the units of nC and the correction factors are unitless.

A 4 Electrometer Correction Factors

A 4.1 $P_{T,P}$

The total charge generated within an irradiated ion chamber is dependent on both the dose rate as well as the mass of air within the ion chamber. For vented ion chambers, the mass of air inside an ion chamber is affected by both changes in temperature and pressure which consequently means the electrometer reading is also dependent on temperature and pressure. Ion chambers are calibrated under the specific temperature and pressure conditions of 295.2 Kelvin (K) and 101.33 kilopascals (kPa), respectively.[9] The temperature and pressure conditions during day to day measurements can fluctuate significantly. To remove the uncertainty in the mass of air in the ion chamber from the electrometer reading, the reading is normalized back to the ion chamber calibration conditions. This is done by taking a ratio of the mass of air

during the calibration of $N_{D,w}^{^{60}Co}$ over the mass of air during the clinical measurement according to the ideal gas law which yields

$$P_{T,P} = \frac{101.33}{P} \times \frac{T}{295.2}, \qquad 3$$

where P and T are the atmospheric pressure in kPa and temperature in K at the time of measurement, respectively. In practice, it is important to ensure that time is given for the chamber to reach thermal equilibrium with its surroundings (i.e. the water within the tank).

A 4.2 P_{ion}

TG-51 assumes 100% charge collection efficiency of the ion pairs created. P_{ion} thus corrects for this "real world" lack of efficiency that results from the ionic recombination within the sensitive volume of the chamber.[10] As P_{ion} is dependent on both pulse rate for a constant dose rate and dose rate per pulse, it must be recalculated in the case that either is changed.[9] For pulsed beams P_{ion} is calculated according to[1]

$$P_{pol} = \frac{1 - V_H/V_L}{M_{raw}^H/M_{raw}^L - V_H/V_L} \qquad 4$$

where V_H is the voltage at which the M^H_{raw} reading is taken and V_L is the voltage at which M^L_{raw} is taken. A typical value for this correction factor is 1.003

A 4.3 P_{pol}

P_{pol} corrects for the dependence of the ion chamber response on the polarity of applied voltage. This dependence varies with a number of factors such as beam quality and cable position.[9] P_{pol} is calculated according to:[1]

$$P_{pol} = \frac{M^+_{raw} - M^-_{raw}}{2M_{raw}} \qquad 5$$

where M^+_{raw} is the electrometer reading when positive charge is collected and M^-_{raw} is the reading when negative charge is collected. M_{raw} is the electrometer reading of the same sign as used during the determination of $N^{^{60}Co}_{D,w}$. In essence, P_{pol} corrects M_{raw} to the mean value of M^+_{raw} and M^-_{raw}. A typical value for this correction factor is 0.999.

A 4.4 P_{elec}

The electrometer calibration factor is used to convert the electrometer reading to true charge in coulombs (C). If the ion chamber and the electrometer are calibrated together as a unit as is the common practice in Canada, P_{elec} is equal to 1.

A 5 k_Q

The factor k_Q converts the absorbed dose to water calibration coefficient for the reference ^{60}Co beam to the absorbed dose to water calibration coefficient for a beam of arbitrary quality Q. Thus

$$N_{D,w}^{Q} = k_Q N_{D,w}^{^{60}Co}. \qquad 6$$

Rearranging this equation we get

$$k_Q = \frac{N_{D,w}^{Q}}{N_{D,w}^{^{60}Co}}. \qquad 7$$

The parameter, k_Q is therefore a ratio of absorbed dose to water calibration coefficients. To expedite the calculation of k_Q, we shall determine the solution of the denominator of Eq. (7) and assume a symmetrical argument for the numerator. As the dose to water calibration coefficient converts the corrected electrometer reading to dose it can (for a ^{60}Co beam) be defined as

$$N_{D,w}^{^{60}Co} = \frac{D_w^{^{60}Co}}{M} \quad . \qquad 8$$

Using the Spencer-Attix theory[11] with the P_{repl}, P_{cel} and P_{wall} correction factors (discussed below), we replace the dose to water in Eq. (8) with the dose to air as follows:

$$N_{D,w}^{^{60}Co} = \frac{D_{air}^{^{60}Co}\left(\bar{L}/\rho\right)_{air}^{water} P_{repl}P_{cel}P_{wall}}{M} \qquad 9$$

where $\left(\bar{L}/\rho\right)_{air}^{water}$ is the water-to-air mean restricted mass collision stopping power ration (spr). The dose to air is measured using an ion chamber and is described by

$$D_{air}^{^{60}Co} = \left(\frac{\bar{W}}{e}\right)\frac{M}{m_{air}}K_h, \qquad 10$$

where $\left(\bar{W}/e\right)$ is the mean excitation energy per ion pair formed in dry air and has a value of 33.97 J/C.[9] Furthermore m_{air} is the mass of air in the ion chamber and K_h is a humidity correction factor. K_h accounts for changes in humidity that cause subsequent changes in the water-to-air spr, m_{air} and $\left(\bar{W}/e\right)$. K_h is equal to 0.997 for a relative humidity between 15% and 80%.[9] Substituting Eq. (10) into Eq. (9) leads to

$$N_{D,w}^{^{60}Co} = \left(\frac{\bar{W}}{e}\right)\frac{K_h}{m_{air}}\left(\bar{L}/\rho\right)_{air}^{water} P_{repl}P_{cel}P_{wall}. \qquad 11$$

k_Q is now determined by applying the same arguments in determining $N_{D,w}^{Q}$ as were used in the determination of $N_{D,w}^{^{60}Co}$ and substituting both into Eq. (7). The result is the standard definition of k_Q as stated in the TG-51 protocol:

$$k_Q = \frac{\left[\left(\bar{L}/\rho\right)_{air}^{water} P_{repl} P_{cel} P_{wall}\right]_Q}{\left[\left(\bar{L}/\rho\right)_{air}^{water} P_{repl} P_{cel} P_{wall}\right]_{^{60}Co}} . \qquad 12$$

A 6 Correction Factors in k_Q Determination

A 6.1 P_{repl}

P_{repl} is the cavity replacement correction factor and it corrects for changes to the electron spectrum that arise from placement of the ion chamber cavity in the medium. P_{repl} consists of gradient and fluence correction factors:

$$P_{repl} = P_{fl} P_{gr} \qquad 13$$

P_{fl} accounts for two primary effects. The first effect is due to the increase in the number of electrons passing through the air cavity as fewer electrons are scattered outwards compared to those scattered in from the medium due the lower scatter probability within the cavity . This results in increased electron fluence within the cavity. The second effect is due to the reduced mean path length of electrons within the cavity resulting from the lower scatter probability within the cavity. The result of this is decreased electron fluence within the cavity. P_{fl} corrections are not required for photon beam measurements made in conditions of transient charged particle equilibrium. According to Fano's theorem[11], under conditions of charged particle equilibrium the electron spectrum is independent of material density[11] and thus is not

affected by the presence of an air cavity. Thus P_{fl} is not required in photon beam measurement beyond the depth of maximum dose (d_{max}).

Another effect of placing a finite size air-cavity in the medium is to cause an effective up stream shift in the point of measurement. This is due to the decreased attenuation and buildup in the cavity as compared to the medium.[9] One method that can be used to account for this in cylindrical ion chambers is applying a shift to the measurement point. The shift of the ion chamber depth dose data is 0.6 multiplied by the cavity radius ($0.6 \cdot r_{cav}$) upstream from the center of the cavity. The other method is to account for this effective shift by applying a correction (P_{gr}) to the measurement itself. P_{gr} is dependent upon the dose gradient and the inner diameter of the chamber itself.[13]

A 6.2 P_{cel}

P_{cel} is a correction that accounts for the effect of having a central electrode in the medium. For ion chambers in which the central electrode is composed of the same material as the wall, the effect is accounted for in the P_{wall} correction factor which will be considered in the next section. For chambers with aluminum electrodes measuring 1 mm in diameter, P_{cel} was found to range between 0.9957 and 0.9926 for photon beam energies between 24 MV and 1.25 MeV respectively.[6] Recent Monte Carlo calculations of P_{cel} for the NE2571 ion chamber in photon beams show good agreement with the values used in TG-51.[14]

A 6.3 P_{wall}

P_{wall} is the wall correction factor that corrects for dose perturbations introduced by the placement of the wall material into the beam and can be described by:

$$P_{wall} = \frac{D_{air}(\text{no wall})}{D_{air}(\text{wall})} \qquad 14$$

The derivation of P_{wall} given here is the result of work done by Shiragai.[15,16] The dose to air in the cavity of an ion chamber when performing measurement within a water phantom has two components. The first dose component is due to those electrons set in motion within the water surrounding the ion chamber; the second component of the dose to air arises from those electrons set in motion within the ion chamber wall. Assuming that the entire dose to air results from the first component, the total dose would be

$$D^{\circ}_{air}(\text{water}) = D_{water}\left(\overline{L/\rho}\right)^{air}_{water} \qquad 16$$

In a similar manner, if it is assumed that the entire dose arises from electrons set in motion within the wall material, the dose would be described by the following equation:

$$D^{\circ}_{air}(wall) = D_{water}\left(\overline{L/\rho}\right)^{air}_{wall}\left(\overline{\mu_{en}/\rho}\right)^{wall}_{water} \qquad 17$$

where $\left(\overline{\mu_{en}/\rho}\right)_{water}^{wall}$ is the wall-to-water ratio of mean mass energy absorption coefficients. In actuality the dose to air is comprised of both components and can be described by

$$D_{air} = D_{water}\left[\alpha\left(\overline{L/\rho}\right)_{wall}^{air}\left(\overline{\mu_{en}/\rho}\right)_{water}^{wall} + \beta\left(\overline{L/\rho}\right)_{water}^{air}\right] \qquad 18$$

where α and β are the relative contributions of these two component to the total dose. If the wall material of the ion chamber were made out of water Eq. (18) would simplify to Eq. (16) which assumes that $\alpha + \beta = 1$. This is assumed to hold for other wall materials and thus:

$$D_{air} = D_{water}\left[\alpha\left(\overline{L/\rho}\right)_{wall}^{air}\left(\overline{\mu_{en}/\rho}\right)_{water}^{wall} + (1-\alpha)\left(\overline{L/\rho}\right)_{water}^{air}\right] \qquad 19$$

As P_{wall} is a ratio of D_{air}(no wall) to D_{air}(wall) it can be described as:

$$P_{wall} = \frac{1}{\left(\overline{L/\rho}\right)_{air}^{water}\left[\alpha\left(\overline{L/\rho}\right)_{wall}^{air}\left(\overline{\mu_{en}/\rho}\right)_{water}^{wall} + (1-\alpha)\left(\overline{L/\rho}\right)_{water}^{air}\right]} \qquad 20$$

In the case of an ion chamber which employs a waterproof sheath Eq. (20) is modified to:

$$P_{wall} = \frac{1}{\left(\overline{L/\rho}\right)_{air}^{water}\left[\alpha\left(\overline{L/\rho}\right)_{wall}^{air}\left(\overline{\mu_{en}/\rho}\right)_{water}^{wall} + \tau\left(\overline{L/\rho}\right)_{sheath}^{air}\left(\overline{\mu_{en}/\rho}\right)_{water}^{sheath} + (1-\tau-\alpha)\left(\overline{L/\rho}\right)_{water}^{air}\right]} \quad 21$$

where τ is the relative contribution of ionization resulting from electrons that originate in the waterproof sheath.

A 7 $N_{D,w}^{^{60}Co}$

$N_{D,w}^{^{60}Co}$ is the absorbed dose-to-water calibration coefficient for a ^{60}Co beam determined at a standards lab. $N_{D,w}^{^{60}Co}$ has the units of Gy/C. The absorbed dose measured for the $N_{D,w}^{^{60}Co}$ value is the dose in water at the ion chambers point of measurement.[1] Assumptions made for $N_{D,w}^{^{60}Co}$ are:[1]

1. Standard temperature, pressure and relative humidity.
2. 100% ion pair collection efficiency.

A 8 Conclusion

The TG-51 protocol discussed in appendix A provides the basic frame work of the Monte Carlo determined HT TG-51 calibration described in chapter 3.

References

[1] P. R. Almond, P. J. Biggs, B. M. Coursey, W. F. Hanson, M. S. Huq, R. Nath, and D. W. O. Rogers, ''AAPM's TG–51 protocol for clinical reference dosimetry of high-energy photon and electron beams,'' Med. Phys. **26**, 1847-1870 (1999).

[2] AAPM TG–21, ''A protocol for the determination of absorbed dose from high-energy photon and electron beams,'' Med. Phys. **10**, 741-771 (1983).

[3] D.W.O Rogers "Why use TG-51" Canadian Medical Physics News Letter / Le bulletin canadien physique medicale. **46**, 106-107 (2000)

[4] ICRU, " Stopping powers for electrons and positrons," ICRU Report 37, ICRU, Washington D.C. (1984).

[5] ICRU, "Radiation Dosimetry: Electron Beams with energies between 1 and 50 MeV,"ICRU Report 35, Bethesda MD (1984)

[6] C.M. Ma, A.E. Nahum, "Effect of size and composition of central electrode on the response of cylindrical ionization chambers in high energy photon and electron beams." Phys. Med. Biol. **38,** 267-290 (1993)

[7] K. Shortt, J. Shobe, S. Domen "Comparison of dosimetry calibration factors at the NRCC and the NIST. National Research Council of Canada. National Institute of Standards and Technology" Med. Phys. **27** 1644-1654 (2000)

[8] G.X. Ding, J.E. Cygler, C.B. Kwok. "Clinical reference dosimetry: comparison between AAPM TG-21 and TG-51 protocols." Med. Phys. **27,** 1217-25 (2000)

[9] D. W. O. Rogers, "Fundamentals of dosimetry based on absorbed dose standards," in *Teletherapy: Present and Future*, edited by T.R. Mackie and J.R. Palta J. R. AAPM Advanced Medical Publishing, Madison, 319-356 (1996)

[10] J.W. Boag, "Ionization Chambers" in The Dosimetry of Ionizing Radiatio, Volume II. edited by K.R. Kase,B.E. Bjarngard, F.H. Attix,Academic Press San Diego California, 169-244 (1987).

[11] F.H. Attix, Introduction to Radiological Physics and Radiation Dosimetry. New York, John Wiley & Sons (1986).

[12] D. W. O. Rogers and C. L. Yang, ''Corrected relationship between $\%dd(10)_x$ and stopping-power ratios,'' Med. Phys. **26**, 538-540 (1999).

[13] K.A. Johansson, L. Lindborg Mattson, and H Svensson, "Absorbed-dose determination with ionization chambers in electron and photon beams having energies between 1 and 50 MeV," in *Proceedings of the IAEA Symposium on National and International Standardization of Radiation Dosimetry.* AEA, Vienna 243-270 (1978)

[14] L.A. Buckley, I. Kawrakow, D.W.O. Rogers,"CSnrc: correlated sampling Monte Carlo calculations using EGSnrc." Med .Phys. **12** 3425-3435 (2005)

[15] A Shirigai, " A proposal concerning the absorbed dose conversion factor." Phys. Med. Biol. **23** 245-252 (1978)

[16] A Shirigai, "Effective mass stopping power ratio in photon dosimetry." Phys. Med. Biol. 452 -454 (1979)

Appendix B: Monte Carlo and the EGSnrc User Codes

B 1 The Monte Carlo Method

The majority of the values required for the HT TG-51 external beam dosimetry protocol calibration in chapter 3 are determined using the Monte Carlo method to simulate radiation transport by using the EGSnrc monte carlo user codes. Because the Monte Carlo method and the associated EGSnrc user codes are important to chapter 3, various aspects of both are reviewed here. The Monte Carlo method was developed shortly after World War II and has been primarily credited to Stanislaw Ulam, and John Von Neuman.[1] The Monte Carlo method uses statistically random samplings of a large number of stochastic events (in our case microscopic photon, electron and positron interactions) to determine approximate solutions to complex macroscopic problems such as electron spectra at a specific location. For problems of significant complexity, the Monte Carlo method offers an efficient alternative as compared to deterministic methods.[2,3]

To illustrate the Monte Carlo method of radiation transport, we consider the distance to interaction of a photon within a medium. The probability of a photon having had no interaction at a depth in a medium is:

$$p(z) = e^{-\mu_p z} \qquad 1$$

where μ_p is the interaction coefficient for a photon of a specific energy in a known medium and z is the distance between 0 and ∞. The cumulative probability distribution is then given by:

$$c(z) = \frac{\int_0^z e^{-\mu_p z'} dz'}{\int_0^\infty e^{-\mu_p z} dz'} = 1 - e^{-\mu_p z} \qquad 2$$

The cumulative probability distribution can be mapped on to a random number map where r is a random number that is uniformly distributed between 0 and 1 thus

$$r = 1 - e^{-\mu_p z}. \qquad 3$$

Inverting Eq. (3) makes it possible to obtain a sample set of z distributed according to Eq 1. The inverted form of Eq. (3) is

$$z = -\frac{1}{\mu_p} \ln(1 - r). \qquad 4$$

It becomes possible using a random number generator to simulate the distance to interaction of individual photons. With increased knowledge of the probability distribution of other microscopic events undergone by photons, electrons and positrons, it is possible to track both the position of the initial photon and the products (photons electrons and positrons) which result directly or indirectly from the individual interactions. This list of events resulting from an initial single particle is commonly referred to as a history. Solutions to complex problems can be obtained by generating and tabulating the results from a large number of histories. Statistical uncertainty in

Monte Carlo is related to the number of histories simulated (N) and generally decreases as $\sqrt{N}$.[4,5]

As is obvious from Eq. (4), an important part of any Monte Carlo code is the random number generator. Ideal random number generators, generate a sequence of pseudorandom numbers with a uniform distribution. Two desirable qualities in a random number generator to be used in a Monte Carlo code are

1) The same sequence of numbers can be generated given the same starting point or seed regardless of the computer platform.
2) It is capable of producing multiple sequences that are independent of one another so that parallel calculations can occur without subsequent correlations in the results.

B 2 EGSnrc

The Monte Carlo determined values required for the TG-51 calibration of the HT system (discussed in chapter 3) are calculated using the EGSnrc user codes.[3,6] The electron gamma shower (EGS) user code was initially developed at the Stanford Linear Accelerator (SLAC) in the 1970s. The motivation for development of the code was to aid in shower detector design. A shower refers to the path of the original particle and all the particles resulting from direct or indirect interactions with the original particle. The use of EGS for medical physics applications increased through the late 80s spurred primarily by its abilities for track particles to clinically relevant energies. A

decade later the EGS code system was moved from Stanford to the National Research Council of Canada (NRCC) in Ontario and the 1st version of EGSnrc was released in 2000.[7] .The random number generator employed by EGSnrc is called RANLUX and has a periodicity of $>10^{165}$ and features both of the desirable qualities mentioned in the previous section.[8,9]

B 2.1 Photon Transport

There are three primary steps by which photon interactions are handled in the EGSnrc code:

1) The distance to the interaction is determined (see section A 1) and the particle is transported in a straight line to the location of interaction
2) The type of interaction (Compton scattering, Rayleigh scattering, photo electric absorption, pair production, triplet production) is determined according to the relative contribution each process makes to the total cross section
3) The new direction and energy of the photon and any new products are determined according to the differential cross section.

These steps are repeated until the photons energy drops below the defined cut off energy, (PCUT) or leaves the geometry of interest.. The current minimum value for PCUT in the EGSnrc user codes is 10 keV. All interaction products are added to the simulation and are transported to their eventual end.

B 2.2 Charged Particle Transport

Compared to photon transport, charged particle transport represents a relatively complicated problem. Considering that a single 1 MeV electron undergoes approximately 10^6 interactions[3] prior to be being locally absorbed it is easy to understand how the time required to perform all these calculations would quickly make any large simulation not feasible even using the current generation of relatively fast processors. To account for this, EGSnrc employs a class II condensed history algorithm for charge particle transport. A class II condensed history algorithm treats hard and soft collisions differently. Hard collisions including hard brehmsstrahlung, hard inelastic collisions, and annihilation events in which a large amount of energy is exchanged as defined by the electron and photon energy threshold values of AE and AP are treated individually. Soft collision such as soft brehmsstrahlung and soft inelastic collisions and elastic collisions which account for the vast majority of interactions are grouped. Energy deposited from soft brehmsstrahlung and soft inelastic collisions is determined using the restricted radiative stopping power and the restricted collisional stopping power respectively. Elastic scattering is accounted for by the multiple scattering theory differential cross sections.[3] The steps for charged particle transport are similar to that for photon transport and involves the following steps:

1) The distance to the next hard collision is determined and the charged particle is transported to the location. Energy is lost on the way as determined by the restricted radiative and collisional stopping powers which are considered

constant over the step. Angular deflections are determined according to multiple elastic scattering theory.

2) At the hard collision location the type of interaction (hard brehmsstrahlung, hard inelastic collision, annihilation) is determined.
3) The new energy and direction of the charged particle are determined according to the interaction along with any secondary products.

These steps are repeated until the charged particles energy drops below the defined cut off energy (ECUT). The current minimum value for ECUT in the EGSnrc user codes is 521 keV.[6] Secondary particles resulting from these interactions are added to the simulation and transported to their eventual end. As default within 3 elastic mean free path lengths of a material boundary the interactions are simulated on an interaction by interaction basis.[3]

B 3 EGSnrc User Codes

B 3.1 BEAMnrc

BEAMnrc is a general purpose Monte Carlo code for simulating radiotherapy sources. It is based on a series of 'component modules', which describe simulation geometries useful for describing components of the linear accelerator machine head (MLC, Jaws, Cones etc.), and which allows for the construction of a wide variety of radiation sources from x-ray tubes and Co^{60} to standard linear accelerators.[10,11]

B 3.2 DOSXYZnrc

DOSXYZnrc is a user code that simulates photon and electron dose deposition through various materials in a Cartesian geometry. The geometry may be user defined or created from CT data sets.[12]

B 3.3 SPRRZnrc

SPRRZnrc is a user code that calculates stopping power ratios within regions of a cylindrical geometry. The method by which SPRRZnrc calculates the mean restricted mass stopping power ratio is by scoring the total dose in the two media within the region of interest. The entire calculation is performed in the transport media and not the detector media.[6] The dose deposition is considered to have 4 modes:

Mode 1: Contains all electron interactions in which the electron start and finish energy are above Δ.

Mode 2: Contains all interactions in which the electron energy is above Δ prior to the interaction and below Δ after the interaction.

Mode3: Contains all the electrons and photons that are being stopped because their energy is below Δ.

Mode 4: Is a subset of Mode 3 and contains those photons and electrons that are created below the Δ value.

Mode 2 is broken into two stages; the stage that occurs above Δ and the stage that occurs below Δ. All modes that occur below Δ are termed stoppers. The dose is

deposited within the transport and is just the sum of the energy depositions ($EDEP_{Transport}$) within the region. The energy deposited in the detector media is determined by summing the energy depositions ($EDEP_{Detector}$) which are determined according to

$$EDEP_{Detector} = EDEP_{Transpost} \frac{\left(L(E_{mid})/\rho\right)_{Detector}}{\left(L(E_{mid})/\rho\right)_{Transpost}} \qquad 5$$

for the electrons as per mode 1 and

$$EDEP_{Detector} = EDEP_{Transpost} \frac{\left(S(\Delta)/\rho\right)_{Detector}}{\left(S(\Delta)/\rho\right)_{Transpost}} \qquad 6$$

for the electrons within mode 3. $\left(L(E_{mid})/\rho\right)$ is the restricted mass collision stopping power at the mid point energy of the energy step E_{mid} and $\left(S(\Delta)/\rho\right)$ is the unrestricted mass collision stopping power at energy Δ. [8] The stopping power ratio is determined by taking the ratio of the dose components from Mode 1 + Mode 2 + Mode 3 – Mode 4 of both the transport and detector medium.

B 3.4 FLURZnrc

FLURZnrc is a user code that calculates the fluence of various particles within regions of a cylindrical geometry.[6] Within a given region the fluence (differential in energy) is calculated according to.[13,14]

$$\overline{\text{Fluence}}(\Delta E) = \frac{PL(\Delta E)}{V}, \qquad 7$$

where PL (ΔE) is the total path length for a given energy bin and V is the volume of the region of interest. Outputs include spectra, fluence versus position and spectra of primaries versus secondary particles.[6]

B 4 Conclusion

The Monte Carlo method described in appendix B provides the basis for the work done in chapter 3.

References

[1] R Eckhardt "Stan Ulam, John Von Neuman, and the Monte Carlo method, Los Alamos Science **15** 131-137 (1987)

[2] A.F. Bielajew, fundamentals of the Monte Carlo method for neutral and charged particle transport Pre-publication manuscript, Ann Arbor Michigan, (2001)

[3] I. Karwrakow and D.W.O. Rogers, The EGSnrc code system: "Monte Carlo simulation of electron and photon transport," Technical Report No. PIRS 701 National Research Council of Canada, Ottawa, Canada (2002).

[4] G.S. Fishman Monte Carlo Concept, Algorithms and Applications 1, ed. Springer Verlag, London (1996)

[5] R.Y. Rubinstein, Simulation and the Monte Carlo Method 1ed. Wiley-Interscience, Hoboken,NewJersey (1981)

[6] D. W. O. Rogers, I. Kawrakow, J. P. Seuntjens, and B. R. B. Walters, ''NRC User Codes for EGSnrc,'' Technical Report No. PIRS-702, National Research Council of Canada, Ottawa, Canada (2002).

[7] I. Karwrakow, "Accurate condensed history Monte Carlo simulations of electron transport I. EGSnrc, the new EGS4 version." Med. Phys. **27** 485-498, (2000)

[8] F.James, "RANLUX: A Fortran implementation of the high quality pseudo random number generator of Luscher," Computer Phys. Commun. **79** 111-114 (1984)

[9] M.Luscher, " A portable high-quality random number generator for lattice field theory simulations," Computer Phys Commun, **79** 100-110 (1994)

[10] D. W. O. Rogers, B. A. Faddegon, G. X. Ding, Ma C.M. We J, Mackie T.R., "BEAM: a Monte Carlo code to simulate radiotherapy treatment units," Med. Phys. **22**, 503-524 (1995).

[11] D. W. O. Rogers, C.-M. Ma. B. Walters, G.X. Ding, D. Sheikh-Bagheri and G. Zhang, ''BEAMnrc Users Manual,'' Technical Report No. PIRS-509(a), National Research Council of Canada, Ottawa, Canada (2003).

[12] B. R. B. Walters and D. W. O. Rogers,''DOSXYZnrc Users Manual,'' Technical Report No. PIRS-794, National Research Council of Canada, Ottawa, Canada (2002).

[13] A.B. Chilton, "A Note on the Fluence Concept", Health. Phys. **34**, 715-716 (1978)

[14] A. B. Chilton, "Further Comments on an Alternative Definition of Fluence," Health Phys. **35**, 637- 638 (1979).

Appendix C: Introduction to MRI

C 1 The Quantum Mechanical Description of NMR

C 1.1 Spin ½ in a Static Magnetic Field B_O

Nuclei probed in the nuclear magnetic resonance (NMR) experiment have an associated magnetic dipole moment $\boldsymbol{\mu}$ which is related to the spin angular momentum operator of the nuclei, **I,** through the equation:

$$\boldsymbol{\mu} = \gamma\hbar\mathbf{I} \qquad 1$$

where γ is the gyromagnetic ratio of the nuclei having the units frequency over magnetic field. The γ for the hydrogen nucleus (a proton) which is of importance to the work done in this thesis is 42.7 MHz/Tesla. The term $\hbar$ is plank's constant h divided by 2π and has the value of ($\hbar = 1.054 \times 10^{-34}$ Js).

The interaction energy of a magnetic moment in a magnetic field B is defined by:

$$E = -\boldsymbol{\mu} \bullet \mathbf{B} \qquad 2$$

For the case of a hydrogen nuclei (I=½) in a static uniform magnetic field B_O oriented in the Z direction of the Cartesian reference frame this equation becomes:

$$E = -\gamma\hbar\mathbf{I} \bullet \mathbf{B}_O \qquad 3$$

Rearranging equation 3 into operator form we get the Zeeman Hamiltonian operator:

$$H_{B_O} = -\gamma\hbar \mathbf{B_O} \mathbf{I_z} \qquad 4$$

Applying the Zeeman Hamiltonian operator to the energy eigenstates in the spin wave function results in the energy eigenvalues of the corresponding eigenstates defined by:

$$H_{B_O}\left(|\alpha\rangle + |\beta\rangle\right) = E\left(|\alpha\rangle + |\beta\rangle\right) = \gamma\hbar \mathbf{B_O}/2|\alpha\rangle + -\gamma\hbar \mathbf{B_O}/2|\beta\rangle \qquad 5$$

where $|\alpha\rangle$ are spins oriented parallel to $\mathbf{B_O}$ and $|\beta\rangle$ are oriented anti-parallel to $\mathbf{B_O}$. It is thus seen that when a spin ½ system is placed in a static magnetic field, it can be described as existing in either ($|\alpha\rangle$ or $|\beta\rangle$) state or a mixture of both.[1] (figure. C-1)

Another way of writing the Zeeman energy is:

$$\Delta E = \hbar\omega_o \qquad 6$$

requiring:

$$\omega_O = \gamma B_O \qquad 7$$

where ω_O is called the Larmor frequency. In thermal equilibrium conditions the relative populations of spins in each eigenstate is determined by the Boltzman distribution[2] expressed as:

$$\frac{N_{|\beta\rangle}}{N_{|\alpha\rangle}} = e^{-\Delta E/kT} \qquad 8$$

here $N_{|\alpha\rangle}$ and $N_{|\beta\rangle}$ represent the number of spins in the $|\alpha\rangle$ and $|\beta\rangle$ eigenstates, k is Boltzman's constant (k=1.38 * 10^{-23} J/K) and T is the temperature in Kelvin. In the absence of a magnetic field the orientation of a spin is equally probable in any direction. A spin in the presence of a static magnetic field will preferentially align itself parallel to the field. The preference of spins to align parallel to the static magnetic field gives rise to a net longitudinal magnetization.

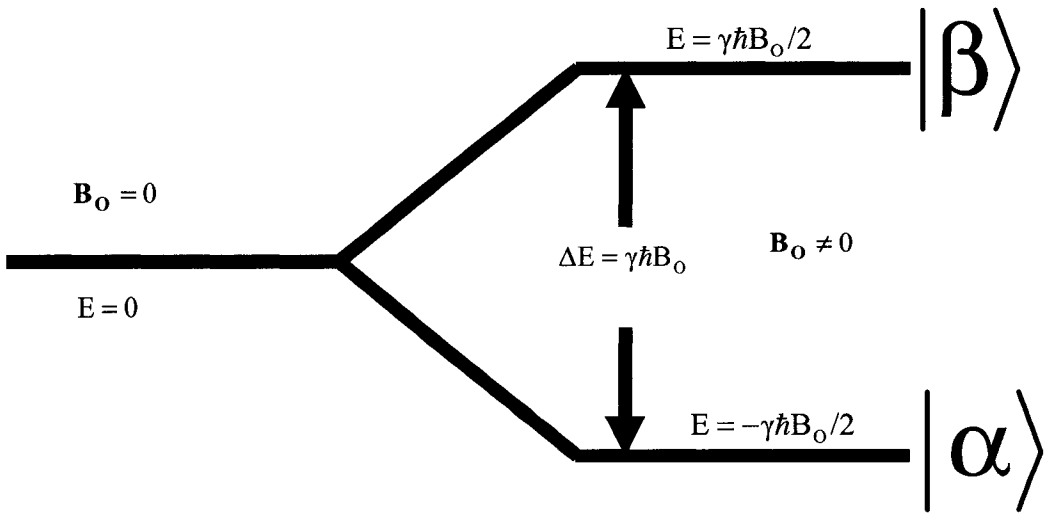

Figure. C-1 Demonstrates demonstrate the split in energy levels that results from a spin ½ system moved from a magnetic field of $B_O = 0$ to a magnetic field of $B_O \neq 0$.

C 2 The Classical Description of NMR

Consider an arbitrary ensemble of protons each with an individual magnetic moment of $\boldsymbol{\mu}$. The net magnetization within the ensemble arises from the sum of the magnetic moment vectors with the sample:

$$\mathbf{M} = \sum_{\text{Volume}} \boldsymbol{\mu}_i \qquad 9$$

In the absence of a magnetic field these moment vectors will orient themselves randomly throughout the ensemble.(figure C-2(a)) Due to the cancellation of these individual moments there will be no net magnetization within the sample.[2]

C 2.1 Magnetic Moment in a Static Magnetic Field B_O

If the ensemble is placed in a static magnetic field oriented in the Z direction, the magnetic moment vectors of the protons will align with the field in either the parallel or anti-parallel directions. Although it is possible for the magnetic moments to align in either the parallel or anti parallel direction the preference will be towards the parallel orientation which in turn will give rise to a net magnetization of the ensemble as shown in figure. C-2(a). This preference of spins to align in the parallel state gives rise to the ensembles longitudinal magnetization (figure. C-2(b)).

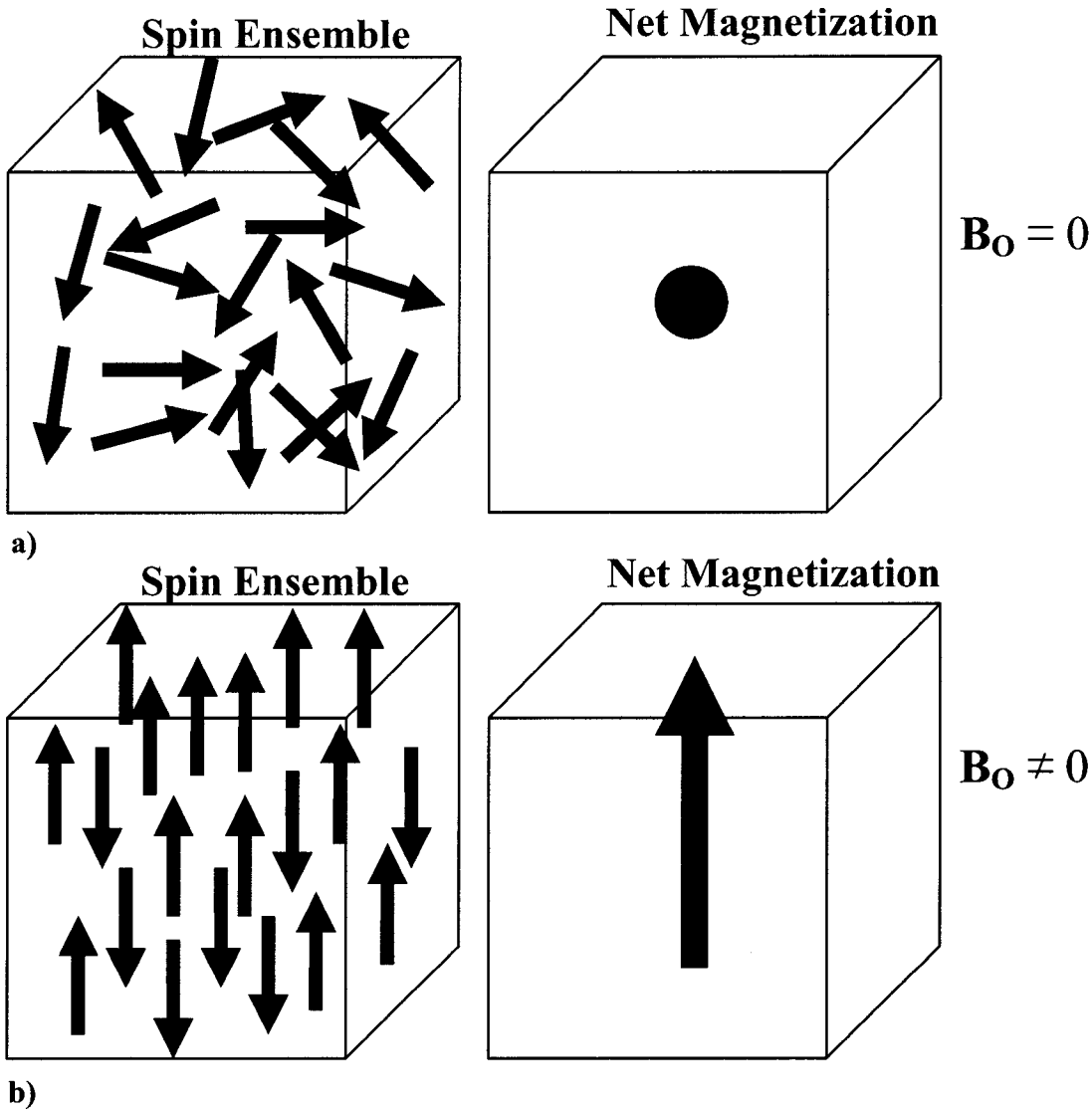

Figure. C-2 Shows the net magnetization from an ensemble of magnetic moment vectors. In (a) they are in a magnetic field of $B_O = 0$ and are arranged with random direction causing a net magnetization of 0 represented by the sphere. In (b) the magnetic moment align in parallel/anti-parallel configurations with respect to the non-zero magnetic field. The result is a net magnetization represented by the large arrow.

The equations of motion for the angular momentum vectors can written by equating the angular momentum **I**, to the torque between the magnetic moment vector and the magnetic field, **B**. The equations of motion for these magnetic moment vectors can thus be written as:

$$\hbar \frac{d\mathbf{I}}{dt} = \boldsymbol{\mu} \times \mathbf{B} \qquad 10$$

Using equation 1 we can eliminate **I** to get:

$$\frac{d\boldsymbol{\mu}}{dt} = \gamma \boldsymbol{\mu} \times \mathbf{B} \qquad 11$$

If B is such that $\mathbf{B} = (0,0,B_O)$, the we can solve the equations of motion for the three Cartesian components of $\boldsymbol{\mu}$ which are[2]:

$$\frac{d\mu_x}{dt} = \gamma \mu_y B_O \qquad 12$$

$$\frac{d\mu_y}{dt} = -\gamma \mu_x B_O \qquad 13$$

$$\frac{d\mu_z}{dt} = 0 \qquad 14$$

The solution these three first order differential equations are:

$$\mu_x(t) = \mu_{xo}\cos(\omega_O t) + \mu_{yo}\sin(\omega_O t) \qquad 15$$

$$\mu_y(t) = -\mu_{xo}\sin(\omega_O t) + \mu_{yo}\cos(\omega_O t) \qquad 16$$

$$\mu_z(t) = \mu_{zo} \qquad 17$$

where $\omega_O = \gamma B_O$ showing the magnetic moment precesses in a negative sense about the Z axis with a frequency that is proportional to the magnitude of the magnetic field in which it is placed. (figure. C-3) It should be noted by the reader that this result is the same as determined in the quantum mechanical description of spin ½ in a static magnetic field B_O.(See Eq. (7))

In thermal equilibrium μ will have a random transverse phase (and thus vector cancellation) throughout the ensemble of spins with the result being no net magnetization in the transverse plane. Magnetization along the Z axis will be determined according to Eq. (9).

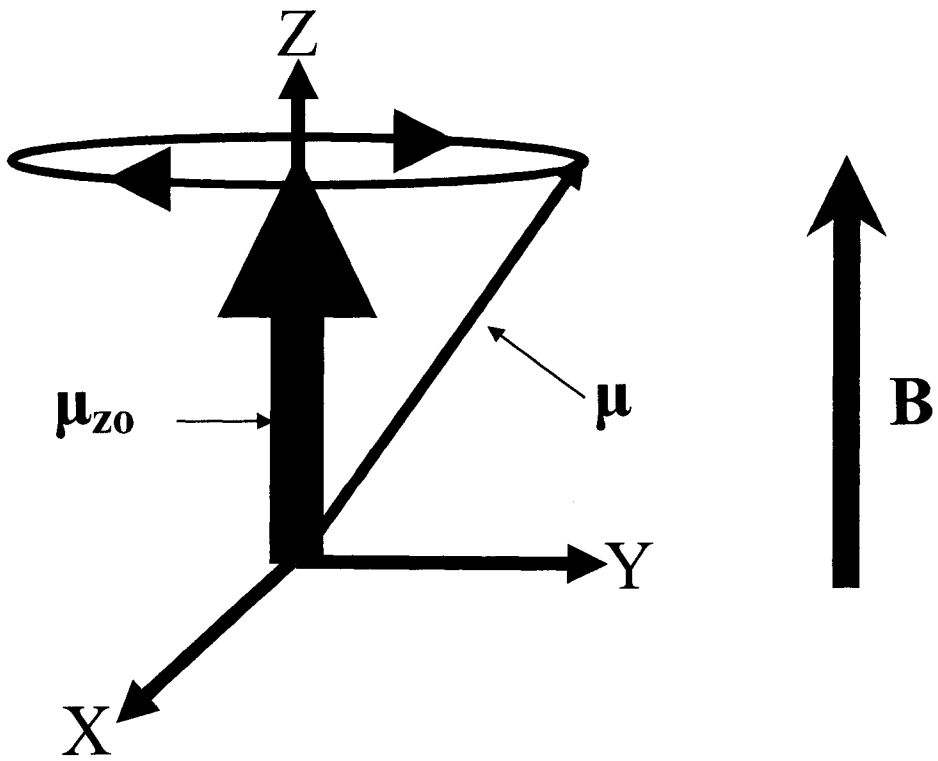

Figure. C-3 Demonstrates the magnetic moment vector (μ) of a proton in a static magnetic field B, which is oriented in the z direction of the Cartesian reference frame. Notice how μ precesses in a negative sense about the z axis in a negative sense.

C 2.2 Magnetic Moment in a Static Magnetic Field B_O and a Radiofrequency RF Circularly Polarized Magnetic field $B_1(t)$

Excitation of the NMR spin system is accomplished through the application of a circularly polarized magnetic field which is termed a radiofrequency (RF) pulse. This circularly polarized magnetic field $\mathbf{B_1}$ (RF pulse) is applied in a direction orthogonal to the static magnetic field $\mathbf{B_O}$ and at a frequency of ω_1. The total resultant field **B** becomes:

$$\mathbf{B} = \mathbf{B_O} + \mathbf{B_1}(t) \qquad 18$$

where

$$\mathbf{B_O} = (0,0,B_O) \qquad 19$$

and:

$$\mathbf{B_1} = (B_1\cos(\omega_1 t), -B_1\sin(\omega_1 t), 0). \qquad 20$$

Combining equations 18 – 20 gives the total magnetic field **B** as:

$$B = (B_1\cos(\omega_1 t), -B_1\sin(\omega_1 t), B_O) \qquad 21$$

Describing the motion of **μ** becomes considerably more complex when dealing with both the static and circularly polarized magnetic fields required for excitation of the NMR spin system. Changing the reference frame from a basic Cartesian (Laboratory) reference frame to a rotating reference frame will help make the process more intuitive.[1] If we imagine a merry-go-round (MGR), the Cartesian reference frame can be likened to observing the MGR from a point beside the MGR, and the rotating reference frame can be likened to observing the MGR while standing on the MGR. From the Cartesian reference frame the motion of the model horses on the MGR will appear to be sinusoidal moving within three dimensions. This motion is

greatly simplified when viewed from the rotating reference frame where the apparent motion of the model horses breaks down into only up and down components.

The rotating reference frame rotates in the same sense and at the same frequency as the applied $B_1(t)$ field (figure. C-4). The components of the magnetic moment vectors in the rotating reference frame (denoted by subscript ρ) are related to the components in the Cartesian reference according to:

$$\mu_{x\rho} = \mu_x \cos\omega_1 t - \mu_y \sin\omega_1 t \qquad 22$$

$$\mu_{x\rho} = \mu_x \sin\omega_1 t + \mu_y \cos\omega_1 t \qquad 23$$

$$\mu_{z\rho} = \mu_z \qquad 24$$

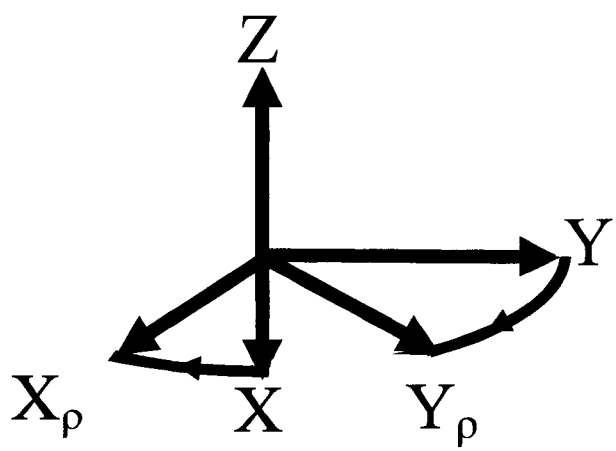

Figure. C-4 demonstrates the relationship between the laboratory (X,Y,Z) and rotating reference frames (X_ρ,Y_ρ,Z_ρ). The rotating reference frame rotates in the same sense and at the same frequency as $B_1(t)$

Applying this new B from Eq. (18) and converting from the Cartesian reference frame to the rotating reference frame results in the following differential equations.

$$\frac{d\mu_{x\rho}}{dt} = (\gamma B_O - \omega_1)\mu_{y\rho} \qquad 25$$

$$\frac{d\mu_{y\rho}}{dt} = -(\gamma B_O - \omega_1)\mu_{x\rho} + \gamma B_1 \mu_{z\rho} \qquad 26$$

$$\frac{d\mu_{z\rho}}{dt} = -\gamma B_1 \mu_y \qquad 27$$

and shown in a simpler form as

$$\frac{d\boldsymbol{\mu}_\rho}{dt} = \gamma \boldsymbol{\mu}_\rho \times \mathbf{B}_{eff} \qquad 28$$

where the effective magnetic field ($\mathbf{B}_{eff}$) is

$$\mathbf{B}_{eff} = B_{1x\rho}\hat{i}_\rho + (B_O - \omega_1/\gamma)\hat{k}_\rho \qquad 29$$

Eq. (28) is the same form as appears in Eq. (11) which is an equation for the Cartesian reference frame. The difference between Eqs. (11) and (28) is the B_{eff} term which unlike B_O has components in both the X and Z directions. In the rotating reference frame the magnetic moment will precess in a cone about the axis of B_{eff} with a

frequency of $\omega_1=\gamma B_{eff}$. (figure. C-5) When ω_1 is applied such that $\omega_1=\gamma B_O$, B_{eff} becomes parallel to B_1. In the case where B_1 is applied at the larmor frequency along the X_ρ direction the magnetic moment will precess about X_ρ in the $Y_\rho Z_\rho$ plane. Thus if a circularly polarized magnetic field B_1 is applied for a time t the classical magnetic moment of the hydrogen protons can be tipped from the Z axis into the tranverse XY plane. This tipping of the hydrogen protons is what gives rise to the detectable signal in the NMR experiment. The angle away from the Z axis that a given pulse rotates the magnetic moment vector is referred to as a tip angle. For and an on-resonance RF pulse the tip angle is defined by:

$$\alpha_{TIP} = \gamma \int_{Pulse} B_1(t)dt \qquad 30$$

After being tipped the magnetic moment may have components in both the direction of the Z axis as well as the XY plane. The sum of z components of the magnetic moment ensemble is referred to as longitudinal magnetization (M_z). The sum of components that exist in the XY plane is referred to as transverse magnetization and is given the complex value M_{xy} defined by:

$$M_{xy} = M_x + iM_y \qquad 31$$

figures C-6(a) and C-6(b) show a 90 degree on resonant pulse from the perspective of both rotating and laboratory reference frames. The figures show the simplification which is obtained by using the rotating reference frame.

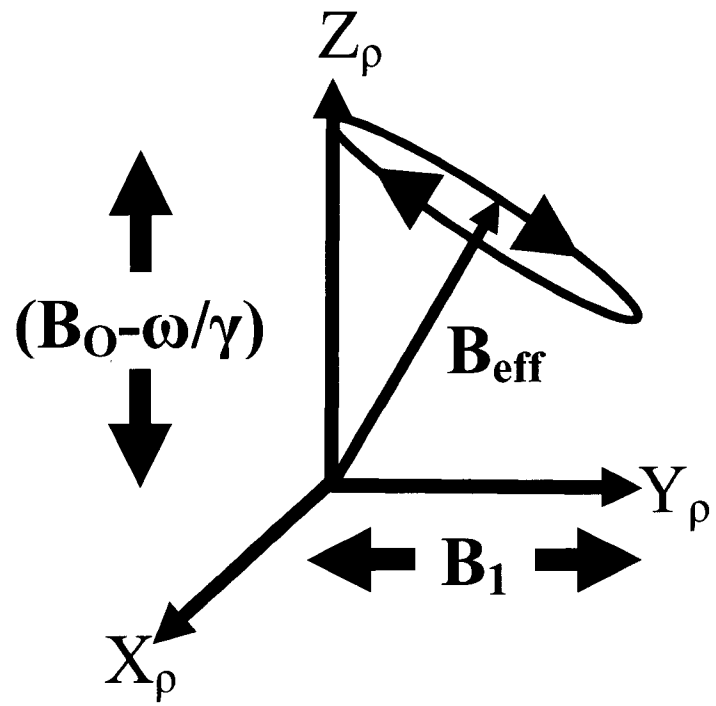

Figure. C-5 The motion of the magnetic moment vector in the rotating frame.

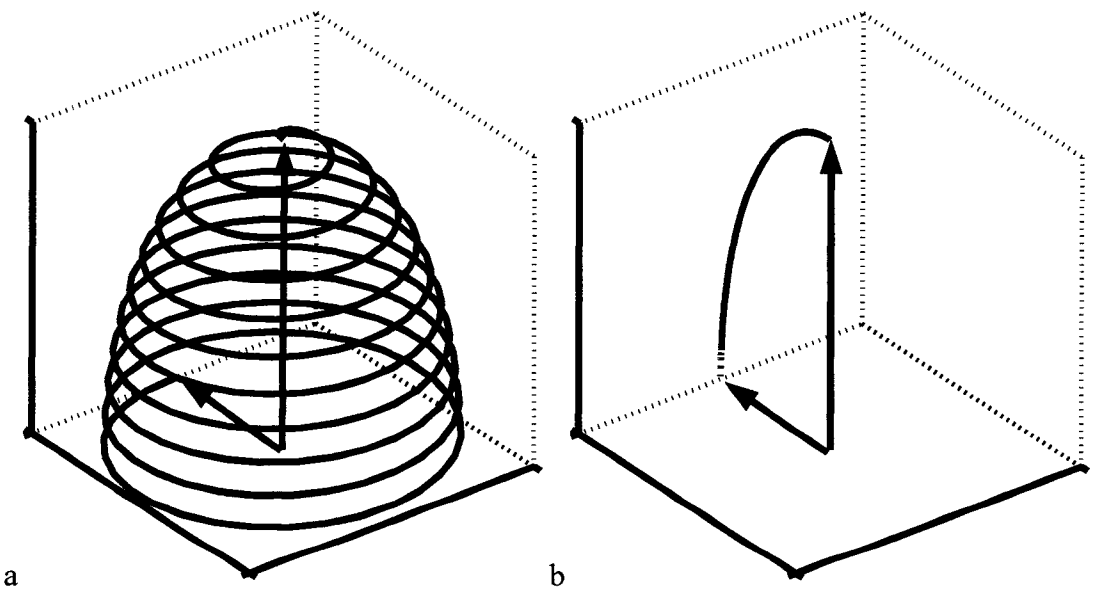

Figure. C-6 The classical magnetization vector during a 90° excitation pulse as viewed from the laboratory reference frame in a) and the rotating reference frame in b).

After having tipped the magnetic moment into the transverse plane the excitation pulse is turned off. In the laboratory reference frame the magnetic moment will behave as it did before the excitation pulse was applied (precessing about the Z axis in a negative sense). (See Eqs. (15) to (17)_. The effect of the precession of the magnetic moment will induce a current in a conducting coil placed adjacent to the sample.[1](figure. C-7(a)) The Fourier transform of this signal results in a sharp peak centered on the Larmor frequency of the magnetic moment vector (figure. C-7(b))

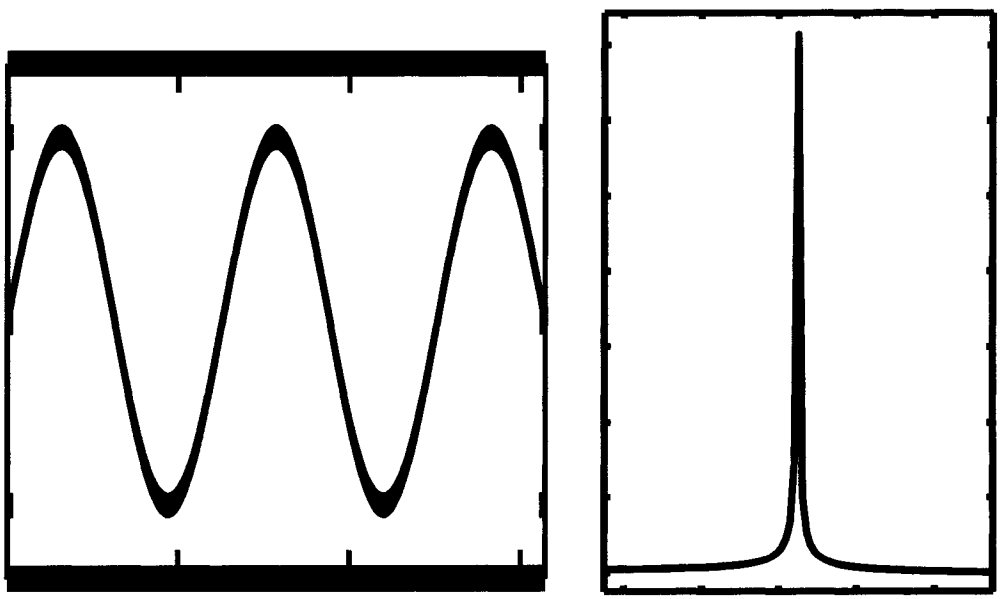

a) Time b) ω

Figure. C-7 a) demonstrates the time dependent emf resulting from the precession of the magnetic moment about the z axis and b) demonstrates its corresponding power spectrum.

C 3 Relaxation (contrast) Mechanism and the Bloch Equations

After having been perturbed from its steady state values (through the excitation process), the magnetic moment will begin to relax back to its initial steady state value. This relaxation will result in a reduction of the measurable signal (M_{xy}), and a simultaneously increase in the amount of longitudinal M_z magnetization. This relaxation process is governed by two related processes; longitudinal and transverse relaxation.

C 3.1 Longitudinal Relaxation

The longitudinal relaxation of previously excited magnetic moments is characterized by the relaxation time T1. T1 relaxation involves the evolution of the M_z component of the magnetization moment from the excited state to equilibrium state (M_O). Longitudinal or T1 relaxation is determined by the energy exchange rate between excited nuclei and the surrounding molecular lattice. This energy is exchanged through randomly changing magnetic fields resulting from the motion within the surrounding dipole lattice. Because different materials have different molecular lattices the energy exchange rate between a magnetic moment and this lattice will also differ between different materials (figure. C-8(a)). Because of the greater energy required for relaxation at higher frequencies, longitudinal relaxation will occur at a lower rate at higher B_O. Both Bloch[3] and Purcel[4] noted that the relaxation rate was dependent on the degree by which the magnetic moments have been removed from their thermal equilibrium position. (figure. C-8(b)) The change in the longitudinal component of the magnetization can be described by the equation:

$$\frac{dM_z}{dt} = \frac{(M_O - M_z(t))}{T1} \qquad 32$$

where M_z is the magnetization along the Z axis and T1 is a constant that defines the longitudinal relaxation rate for various materials. Solving the 1st order differential equation yields:

$$M_z(t) = M_O + (M_z(0) - M_O)e^{-t/T1} \qquad 33$$

For a 90° excitation pulse the equation becomes:

$$M_z(t) = M_O(1 - e^{-t/T1}) \qquad 34$$

and for a 180° pulse the equation becomes:

$$M_z(t) = M_O(1 - 2e^{-t/T1}) \qquad 35$$

as is implicit in equation 33, the quickest relaxation occurs immediately following excitation, and the farther away from the equilibrium state the magnetic moments are perturbed the quicker the relaxation rate (figure. C-8(b)). These differences in relaxation rates can be used to obtain contrast between different tissues through the use of appropriate timings within an MRI pulse sequence (table C-1).[5]

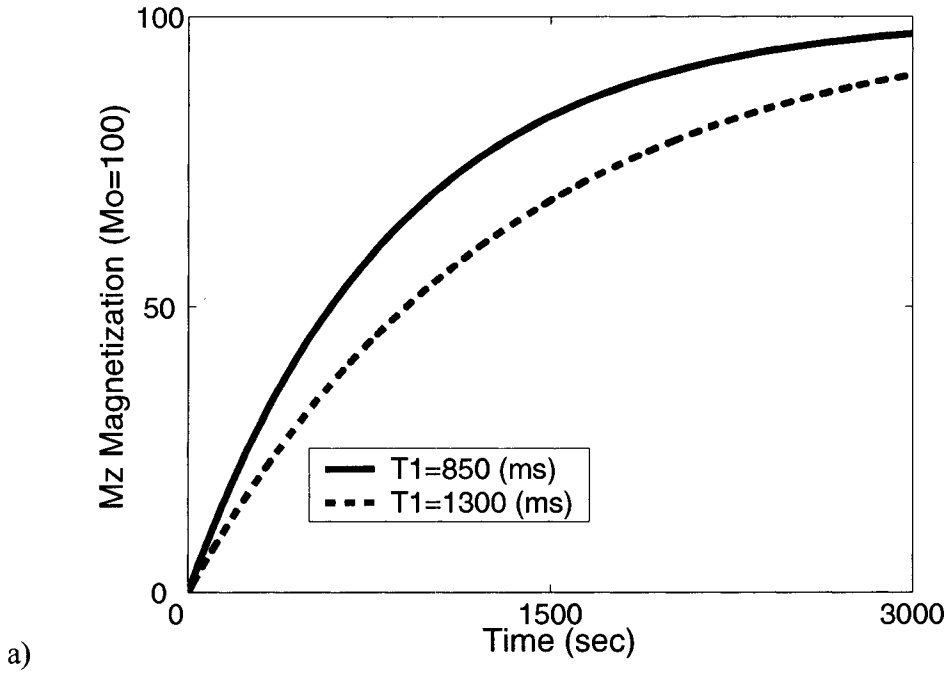

a)

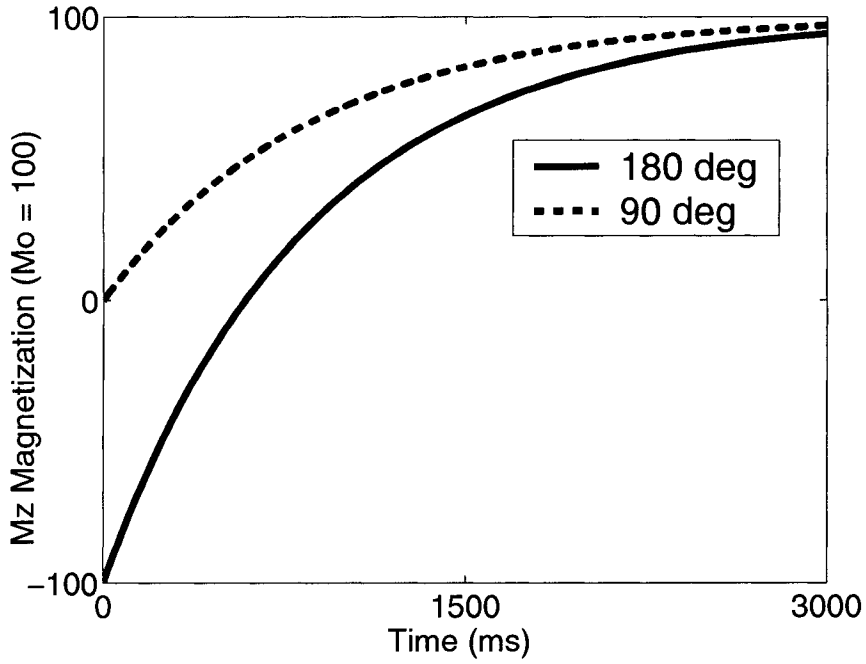

b)

Figure. C-8 a) demonstrates relaxation for grey (T1=1300 msec) and white (T1= 850 msec) matter having undergone a 90° RF pulse. In b) the relaxation for white matter having undergone both 90° and 180 ° excitation pulses.

Table C-1 Average T1 times for various tissue in both 1.5 T and 3.0 T magnetic fields

Tissue	T1(ms) @ 1.5 Tesla	T1(ms) @ 3.0 Tesla
White Matter	790	850
Grey Matter	920	1300
Cerebrospinal Fluid	~4316	~4316
Muscle	870	1073
Fat	250	419

C 3.2 Transverse Relaxation

The T2* value describes the decay of transverse relaxation through both reversible and non-reversible processes. The equation describing the decay of signal resulting from T2* relaxation is [5-8]:

$$\frac{dM_{xy}}{dt} = -\frac{M_{xy}(t)}{T2^*} \qquad 36$$

where M_{xy} is the magnetization in the transverse plane, and T2* is the transverse relaxation rate. Solving this differential equations yields:

$$M_{xy}(t) = M_{xy}(0)e^{-t/T2^*} \qquad 37$$

this is the time dependant signal decay after the initial excitation. The T2* value has two components such that:[2]

$$\frac{1}{T2^*} = \frac{1}{T2} + \frac{1}{T2'}$$ 38

The T2 component of T2* is irreversible and will ultimately result in a complete loss of coherent signal. T2 rate results from several mechanisms.[6] One factor is the spin-spin interaction in which an excited dipole will produce an on-resonance perpendicular magnetic B_1 which will excite surrounding dipole moments. Another factor is that molecular rotations and vibrations will cause the local Larmor frequency to fluctuate resulting in a loss of coherent signal (figure. C-9). The average T2 component of T2* at 1.5 T field strength are given in table C-2.[5]

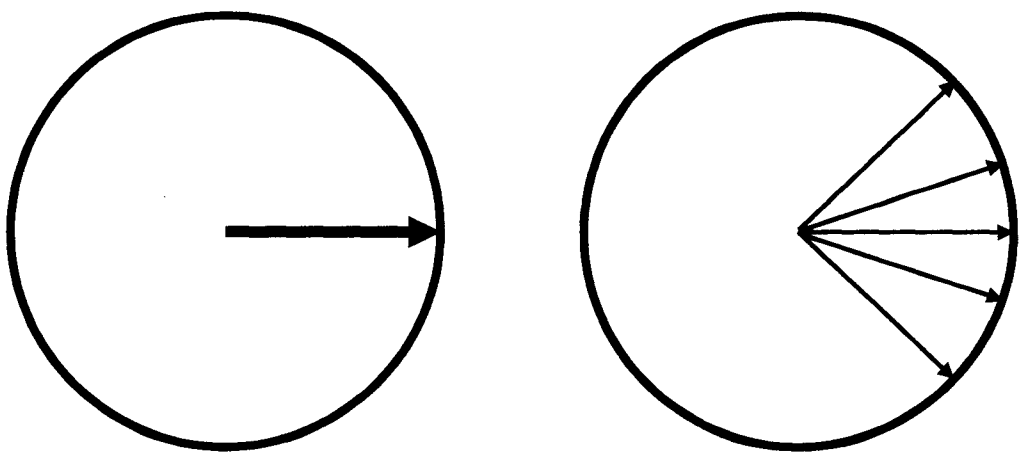

Figure. C-9 The fluctuation of ω_O results in a distribution of phase further resulting in a lost of coherent signal.

Table C-2 Average T2 times for various tissues in a 1.5 T magnetic field

Tissue	T2(ms) @ 1.5 Tesla
White Matter	92
Grey Matter	100
Muscle	470

C 4 Spatial Encoding

Spatial encoding allows for the location of the signal produced from the NMR experiment to be determined. Although the result can take several forms, for our purpose the final product of spatial encoding will be an image which relates signal frequency to spatial location. Spatial encoding involves superimposing a linearly varying magnetic field of slope G to the existing field B_O. The resultant field thus becomes.

$$B_{total} = B_O + \mathbf{G_d} \cdot \mathbf{d} \qquad 39$$

Where d is the displacement in the direction of the gradient. Using this in conjunction with equation 7 gives us the linearly varying resonance frequency.

$$\omega_{total} = \gamma(B_O + G_d \cdot d) \qquad 40$$

which in the rotating frame appears in the simpler form of:

$$\omega_\rho = \gamma(G_d \cdot d) \qquad 41$$

This result is used to spatially encode the NMR signal in three ways.

C 4.1 Slice Selection and the RF Excitation Pulse

In slice selection a gradient (G_{SS}) is applied in conjunction with an RF excitation pulse. The RF pulse is of a set bandwidth (BW_{rf}) and transmission frequency (ω_{rf}). Application of the G_{SS} results in a linear spread of the Larmor frequencies across the direction of the gradient. The RF pulse will then interact with those magnetic moments which have Larmor frequencies that are contained within BW_{rf}.[7] The thickness of the excited slice (sl) can be controlled by the adjustment of the G_{SS} such that:

$$sl = \frac{BW_{rf}}{G_{SS}} \qquad 42$$

The position of the slice can also be controlled by adjusting ω_{rf}.

The RF pulse is applied at the transmission frequency and its time domain amplitude is modulated. Fourier transforming the time domain pulse gives its associated frequency response. When the slice selection gradient is applied in the slice selection process this frequency response becomes the excitation or slice profile. In equation 42 the term BW_{rf} refers to the full width or half the maximum value of the excitation profile as shown in figure. C-10. Two common excitation pulses used in

NMR are termed hard and soft. The hard pulse has a rectangular time domain profile (figure. C-11(a)) and a corresponding Sinc frequency response function (figure. C-11(a)). The broadband frequency response profile of the hard pulse makes it a poor choice for use in slice selection. Conversely a soft pulse (in this case a truncated sinc pulse (figure. C-11(c)) has a long duration time domain profile with a narrow and sharp frequency response (figure. C-11(d)) which makes it an excellent choice for slice selection.[8] Due to RF amplifier imposed power constraint a compromise must be made between profiles in the time and frequency domains.

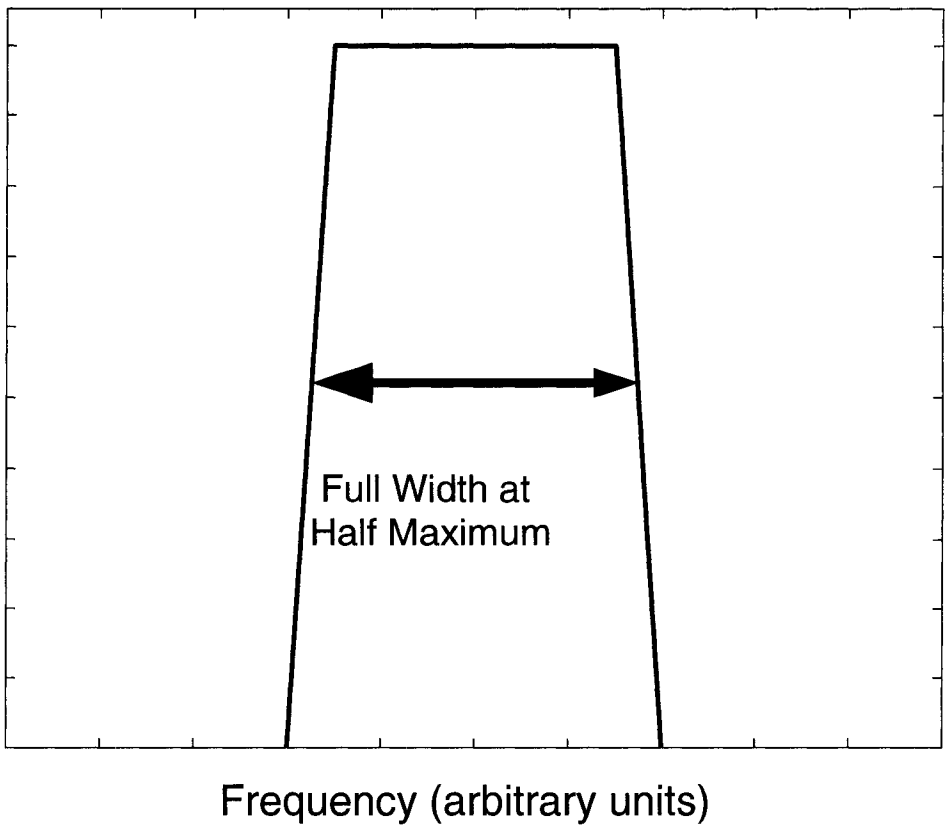

Figure. C-10 The bandwidth of an RF pulse is defined as the full bandwidth at half of the maximum amplitude of the frequency response.

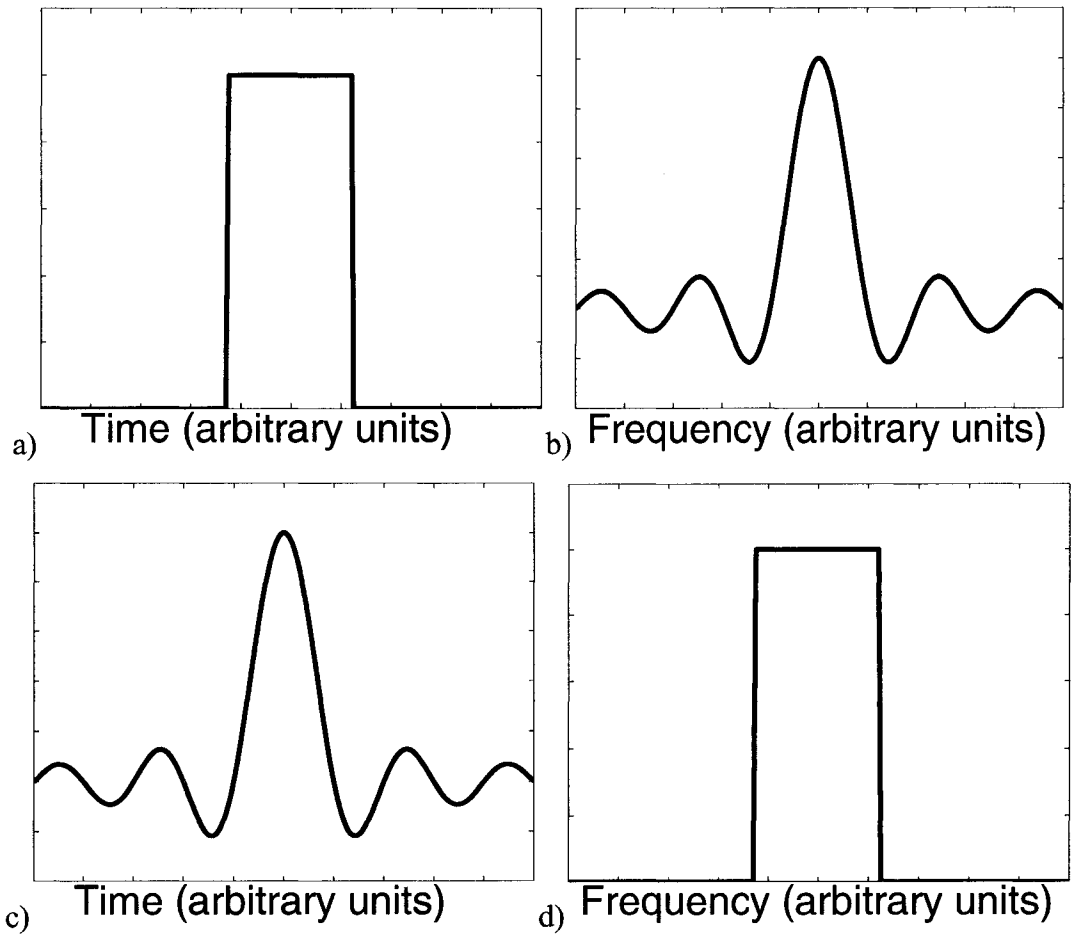

Figure. C-11 The time/frequency relations are shown for both hard (a,b) and soft (c,d) RF excitation pulses.

C 4.2 Frequency Encoding

To frequency encode the location of the excited magnetic moments a magnetic field gradient G_{read} is applied during signal acquisition. Like G_{SS} the application of G_{read} results in a linear spread of the Larmor frequencies across the spatial read encode direction. When fourier transformed the signal is separated into its frequency components, which in turn are related to spatial position. The bandwidth of the received signal is described by:

$$BW_{read} = \gamma(G_{read} FOV_{read}) \quad 43$$

where FOV_{read} is the field of view in the frequency encode direction. Assuming the object does not exist beyond FOV_{read} aliasing is avoided by satisfying the Nyquist criteria:

$$\text{Sampling Rate}_{read} \geq 2\gamma(G_{read} x_{max}) \quad 44$$

were x_{max} is the maximum displacement from gradient center. Typically the data acquisition system will apply an analogue filter to remove any frequencies above or below the range of interest. Thus aliasing is generally not a concern in the frequency encode direction.

C 4.3 Phase Encoding

The final method of spatial encoding discussed in this appendix is phase encoding. To encode a phase increment a gradient G_y is applied for a time t_{phase}. During this time the Larmor frequencies of the magnetic moment spread out according to their experienced local magnetic field. After time t_{phase} the gradient is turned off. With no gradient, the magnetic spins all return to the same Larmor frequency while maintaining a linear phase distribution across the spatial phase encode direction. (figure. C-12) The phase acquired over this time period is described by:

$$\theta = \gamma \int_{t_{phase}} \left(G_y(\tau) \cdot y_{phase} \right) d\tau \qquad 45$$

where y_{phase} is the physical displacement from the gradient center in the y direction. Between each line of acquisition, the phase encode gradient is incremented in discrete linear steps of $G_{phase\ inc}$. To avoid aliasing, $G_{phase\ inc}$ is chosen according to:

$$G_{phase\ inc} = \frac{2\pi}{\gamma t_{phase} FOV_{phase}} \qquad 46$$

where FOV_{phase} is the field-of-view in the phase direction. It should be noted that $G_{phase\ inc}$ is the maximum increment in the phase encode gradient between adjacent phase encode steps and not the maximum applied gradient. The spatial resolution in the phase direction is given by:

$$\Delta y = \frac{FOV_{phase}}{N_{pe}} \qquad 47$$

where N_{pe} is the number of phase encode steps in the y direction.

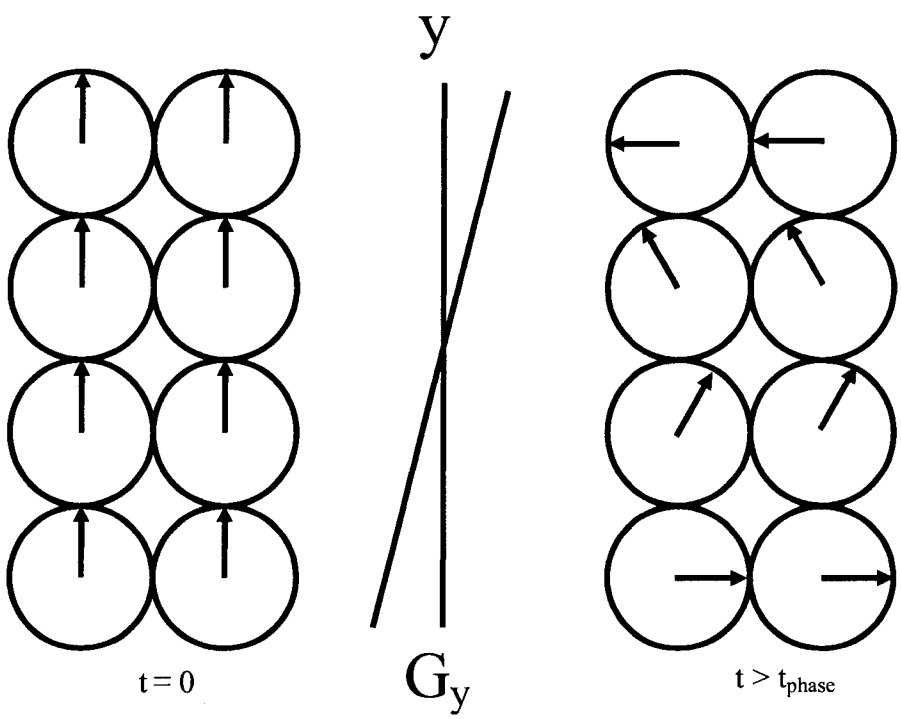

Figure. C-12 The phase distribution before and after application of the phase encode gradient. The gradient G_y is applied for time t_{phase} resulting in a phase distribution that is dependant on the displacement from the gradient center.

C 5 The Signal Equation and k Space.

In the previous sections of this chapter, we have discussed the creation and spatial encoding of signal. In this section, we shall investigate the resultant signal and its use in creation of an image. To keep things simple we shall look at a two dimensional sequence demodulated by ω_O using a phase sensitive detector, we shall also ignore the effects of T2 relaxation.

The receiver detects signal from all the precessing magnetic moments within the excited volume according the slice selection process. The sum of all the received signal due to $M_{xy}(x,y)$ within the region of interest can written as the integral:

$$S(t) = \int_x \int_y M_{xy}(x,y) e^{-i2\pi\left|k_{read}(\tau)x + k_{phase}(\tau)y\right|} dxdy \qquad 48$$

where k_{read} and k_{phase} are the time integrals of the gradient waveforms in the read and phase directions and are given by:

$$k_{read} = \gamma \int_0^t G_{read}(\tau) d\tau \qquad 49$$

$$k_{phase} = \gamma \int_0^t G_{phase}(\tau) d\tau \qquad 50$$

Note that equation 48 has the form of a Fourier transform.[9]

The terms k_{read} and k_{phase} are positions in k-space. K-space is a space in which frequency and phase exist in place of displacements in real space. The k space data generally has as many points as there are voxels in an image. As seen in equations 49 and 50, k-space is traversed by application of magnetic field gradients. Figure. C-13 demonstrates how a single 2-D gradient echo pulse sequence samples k-space. During time 1 both the phase encode and read encode de-phaser gradients are on which results in a shift in k-space. During time 2 of the sequence the read encode gradient is turned on while signal is simultaneously acquired. The result of this is that a whole line of k_{read} k-space data is sampled.[5] In the following TR, the height of the phase encode

gradient is incremented such that a new k_{read} line is sampled. This scheme is repeated until all of k-space has been sampled. The field of view is related to the sampling rate through:

$$FOV_{read} = \frac{1}{\Delta k_{read}} = \frac{2\pi N_{read}}{\gamma G_{read} \text{Time } 2} \qquad 51$$

$$FOV_{phase} = \frac{1}{\Delta k_{phase}} = \frac{2\pi}{\gamma G_{phase\ inc} \text{Time } 1} \qquad 52$$

and resolution through

$$\text{Pixel Size}_{read} = \frac{1}{\Delta k_{read} N_{read}}$$

$$\text{Pixel Size}_{phase} = \frac{1}{\Delta k_{phase} N_{pe}}$$

Hence, the pixel size is inversely proportional to the number of frequency encodes (N_{read}) or N_{pe}.

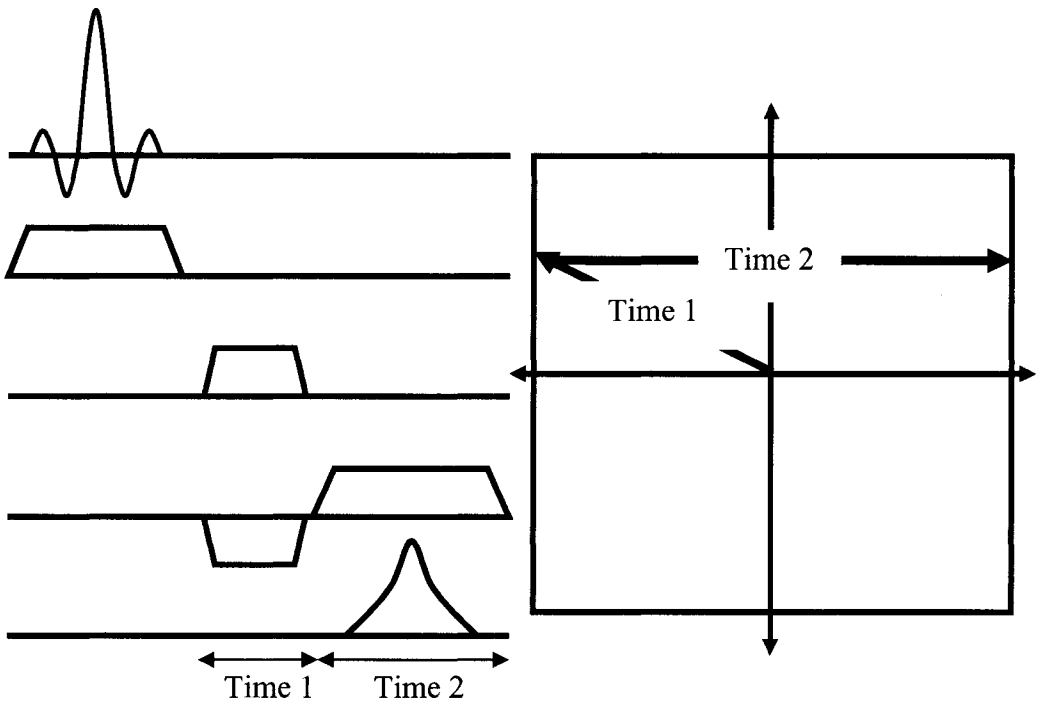

a) b)

Figure. C-13 A typical gradient echo pulse sequence is shown in a) and the effect of the respective gradients have on the traversal of k-space.

C6 Imaging Pulse Sequences:

In this section pulse sequence diagrams are shown for standard imaging sequences employed in the thesis. The pulse sequences provide the order and timings of the applied magnetic fields required to create the images. Figure C-14 shows the pulse sequence for a GE imaging sequence. Figure C-15 demonstrates the pulse sequence for an FSE sequence. Finally figure C-16 shows a BFFE sequence. The contrast for each of these pulse sequences is determined by the combination of TE, TR and α_{TIP}.

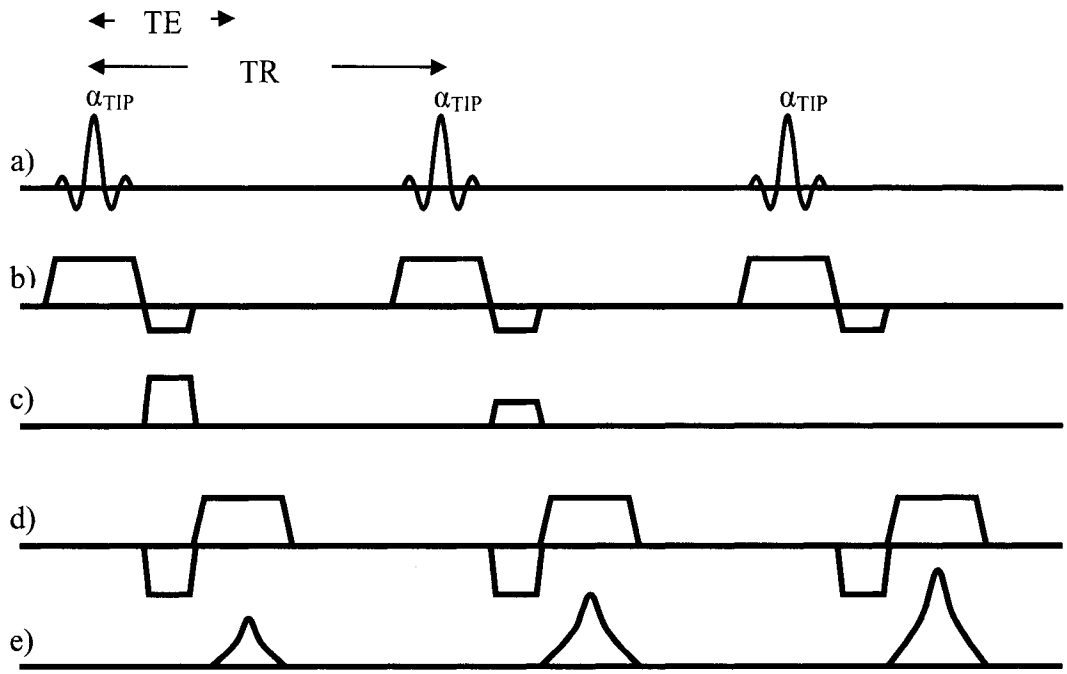

Figure. C-14 A GE pulse sequence diagram. Shown are the channels for RF a), slice select b), phase encode c), frequency encode d) and the receiver e).

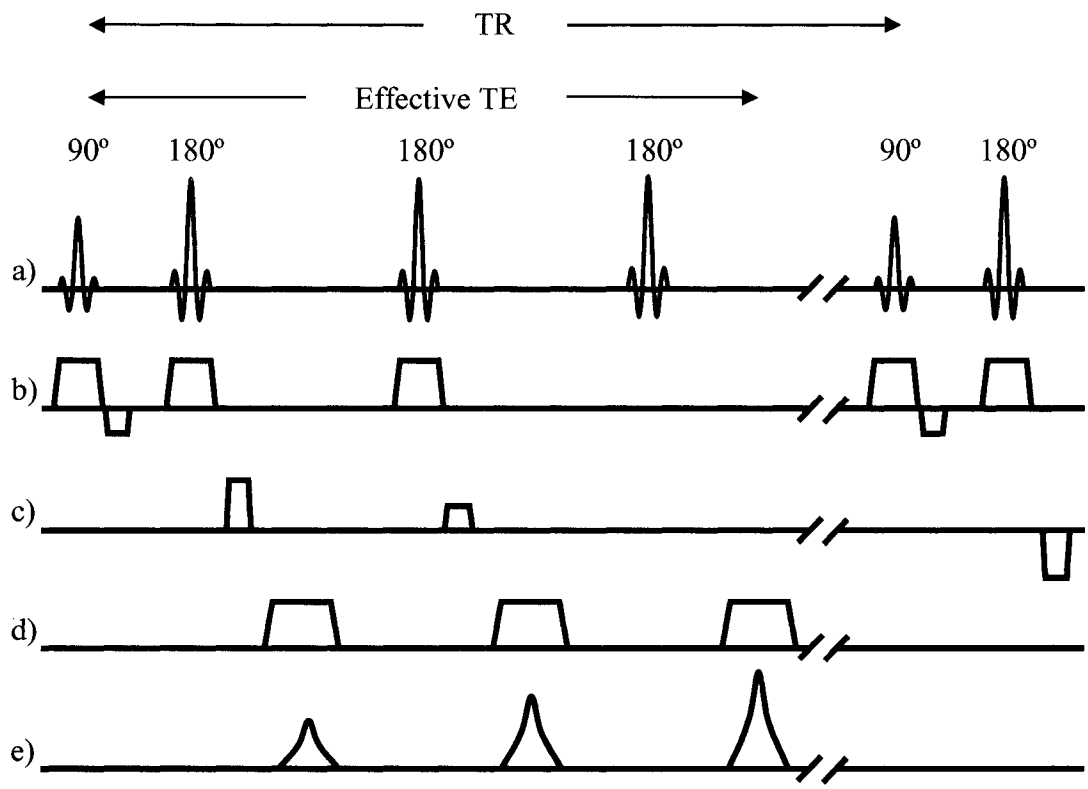

Figure. C-15 A FSE pulse sequence diagram. Shown are the channels for RF a), slice select b), phase encode c), frequency encode d) and the receiver e).

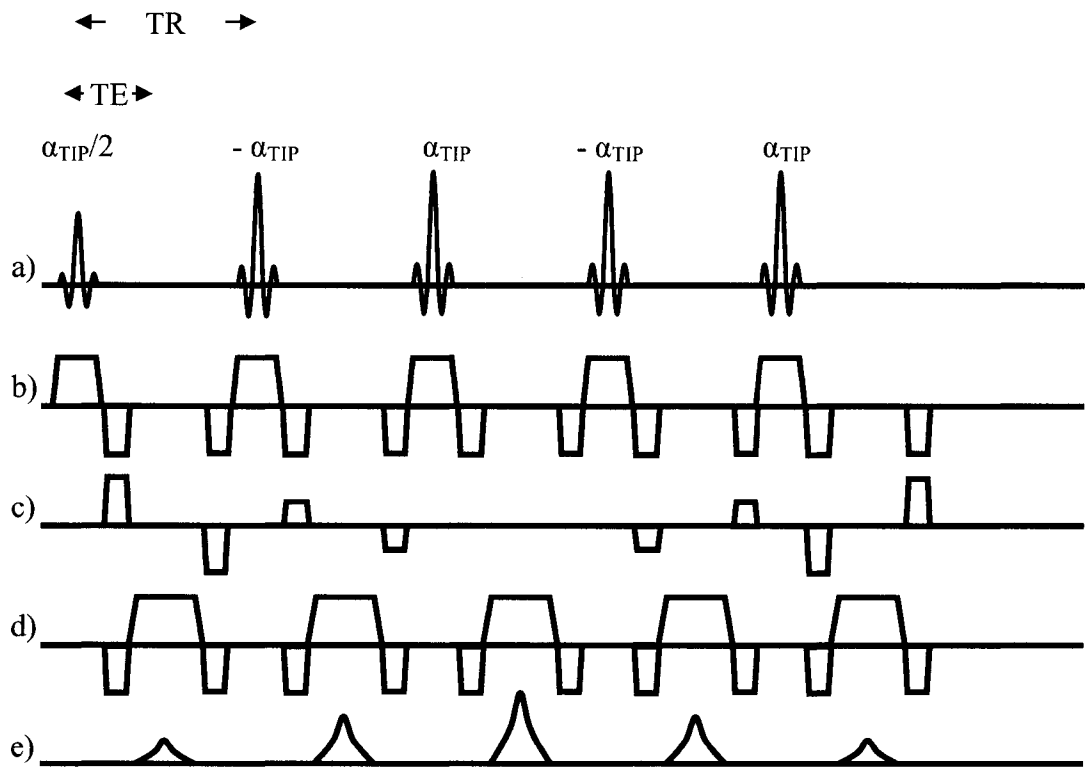

Figure. C-16 A BFFE pulse sequence diagram. Shown are the channels for RF a), slice select b), phase encode c), frequency encode d) and the receiver e).

C 7 Conclusion:

Appendix C provides a basic overview of the MRI experiment which is the subject of chapters 4 and 5 in this thesis.

References

[1] M.J. Bronskill and P. Sprawls , "The physics of magnetic resonance imaging" American Institute of physics (1993)

[2] E.M Haake. R.W.Brown, M.R.Thompson, R. Ventakesan, "Magnetic Resonance Imaging, physical principles and sequence design", John Willey & Sons (1999)

[3] F. Bloch "Nuclear induction", Physical Review 70, 460-474 (1946)

[4] E.M. Purcell, H.C. Torrey and R.B. Pound. "Resonance absorption by nuclear magnetic moments in a solid" Physical Review 69, 37-38 1946

[5] D.G. Nishimura. " Principles of magnetic resonance imaging" Stanford University (1996)

[6] M.A. Brown and R.C. Semelka "MRI Basic Principle and Applications" John Wiley & Sons, (1995)

[7] D.W. McRobbie., "Investigation of slice characteristics in NMR imaging" Phys. Med. Biol., 31, 613-626 (1986)

[8] R. Freeman., "Shaped radiofrequency pulses in high resolution NMR" J. of Progress in NMR Spectroscopy 32, 59-106 (1998)

[9] R.N. Bracewell., "The Fourier transform and its Applications" McGraw Hill. (1978)